Quantum Optics on Artificial Quantum Media

Teresa Hönigl-Decrinis

Department of Physics

Royal Holloway, University of London

Supervisor: Prof. Oleg Astafiev

This dissertation is submitted for the degree of

Doctor of Philosophy.

1st March 2018

Declaration of Authorship

I, Teresa Hönigl-Decrinis, confirm that the work presented in this thesis is my own. Where information has been derived from other sources, I confirm that this has been indicated in the work.

Abstract

Superconducting artificial atoms are remarkably attractive to study quantum optics phenomena. The artificial atoms are nano-scale electronic circuits that can be fabricated using well-established techniques and can therefore be easily scaled up to larger systems. Their energy levels can be engineered as desired, and strong coupling can be achieved with resonators and transmission lines. This greater control of parameters is a huge advantage over natural atoms and allows to reach regimes that would otherwise be unattainable.

In this thesis, we report on quantum optics phenomena on chip and their emerging devices for present and future applications with a focus on quantum wave mixing (QWM) effects.

First, we study continuous wave mixing on a quantum object and observe a symmetric spectrum with an infinite number of side peaks. Then, we investigate two regimes of QWM: Coherent wave mixing and quantum wave mixing with non-classical superposed states. In the former, two pulsed waves with frequencies slightly detuned from each other are scattered on the single artificial atom resulting in a symmetric spectrum with an infinite number of side peaks. The amplitude of each of these peaks oscillates in time according to Bessel functions with the orders determined by the number of interacting photons. In the latter regime, a time delay between the two pulses is introduced causing a striking difference in the spectrum, which now exhibits a finite number of narrow coherent emission peaks. Furthermore, the spectrum in the latter regime is asymmetric with the number of positive frequency peaks (due to stimulated emission) always exceeding by one compared to the negative

frequency peaks (due to absorption).

Then, we investigate a coherent frequency conversion scheme with a single three-level artificial atom. The scheme is based on three-wave mixing, which utilises the quantised energy levels of the artificial atom. We drive the three-level atom with two continuous drives corresponding to two transition frequencies of the atom and measure the coherent emission at the sum or difference frequency. The device may be used as a quantum router, coherently interconnecting quantum channels, in prospective quantum networks.

Another part of the thesis addresses the challenge of measuring the absolute power of a microwave signal in a transmission line at cryogenic temperatures which is critical for applications in quantum optics, quantum computing and quantum information. We demonstrate that a two-level system strongly coupled to the open space can act as a quantum sensor of absolute power. We realise the quantum sensor using a superconducting flux qubit that is strongly coupled to the environment. The quantum sensor is independent of dephasing of the two-level system.

Acknowledgements

First of all I'd like to thank my thesis supervisor, Prof. Oleg Astafiev, and the whole Nano-technology group for giving me the opportunity to work on quantum optics with superconducting circuits and for providing such a supportive, fun and stimulating environment.

Thanks to Dr. Rais Shaikhaidarov for training me rigorously in nanofabrication. Fabricating the first working superconducting qubit in the UK was definitely a highlight during my doctoral studies. After spending hours, days or even weeks in the clean room, it is extremely rewarding when you finally measure your device and it actually works.

Thanks to Dr. Vladimir Antonov for all your constructive feedback on manuscripts and for generally always being approachable.

Thanks to Massimo Venti for machining all my bits and pieces so promptly and for advising me on my car troubles.

Thanks to my collaborators at the National Physical Laboratory, Dr. Tobias Lindström and Dr. Sebastian de Graaf for fruitful discussions, technical and scientific support.

Thanks to my thesis advisor, Prof Phil Meeson, and moderator, Prof Glen Cowan, for grilling me for hours during my upgrade meeting and preparing me well for the upcoming viva-voce examination.

Thanks to Aleksei Dimitriev, Dr. Ivan Khrapach , Iulia Zotova, Sasha Kulakova and the rest of the Artificial Quantum Systems group at the Moscow Institute of Physics and Technology for always welcoming me in Moscow with open arms, and for the fun times and discussions.

Thanks to Sebastian Skacel, and Ilya Antonov. It's been a pleasure to work alongside you.

Thanks to Royal Holloway, and the National Physical Laboratory for supporting my PhD project with a stipend.

Thanks to Mr Kapper who inspired me to study Physics at university level.

Thanks to my family and friends who, I know, I can always count on. I love you.

And last but not least, many thanks to everyone who has supported and encouraged me. I dedicate this thesis to you!

Contents

1 Introduction **24**

1.1 Overview of the thesis 24

2 Basic concepts **26**

2.1 Superconductivity and the Josephson Effect 26

2.2 Qubits and quantum computing 31

2.3 Superconducting qubits 33

2.3.1 Charge based qubits 33

2.3.2 The RF-squid 35

2.3.3 The flux qubit 37

2.4 Artificial atoms 42

2.5 Quantum dynamics of open systems 43

2.5.1 The transmission line 43

2.5.2 The density matrix formalism 44

2.5.3 The master equation 45

2.5.4 The Bloch equations 48

2.5.5 Quantum regression theorem 50

2.5.6 Emission spectra 51

2.5.7 Relaxation 56

2.5.8 Dephasing 58

3 Experimental principles **61**

3.1 Sample design considerations 61

3.2 Fabrication 63
3.2.1 Photolithography 64
3.2.2 Electron beam lithography 66
3.3 Room temperature characterisation 71
3.4 Wire bonding 72
3.5 Measurement setup 72
3.5.1 Cryogenic Environment 74
3.5.2 Microwave engineering 76
3.6 Qubit characterisation 77
3.6.1 Spectroscopy 77
3.6.2 Smith chart representation of the microwave transmission 81
3.6.3 Rabi Oscillations 82

4 Quantum wave mixing and visualisation of photonic states 86
4.1 Introduction 87
4.2 Sample description 89
4.3 Stationary coherent wave mixing 91
4.4 Pulsed coherent wave mixing 95
4.4.1 Coherent and zero-one photon superposed state 97
4.4.2 Elastic scattering and Bessel function Rabi oscillations . 99
4.5 Quantum wave mixing 102
4.6 Probing the two-photon superposed state 105
4.7 Theoretical description 106
4.7.1 Continuous wave mixing on a single two-level atom . . . 107
4.7.2 Elastic scattering of electromagnetic waves on an artificial atom 110
4.7.3 Elastic scattering of two frequencies 112
4.7.4 Quantum mixing 117
4.7.5 Two-photon quantum mixing 119
4.8 Conclusion 121

5 Mixing of coherent waves on a single three-level artificial atom 124

5.1 Introduction 124

5.2 Sample description 126

5.3 Coherent frequency conversion 127

5.4 Conclusion 134

6 Quantum sensor of absolute power 136

6.1 Introduction 136

6.2 Sample description and working principle 137

6.3 Reflection through the transmission line 140

6.4 Quantum oscillations 142

6.5 Mollow triplet 143

6.6 Wave mixing in combination with the Mollow triplet 144

6.7 Conclusion 147

7 Conclusion and outlook 149

Bibliography 151

List of publications

This thesis is partly based on the following journal articles:

1. A Yu Dmitriev, R Shaikhaidarov, V N Antonov, T Hönigl-Decrinis, and O V Astafiev. Quantum wave mixing and visualisation of coherent and superposed photonic states in a waveguide. *Nature Communications*, 8(1):1352, 2017

2. T Hönigl-Decrinis, R Shaikhaidarov, I V Antonov, V N Antonov, A Yu Dmitriev, and O V Astafiev. Mixing of coherent waves on a single artificial atom. Submitted (2018).

3. T Hönigl-Decrinis, A Yu Dmitriev, R Shaikhaidarov, V N Antonov , and O V Astafiev. Two-level system as a quantum sensor of absolute power. In preparation.

4. A Yu Dmitriev, R Shaikhaidarov, T Hönigl-Decrinis, V N Antonov , and O V Astafiev. Stationary coherent wave mixing of propagating waves on a single two-level system. In preparation.

In addition, I have contributed to the publication below:

5. S. E. de Graaf, S. T. Skacel,T. Hönigl-Decrinis, R. Shaikhaidarov, H. Rotzinger, S. Linzen, M. Ziegler, U. Hübner, H.-G. Meyer, V. Antonov, E. Il'ichev, A. V. Ustinov, A. Ya. Tzalenchuk, O. V. Astafiev. Quantum Interference Device. *Nature Physics* (2018).

List of Figures

2.1 Superconductivity and the Josephson effect. (a) The resistance of some metals drops abruptly to zero at the critical temperature. (b) Leakage and interference of macroscopic wavefunctions of two superconductors in an SIS junction (c) Formation of Cooper pairs in BCS theory. (d) The electron spectrum: (on the left) in normal metals at $T = 0$ and (on the right) in superconductors at $T << T_c$ with the superconducting gap 2Δ. . . . 28

2.2 (a) Current biased Josephson junction denoted as an X and (b) its washboard potential $U_J(\delta) = E_J[1 - cos(\delta)]$. 30

2.3 Bloch sphere. Any arbitrary qubit state can be represented as a point on the unit sphere. 32

2.4 (a) Schematic circuit and (b) electrostatic energies of the Cooper pair box (CPB). 34

2.5 Energy spectrum of the Cooper pair box for the ratio (a) $E_J/E_C = 0.1$, (b) $E_J/E_C = 4$, and (c) $E_J/E_C = 50$. 35

2.6 (a) Circuit diagram of the RF-Squid. (b) Energy spectrum of the first four levels of the RF-squid with $E_L/h = 70$ GHz, $E_J/h = 30$ GHz, and $E_C/h = 100$ GHz. (c-d) Potential of the RF-squid for $\delta_{ext} = \pi$ and $\delta_{ext}/2\pi = 0.3$ respectively with the first few energy levels. 36

2.7 Schematic circuit representation of a four junction flux qubit capacitatively coupled through a capacitance C_k to a transmission line. 38

2.8 Potential of four-JJ flux qubit U/E_J (a-b) for $\alpha = 0.7$, $\delta_{23} = \delta_{12}$ at $\delta_{ext} = \pi$, (c) for α ranging from 0.3 to 0.9 at $\delta_{ext} = \pi$ where $\delta = \delta_{01} = \delta_{12} = \delta_{23}$, (d) for $\delta = \delta_{01} = \delta_{12} = \delta_{23}$, $\alpha = 0.7$ at $\delta_{ext}/2\pi$ ranging from 0.3 to 0.7. 40

2.9 (a) First three energy bands and (b) first transition energy of a 4-JJ flux qubit with $E_J/h = 50GHz$, $C_J = 5fF$, $\alpha = 0.5$ as a function of external flux numerically simulated in Matlab. . . . 42

2.10 Schematic circuit representation of a transmission line modelled as a chain of inductances L and capacitances C. 43

2.11 Evolution of a two-level atom ($\Gamma_2 = \Gamma_1/2 = 0.5$ arb. u.), initially in its ground state $\vec{\sigma_0} = \{0, 0, 1\}$, under a resonant drive with amplitude $\Omega = 8$ arb. u. and phase $\phi = 0$. a) Rabi oscillations. $\vec{\sigma_x}$,$\vec{\sigma_y}$,$\vec{\sigma_z}$ as a function of time. b) Evolution visualised on the Bloch sphere. c) Evolution as a function of σ_z and σ_y. . . 50

2.12 Schematic of an artificial atom coupled through a capacitance C_k to a 1-D transmission line. The incident wave indicated by the green arrow is scattered in both directions (red arrows). . . 52

3.1 Normal resistance R_N (normalised to a junction area of 200 × 800 nm^2) of several $Al/Al_2O_3/Al$ Josephson junctions plotted against oxygen pressure. All test tunnel junction were oxidised for 10 minutes under different oxidation pressures at room temperature. The variation of the thickness distribution of $Al/AlOx/Al$ tunnel junctions with oxygen pressure and oxidation time has been studied in [2, 3]. 63

3.2 (a) Design of one building block of the photomask. On the top, there are eight fields for test structures. The field for the nano circuitry is located in the centre (main field). (b) A sapphire wafer cut into half after photolithography. 65

3.3 Fabrication steps for electron-beam lithography. a) Copolymer of thickness 0.7μ m is spun on the undoped silicone or sapphire substrate. b) After baking, a 60 nm layer of ZEP520A is spun on top of the first layer and baked. c) Electron beam lithography of qubits. d) Development of the exposed resist. e) Evaporation of aluminium. f) Oxidation of aluminium. g) Shadow evaporation technique [4]. h) Resist liftoff. Figure adapted from [5]. 66

3.4 Chip design with a base dose of 70 μCcm^{-2} (dark blue). Seven qubits are capacitatively coupled to a transmission line. The transmission line and contact pads have been proximity corrected. A dose of 181 is assigned to the qubit lines containing Josephson junctions (in red). A dose of 166 is assigned to the qubit lines (in orange). A dose of 121 is assigned to the coupling capacitors (in green). 69

3.5 Photograph of sample holder assembly. (a) Printed Circuit Board (PCB). (b) Aluminium wire bonds connecting the sample chip with the PCB. The transmission line on chip is connected to the impedance matched line (50Ω) on the PCB with 3 bonds on each side. The ground plane of the PCB is bonded to the ground plane of the sample chip, with ~ 6 bonds along the sample chips width and ~ 15 bonds along its length. (c) PCB with bonded sample chip on copper stand. A copper anti-spacer is screwed on top of the PCB to minimise room for standing waves avoiding parasitic resonances. 73

3.6 Photograph of *Blue Fors* cryostat insert layout. (a) From top to bottom: 50K flange, quasi-4K flange, still flange, cold plate, and mixing chamber flange. (b) Coil assembly for flux qubits. (c) Additional stage for flux qubit sample holders. The coil assemblies are shielded by a *Cryoperm* shield. 74

3.7 Drawing of sample holder assembly. 75

3.8 (a) Circuit schematic and (b) photograph of a chopper consisting of two mixers, one splitter, a low pass filter and attenuators. 77

3.9 The first UK qubits. (a) False-coloured scanning-electron micrograph (SEM) of a flux qubit coupled to a 1D transmission line. The flux qubit consists of a macroscopic superconducting loop interrupted by four Josephson junctions that are inductively coupled to the line. (b) Six flux qubits with varying loop area inductively coupled to the transmission line. Colour-code: Yellow, blue and violet correspond to gold, aluminium and the Si substrate respectively 78

3.10 Experimental setup for tranmission spectroscopy. The input line is attenuated using 60dB at room temperature, 10dB at 4K and 30dB at 15mK. The flux qubit is coupled through mutual inductance to the transmission line (on chip). The output line includes an isolator giving $\sim$ 20dB attenuation to prevent noise reaching the sample from the output line. The signal is then amplified at 4K and at room temperature. The external flux applied to the artificial atom acts as control. 79

3.11 Transmission spectroscopy of the flux qubit (Qubit ID 4). Shown is the real and imaginary part of the reflection coefficient r as a function of flux bias $\delta\phi/\phi_0$ and incident microwave frequency $\omega/2\pi$ where $\delta\phi = \phi_{ext} - \phi_0/2$. 81

3.12 Elastic scattering of microwaves on the artificial atom (Qubit ID 5) measured at driving powers -24dBm to -4dBm with a step of 4dBm. (a) Smith chart representation of the microwave transmission for (b) Power extinction $|t|^2$, (c) real part of the reflection coefficient r, and (d) imaginary part of the transmission coefficient t as a function of frequency detuning $\delta\omega/2\pi$ from the atomic transition $\omega_0/2\pi = 14.678$ GHz. 83

3.13 Rabi oscillations (a) pulse sequence: The driving pulse P prepares the atomic states, and the emission from the atom is detected during the readout pulse R. (b) The measurement yields decaying Rabi oscillations in time (at fixed driving power of -6dBm. 84

3.14 Intensity plot of decaying Rabi oscillations as a function of incident pulse length Δt_P and driving power. 84

3.15 Experimental setup for measuring Rabi oscillations. A microwave pulse is formed using a chopper consisting of two IQ modulation mixers, a splitter, a low pass filter, and some attenuators (see Fig 3.8). The Vector Network Analyser (VNA) provides the continuous coherent microwave, while the pulse function arbitrary generator (PFAG) generates the pulse envelope, both of which are fed into the chopper. The microwave pulse is then attenuated by 40dB at room temperature, 10dB at 4K, and 30dB at 15mK before interacting with the flux qubit that is biased through a superconducting coil. The output line features an isolator and two amplifiers, one at 4K and the other at room temperature. A read out pulse is formed through an additional chopper on the output line. The output signal is detected by a VNA. 85

4.1 The device. (A) SEM image of a flux qubit coupled to the transmission line through an interdigitated capacitance. (B) A schematic circuit representation of the device consisting of a superconducting qubit interrupted by four Josephson junctions. 89

4.2 Spectroscopy. (A) A transmission spectroscopy of the system as a function of the normalised magnetic flux bias measured by a vector network analyser (VNA). The red dashed curve shows calculations of the energy $\approx \omega_{01}$. An inset shows the transmission phase under a strong drive. A transition line at ω_{01} crosses a line from the two-photon transition process at ω_{02}. The crossing takes place at a point where $\omega_{01} = \omega_{12}$. (B) A simulation of the system energies with parameters close to our artificial atom. The red arrowed lines show two equal transition frequencies $\omega_{01} = \omega_{12} \neq \omega_{23}$. The insets show level schemes at $\delta\Phi/\Phi_0 = \pm 0.035$ and at $\delta\Phi/\Phi_0 = 0$. 90

4.3 Experimental setup for wave mixing in the continuous regime. Two continuous microwaves slightly detuned from each other and from the resonance of the atom are generated, added and delivered to the artificial atom (Fig. 4.1). The output is amplified twice and then measured by a Spectrum Analyser (SPA). . 92

4.4 (a) Schematic of the concept and resulting spectrum of wave mixing on a single two-level system. (b) and (c) show spectra of coherently scattered radiation measured when the driving tones are either (b) off-resonant or (c) resonant with the qubit, plotted as a function of the amplitude of both drives $\Omega = \Omega_+ = \Omega_-$. (d) An averaged trace at fixed driving amplitude Ω measured by a spectrum analyser. 93

4.5 Side spectral components of elastically scattered radiation due to wave mixing effects for (a) equal driving amplitudes $\Omega = \Omega_+ = \Omega_-$ and (b) unequal driving amplitudes $\Omega_- > \Omega_+$ by 1dB. The "plus"-components are larger in power compared to the "minus"-components demonstrating high sensitivity of wave mixing peaks to driving amplitudes. 95

4.6 Measurement set up for QWM mixing with individual pulse manipulation. A vector network analyser (VNA) and a microwave generator (Gen) are used as microwave sources. The pulse envelope is provided by a pulse function arbitrary generator (PFAG). Pulses are shaped with choppers (CH), added and delivered to the sample. The output is amplified twice and measured using a spectrum analyser (SPA). Additional cables may be added to the circuit to introduce delays between pulses. 96

4.7 Principles of the device operation. (a) False coloured SEM image of the device: an electronic circuit (a superconducting four Josephson junction loop), behaving as an artificial atom, embedded into a transmission line, strongly interacts with propagating electromagnetic waves. (b) The four-wave mixing process results in the zero-one photon field creation at $\omega_3 = 2\omega_+ - \omega_-$. In classical mixing, process $a_+ a^\dagger a_+ b_3^+$ comes in a pair with the symmetric one $a a_+^\dagger a b_{-3}^+$. In the mixing with non-classical states, the time-symmetry and, therefore, spectral symmetry are broken. (c) In QWM, the number of spectral peaks is determined by the number of photonic (Fock) states forming the superposed state in the atom. The state is created by the first pulse at ω_- and then mixed with the second pulse of ω_+. Single-photon ($N_{ph} = 1$) state $|\beta\rangle_- = B(|0\rangle + \beta\,|1\rangle)$ can only create a peak at $\omega_3 = 2\omega_+\omega_-$ because only one photon at can be emitted from the atom. Two photon ($Nph = 2$) superposed state $|\gamma\rangle_- = C(|0\rangle + \gamma_1\,|1\rangle + \gamma_2\,|2\rangle)$ results in the creation of an additional peak at $3\omega_+ 2\omega$, because up to two photons can be emitted. Also two photons of ω_- can be absorbed, creating an additional left-hand-side peak at $2\omega_-\omega_+$. 98

4.8 Dynamics of coherent wave mixing.(a) An example of a spectrum of scattered microwaves, when two simultaneous periodic pulses of equal amplitudes and frequencies ω_- and ω_+ are applied according to the top time diagram. The mixing of coherent fields $|\alpha\rangle_\pm$, consisting of an infinite number of photonic states results in the symmetric spectrum with an infinite number of side peaks, which is the map of classical states. (b) Four panels demonstrate anharmonic Rabi oscillations of the peaks at frequencies $\omega_0 + (2k+1)\delta\omega$. The measured data (dots) are fitted by squares of $2k+1$-order Bessel functions of the first kind (solid lines). The orders are equal to the interacting photon numbers. 101

4.9 Quantum wave mixing with non-classical states. (a) Two consecutive pulses at $\omega_- = \omega_0 - \delta\omega$ and then at $\omega_+\omega_0 - \delta\omega$ are applied to the artificial two-level atom with $\delta\omega = 1$kHz, $\omega_0 \approx 9$GHz. The plot exemplifies the QWM power spectrum from the zero-one photon coherent state $|\beta\rangle_-$. The single side peak at $2\omega_+ - \omega_-$ appears, due to the transformation of $|\beta\rangle_-$ (one photon, $N_{ph} = 1$, from $|\beta\rangle_-$ and two photons from $|\alpha\rangle_\pm$). (b) The peak amplitude dependences at several side-peak positions in classical (left column) and quantum with the two-level atom (right column) wave mixing regimes as functions of both driving amplitudes ($\alpha_\pm$) expressed in photons per cycle. Several side peaks are clearly visible in the classical regime. This is in striking difference from the quantum regime, when only one peak at $2\omega_+ - \omega_-$ is observed and behaves qualitatively similar to the one in the classical regime. 103

4.10 Quantum wave mixing with two-photon superposed states and sensing of quantum states. The mixing spectrum with the three-level atom consists of five peaks, which is a result of the mapping of two-photon state $|\gamma\rangle_-$ ($N_{ph} = 2$). Comparing with Fig. 4.9, an additional emission peak at $3\omega_+ - 2\omega_-$ appears, corresponding to two-photon emission from $|\gamma\rangle_-$. The absorption process resulting in a peak at $2\omega_- - \omega_+$ is now possible, as it is schematically exemplified. Importantly, the device probes the photonic states of the coherent field, distinguishing classical (Fig. 4.8(a)) ($N_{ph} = \infty$), one- ($N_{ph} = 1$), and two-photon ($N_{ph} = 2$) superposed states. 106

4.11 a) Pulse sequence b) The first pulse prepares the coherent single-photon state $|\beta\rangle_-$ which interacts with the coherent state $|\alpha\rangle_+$ of the second pulse. c) Schematic presentation of the only non-trivial high order process resulting in a peak at $\omega_0 + 3\delta\omega$. 118

4.12 a) The system can be tuned to a working point where the transition from the ground state to the first excited state and from the first excited state to the ground state are equal and other energies are far away. b) We consider two sequential pulses at frequencies ω_- and ω_+ interacting with the equally spaced three-level atom resulting in the spectrum exhibiting five peaks. c) The first pulse prepares the coherent two-photon state $|\gamma\rangle_-$ which interacts with the coherent state $|\alpha\rangle_+$ of the second pulse. d) Schematic of the physical process resulting in a peak at $3\omega_+ - 2\omega_-$. 120

4.13 Different regimes of mixing and dynamics of photonic states. (a) Coherent wave mixing on a single artificial atom in the continuous driving regime. (b) Anharmonic Rabi oscillations in classical wave mixing on a single artificial atom. (c) Quantum wave mixing with a two-level atom. The single emission side peak appears. (d) Quantum wave mixing on a three-level atom. Two more side peaks at $3\omega_+ - 2\omega_-$ and $2\omega_- - \omega_+$ appear because the two-photon field is stored in the atom at ω_-. 122

5.1 (a) False-coloured micrograph of the device taken at an angle. The three-level artificial atom consisting of a superconducting loop with four Josephson junctions is capacitatively coupled to the transmission line. (b) Spectroscopy of the single artificial three-level atom. The transition frequencies are detected by transmission as a function of flux bias and probe driving frequency. Choosing a working point away from the degeneracy point $\delta\Phi \neq 0$ indicated by the dashed line in (b) results in (c) a cyclic-type artificial atom with transition frequencies $\omega_{21}/2\pi = 6.48$ GHz, $\omega_{32}/2\pi = 8.35$ GHz, and $\omega_{31}/2\pi = 14.83$ GHz. 126

5.2 Measurement setup for coherent mixing of a three-level artificial atom under two continuous driving tones. 128

5.3 Coherent emission in a driven three-level atom with energy diagrams of the pumping schemes. (a) The three-level atom is continuously driven with driving amplitudes Ω_{23} and Ω_{13}, in b) with driving amplitudes Ω_{12} and Ω_{13}, and in c) with driving amplitudes Ω_{12} and Ω_{23}. d) The measured coherent emission peak at ω_{12} in terms of photon rate, ν_{em}^{21}, under driving amplitudes $\Omega_{23}/2\pi = 16$ MHz, $\Omega_{13}/2\pi = 50$ MHz, as a function of detuning of the driving frequency, $\delta\omega_{23}^{d}$. The inset schematically shows the typically measured spectrum. 129

5.4 Measurement of coherent emission photon rate ν^{em} in arbitrary units as a function of frequency detuning $\delta\omega^d$ of the two drives with amplitudes Ω_{ij} indicated on the panels. (a) Emitted photon rate of the transition from $|2\rangle \rightarrow |1\rangle$, ν_{21}^{em}, with Rabi frequencies corresponding to the respective field strengths Ω_{13}, Ω_{23}. (b) Emitted photon rate of the transition from $|3\rangle \rightarrow |2\rangle$, ν_{em}^{32}, with Rabi frequencies corresponding to the respective field strengths Ω_{13}, Ω_{12}. (c): Emitted photon rate of the transition from $|3\rangle \rightarrow |1\rangle$, ν_{em}^{31}, with Rabi frequencies corresponding to the respective field strengths Ω_{12}, Ω_{23}. 131

5.5 Numerical simulations of coherent emission photon rate ν_{em} as a function of frequency detuning $\delta\omega^d$ of the two drives with amplitudes Ω_{ij} indicated on the panels. (a) Emitted photon rate of the transition from $|2\rangle \rightarrow |1\rangle$, ν_{21}^{em}, with Rabi frequencies corresponding to the respective field strengths Ω_{13}, Ω_{23}. (b) Emitted photon rate of the transition from $|3\rangle \rightarrow |2\rangle$, ν_{32}^{em}, with Rabi frequencies corresponding to the respective field strengths Ω_{13}, Ω_{12}. (c) Emitted photon rate of the transition from $|3\rangle \rightarrow |1\rangle$, ν_{31}^{em}, with Rabi frequencies corresponding to the respective field strengths Ω_{12}, Ω_{23}. 132

6.1 Transmission spectroscopy, $Im[t]$, of four flux qubits. We benchmark the absolute power sensor at 7.48 GHz. 138

6.2 Transition frequencies (top row), and relaxation rates (bottom row) f_{12}, $\Gamma_{1(12)}$ in red, f_{13}, $\Gamma_{1(13)}$ in yellow and f_{23}, $\Gamma_{1(23)}$ in violet as a function of flux $\delta\phi/\delta\phi_0$ of artificial atoms A,B,C and D. Blue markers are experimental points taken from transmission spectroscopy (Fig. 6.1). Solid lines are numerical simulations calculated with fitting parameters $E_C = 16$ GHz, $E_J = 53$ GHz with α and coupling capacitance C shown in the insets. 139

6.3 Schematic of a cryogenic environment together with an illustration of the chip containing a two-level system - the absolute power sensor - coupled to a transmission line. Knowledge of absolute powers W_0 supplied to a chip at cryogenic temperatures, are important for most quantum technologies with superconducting circuits. The two-level system with dipole moment μ interacts with the field V_0 containing many photons giving rise to coherent oscillations at Rabi frequency Ω. 139

6.4 Qubit B. a) Reflection as function of frequency for a set of input powers W_{in}. b) Reflection at $f = 7.468$ GHz versus input powers W_{in}. 141

6.5 The absolute power W_0 sensed by qubits A, B, C, and D (Table 6.1) at 7.48 GHz as a function of (a) input power W_{in} and as a function of (b) output power W_{out}. The slope of the linear fit (solid red line) represents (a) attenuation and (b) gain in our measurement circuit. 142

6.6 (a) Rabi oscillations (of qubit B) for input powers W_{in} ranging from -10 to 8 dBm. (b) The absolute power W_0 sensed by qubits A, B, C, and D (Table 6.1) at 7.48 GHz as a function of input power W_{in}. The slope of the linear fit (solid red line) represents attenuation in our measurement circuit. 143

6.7 Qubit B. a) Mollow triplet as a function of W_{in} and frequency. b) Linear frequency spectral density of emission power under a resonant drive with fixed driving power $W_{in} = 0.73$mW forming the Mollow Triplet. Experimental data is presented by blue markers. The red solid curve presents the fit of the emission spectrum according to Eq.6.6with $\Gamma_1 = 12.36$ MHz and $\Gamma_2 = \Gamma_1/2$. From the fitting parameters we obtain the Rabi frequency as a function of the input driving power. 144

6.8 The absolute power W_0 sensed by qubits A, B, C, and D (Table 6.1) at 7.48 GHz as a function of input power W_{in}. The slope of the linear fit (solid red line) represents attenuation in our measurement circuit. 145

6.9 Qubit B. a) Spectral component of first side peak (p=1), that appears due to continuous wave mixing with two drives of unequal amplitudes, as a function of frequency for driving amplitudes V_+ ranging from 1 to 0.1 $(mW)^{1/2}$. b) $\sqrt{V_3/V_1}$ as a function of frequency. 146

6.10 Third peak method with equal driving powers: The absolute power W_0 sensed by qubits A, B, C, and D (Table 6.1) at 7.48 GHz as a function of (a) input power W_{in} and as a function of (b) output power W_{out}. The slope of the linear fit (solid red line) represents (a) attenuation and (b) gain in our measurement circuit. 146

6.11 Third peak method with unequal driving powers: The absolute power W_0 sensed by qubits A, B, C, and D (Table 6.1) at 7.48 GHz as a function of (a) input power W_{in} and as a function of (b) output power W_{out}. The slope of the linear fit (solid red line) represents (a) attenuation and (b) gain in our measurement circuit. 147

Chapter 1

Introduction

1.1 Overview of the thesis

First, I introduce basic concepts that are important in the field of quantum optics. I briefly cover superconductivity, circuit theory, superconducting qubits, and artificial atoms. Then, I discuss methods of describing the dynamics of open quantum systems.

This is followed by a chapter dedicated to experimental principles. I discuss design considerations of experimental sample chips and explain the fabrication process in detail. I present a typical measurement set-up and briefly discuss their components. Finally, I dedicate one sub-chapter to qubit characterisation.

Then, we move on to the main results obtained during my doctoral research: quantum wave mixing (QWM), coherent wave mixing on a three level atom, and the development of an absolute power sensor.

Wave mixing on a nonlinearity is a classical effect, that is well described in text books [6, 7]. However, once the classical nonlinearity is replaced by a single quantum scatterer, effects beyond classical physics are revealed.

First, we study continuous wave mixing on a quantum object and observe a symmetric spectrum with an infinite number of side peaks. Then, we investigate two regimes of QWM: Coherent wave mixing and quantum wave mixing with non-classical superposed states. In the former, two pulsed waves

with frequencies slightly detuned from each other are scattered on the single artificial atom resulting in a symmetric spectrum with an infinite number of side peaks. The amplitude of each of these peaks oscillates in time according to Bessel functions with the orders determined by the number of interacting photons. In the latter regime, a time delay between the two pulses is introduced causing a striking difference in the spectrum, which now exhibits a finite number of narrow coherent emission peaks. Furthermore, the spectrum in the latter regime is asymmetric with the number of positive frequency peaks (due to stimulated emission) always exceeding by one compared to the negative frequency peaks (due to absorption).

Then, we investigate a coherent frequency conversion scheme with a single three-level artificial atom. The scheme is based on three-wave mixing, which utilises the quantised energy levels of the artificial atom. We drive the three-level atom with two continuous drives corresponding to two transition frequencies of the atom and measure the coherent emission at the sum or difference frequency. The device may be used as a quantum router, coherently interconnecting quantum channels, in prospective quantum networks.

Another part of the thesis addresses the challenge of measuring the absolute power of a microwave signal in a transmission line at cryogenic temperatures which is critical for applications in quantum optics, quantum computing and quantum information. We demonstrate that a two-level system strongly coupled to the open space can act as a quantum sensor of absolute power. We realise the quantum sensor using a superconducting flux qubit that is strongly coupled to the environment. The quantum sensor is independent of dephasing of the two-level system.

I conclude with a summary and a brief outlook.

Chapter 2

Basic concepts

2.1 Superconductivity and the Josephson Effect

Over 100 years ago, in 1911, superconductivity was discovered by Heike Kamerlingh Onnes who investigated the properties of matter at low temperatures [8]. Onnes found that the electrical resistance of some metals dropped abruptly to zero at a material-dependent critical temperature T_C as illustrated in Fig. 2.1(a). This was confirmed by experiments with persistent currents in superconducting rings [9]. It was observed that currents through a superconducting ring placed inside a magnetic field and cooled below its critical temperature T_c persist to flow. Thus, perfect conductivity was achieved - a prerequisite for many applications such as high-current transmission lines or high-field magnets for example.

In 1933, Walther Meißner and Robert Ochsenfeld discovered another property of superconductivity, perfect diamagnetism [10]. They found that not only a magnetic field cannot enter a superconductor, but also would be expelled from the superconductor as it is cooled through T_C. This is known as the Meißner effect. Since it is a reversible effect, it implies that superconductivity will be destroyed by a critical magnetic field H_C, which is related thermodynamically to the free-energy difference between the normal and superconducting states in zero field.

These two basic properties of superconductivity, perfect conductivity and perfect diamagnetism, were well described by Fritz and Heinz London in 1935 [11]. However, their theory was phenomenological and lacked to explain its fundamental origin. The next break-through in understanding superconductivity was the establishment of the existence of an energy gap Δ, of order kT_C, between the ground state and the quasi-particle excitations of the system. Measurements of the specific heat of superconductors [12] and of electromagnetic absorption in the region of $\hbar\omega \sim kT_C$ [13, 14] led Bardeen, Cooper, and Schrieffer (BCS) to formulate a pairing theory of superconductivity [15]. In BCS theory electrons pair into Cooper pairs with zero total spin and momentum and are condensed into a single macroscopic state described by a wavefunction $\psi(\mathbf{r}, t)$ (where $\mathbf{r}$ is the spatial variable, and t is time). The minimum energy $E_g = 2\Delta(T)$ to break a Cooper pair into two quasi-particle excitations was predicted by the BCS theory (Fig. 2.1(c-d)). Moreover, the theory stated that the energy gap $\Delta(T)$ should increase from zero at T_C to $E_g(0) = 2\Delta(0) = 3.528kT_C$ for $T << T_C$ (where k is the Boltzmann constant). These predictions not only matched the measurements of the gap widths but also agreed with the measurements of the shape of the absorption edge above $\hbar\omega_g = E_g$.

Both the London equations and BCS theory failed to include spacial variations of the properties of the material. Ginzburg and Landau considered this in their theory which they first proposed in 1950, even before the BCS theory, but the Ginzburg-Landau theory did not receive its deserved attention until it was shown that it could be derived from a generalised BCS theory [16]. Ginzburg and Landau introduced ψ (describing the superconducting electrons) as a complex order parameter linking the superconducting electrons to the local density of superconducting electrons n_S in the material via $n_S = |\psi(x)|^2$ [17]. Their theory also introduced the coherence length ξ, which characterises the length scale over which $\psi(\mathbf{r})$ can vary without excessive energy increase.

The finite coherence length ξ means that at the interface of a supercon-

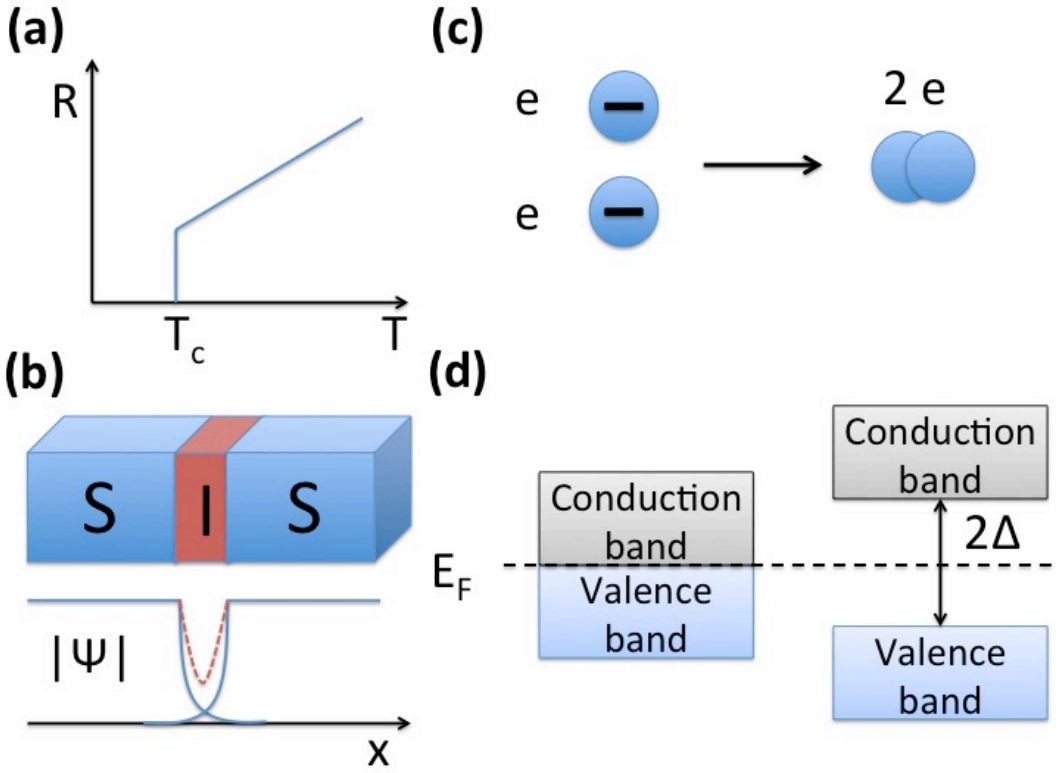

Figure 2.1: Superconductivity and the Josephson effect. (a) The resistance of some metals drops abruptly to zero at the critical temperature. (b) Leakage and interference of macroscopic wavefunctions of two superconductors in an SIS junction (c) Formation of Cooper pairs in BCS theory. (d) The electron spectrum: (on the left) in normal metals at $T = 0$ and (on the right) in superconductors at $T << T_c$ with the superconducting gap 2Δ.

ductor (S) and a normal metal (N) or insulator (I), some Cooper pairs will penetrate through the non-superconducting material. Moreover, when a very thin N- or I-layer is sandwiched between two superconductors, macroscopic wavefunctions of the two superconductors would interfere as schematically shown in Fig. 2.1(b). In 1962, Brian Josephson [18] predicted that Cooper pairs tunnel through such a junction, a Josephson junction, even at zero voltage difference, giving rise to a supercurrent

$$I_s = I_C sin(\delta). \tag{2.1}$$

where I_C is the maximum supercurrent the junction can sustain and δ is the

phase difference between the two superconductors. In the presence of a voltage difference V between the superconductors, the phase difference δ evolves with time according to

$$\dot{\delta} = \frac{2eV}{\hbar} = \frac{2\pi V}{\Phi_0}, \tag{2.2}$$

so that the current oscillates with frequency $\omega = 2eV/\hbar$. Here e is the magnitude of the electron charge and Φ_0 is the magnetic flux quantum arising from the periodic boundary conditions causing $\psi(\mathbf{r}, t) = |\psi(\mathbf{r})|e^{i\phi(\mathbf{r})}$ to be single valued. After switching off the magnetic field, the magnetic flux ϕ in a closed superconducting ring - maintained by the circulating persistent current - is quantised in integer values of the flux quantum $\Phi_0 = h/2e \approx 2.07x10^{-15}$ Tm^2. This was experimentally verified in 1961 [19]. Equations 2.1 and 2.2 are known as first and second Josephson equations, respectively and imply that the Josephson junction is intrinsically a nonlinear inductance. This can be seen by differentiating Eq. 2.1 with respect to time giving $\dot{I} = I_0 cos(\delta)\dot{\delta}$ and substituting Eq. 2.2 to give $\dot{I} = (2\pi V I_0 cos(\delta))/\Phi_0$. Comparing this result with Faraday's law $V = L\dot{I}$ leads to the Josephson inductance

$$L_J = \frac{\Phi_0}{2\pi I_0 cos(\delta)}. \tag{2.3}$$

The energy stored in a Josephson junction can be derived from $U_J = \int I_s V dt$ and using Eqns. 2.1, 2.2 to yield

$$U_J(\delta) = E_J[1 - cos(\delta)], \tag{2.4}$$

with the Josephson energy $E_J = \hbar I_c/2e$ and where the constant of integration was chosen such that $U_J(\delta)$ has a minimum of 0 in the case of a vanishing phase difference (in bulk superconductors). This is known as the washboard potential shown in Fig. 2.2(b). Since a Josephson junction geometrically resembles a plate capacitor, the total energy stored in the junction must also include the

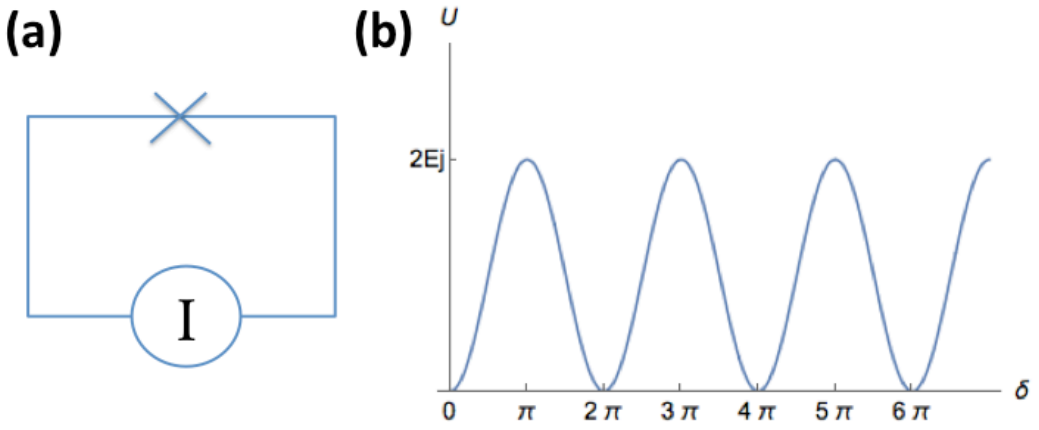

Figure 2.2: (a) Current biased Josephson junction denoted as an X and (b) its washboard potential $U_J(\delta) = E_J[1 - cos(\delta)]$.

electrostatic energy

$$T = \frac{Q^2}{2C} = E_C(N_c - N_g)^2, \tag{2.5}$$

where $E_C = 4e^2/2C$ is the charging energy describing the Coloumb energy of a single Cooper pair with charge $2e$ stored on the capacitor, N_C is the integer number of pairs that tunnel through the junction and N_g is an externally applied charge bias through a gate. The total Hamiltonian of the Josephson junction can be written as

$$H = T + U = \frac{Q^2}{2C} + E_J[1 - cos(\delta)]. \tag{2.6}$$

Comparing Eq. 2.6 with the classical Hamiltonian $H_{classical} = \frac{1}{2m}p^2 + U(x)$, it can be seen that the charge Q (or the number of Cooper pairs N) is analogoues to momentum p and the capacitance C acts like a mass m. And since the charge is related to the voltage by $Q = CV = C\dot{\Phi} = C^2\frac{\Phi_0}{2\pi}\dot{\delta}$, the Hamiltonian can be rewritten as $H = \frac{C\dot{\Phi}^2}{2} + E_J[1 - cos(\delta)]$. Comparing this to the classical Hamiltonian $H_{classical} = \frac{m}{2}\dot{x}^2 + U(x)$, one can see that the flux Φ (or the phase difference δ across the junction) corresponds to the classical position x. From this comparison, the commutator relations

$$[\hat{\Phi}, \hat{Q}] = i\hbar \tag{2.7}$$

$$[\hat{\delta}, \hat{N}] = \frac{2\pi}{\Phi_0}[\hat{\Phi}, \hat{Q}]\frac{1}{2e} = i \tag{2.8}$$

where the phase operator $\hat{\delta} = \frac{2\pi}{\Phi_0}\hat{\Phi}$, the number operator $\hat{N} = \frac{\hat{Q}}{2e}$, and the flux quantum $\Phi_0 = h/2e$ was substituted and the operators

$$\hat{Q} = -i\hbar\frac{\partial}{\partial\Phi} \tag{2.9}$$

$$\hat{N} = -i\frac{\partial}{\partial\delta} \tag{2.10}$$

follow. This representation considers flux (Φ) and flux motion ($\dot{\Phi} = Q/C$) in electric circuits. If we instead consider charge (Q) and the motion of charges ($\dot{Q} = \Phi/L$) in electric circuits and comparing it with the classical Hamiltonian, we find that charge Q, flux Φ, inductance L may also be the analog of position x, momentum p, and mass m respectively.

2.2 Qubits and quantum computing

Quantum bits, or in shorthand notation qubits, are the building blocks of quantum computers - an idea first introduced by Richard Feynman in 1982 [20]. Different to classical bits, a qubit cannot only be in two states, $|0\rangle$ or $|1\rangle$, but in an arbitrary state $|\psi\rangle$ that can be any linear superposition of the two basic states $|0\rangle$ and $|1\rangle$,

$$|\psi\rangle = \alpha\,|0\rangle + \beta\,|1\rangle\,, \tag{2.11}$$

where α and β are complex numbers satisfying the normalisation condition $|\alpha|^2 + |\beta|^2 = 1$. If we tried to determine the state of the qubit we would either measure $|0\rangle$ with probability $|\alpha|^2$, or $|1\rangle$ with probability $|\beta|^2$. It is instructive to think of a sphere with radius 1, the Bloch sphere, since the normalisation condition can be interpreted geometrically as a unit vector in a two-dimensional complex vector space. Eq. 2.11 may be rewritten as

$$|\psi\rangle = cos\frac{\theta}{2}\,|0\rangle + e^{i\phi}sin\frac{\theta}{2}\,|1\rangle\,, \tag{2.12}$$

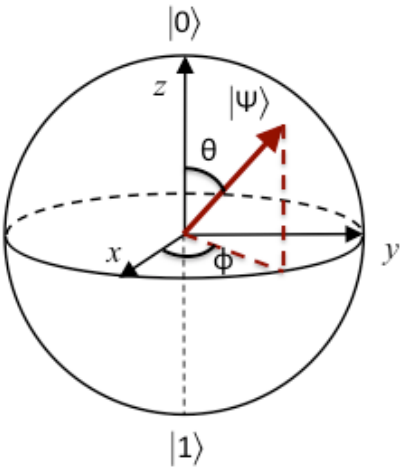

Figure 2.3: Bloch sphere. Any arbitrary qubit state can be represented as a point on the unit sphere.

where θ and ϕ are polar and azimuthal angles in spherical coordinates respectively defining a point on the Bloch sphere [21], as shown in Fig. 2.3. The two basis states $|0\rangle$ and $|1\rangle$ are at the north and south pole respectively. Points on the Bloch sphere can be used to represent any pure state $|\psi\rangle$ while any points inside the Bloch sphere represent mixed states.

The Bloch sphere serves as an excellent tool to visualise single qubit operations. Any point on the unit sphere can be transferred to any other point by rotation about the $\mathbf{n} = [sin\theta cos\phi, sin\theta sin\phi, cos\theta]$ axis by angle γ, described by the unitary $2x2$ matrix

$$\hat{R}_{\mathbf{n}}(\gamma) = e^{\frac{i\gamma}{2}\mathbf{n}\cdot\sigma}, \tag{2.13}$$

where $\sigma = [\sigma_x, \sigma_y, \sigma_z]$ are the Pauli matrices. This represents an arbitrary transformation of a single qubit that is often referred to as a gate in analogy with classical computing. A gate transforms the initial qubit state $|i\rangle$ to the final state $|f\rangle = \hat{R}\,|i\rangle$. Similar to classical computing, information is stored in string of bits, but here we speak about quantum information stored in string of qubits. Unfortunately, there is no simple generalisation of the Bloch sphere for multiple qubits.

The wave function of N qubits is a superposition of the basis states $|j\rangle$

and scales with 2^N independent complex components f_j such that

$$|f\rangle = \sum_{j=0}^{2^N-1} f_j \, |j\rangle \, ; \quad \text{with} \quad \sum_j |f_j|^2 = 1. \tag{2.14}$$

Performing certain quantum algorithms [22, 23] using N-qubit gates or a combination of single - and two-qubit gates can lead to speed-ups compared to classical computing. This is highly motivating to implement a quantum computer. Di Vincenzo formulated criteria for a successful implementation of quantum computing [24]. This includes the realisation of a qubit that is long-lived, controllable and scalable. Qubits have been demonstrated in NMR systems [25, 26], trapped ions [27, 28], photons [29, 30], and in electrical circuits [31].

2.3 Superconducting qubits

Superconducting qubits are fabricated on chip using well established lithography techniques allowing for energy levels to be engineered. Multiple qubits can be printed on one chip and integrated on a solid-state platform. This potential scalability of superconducting qubits is one of their biggest advantages over other systems. Another benefit of the superconducting circuit platform is that the strong coupling regime can be easily achieved [32], since they are operating in one-dimensional space.

There are several different approaches of implementing a qubit with superconducting circuits [33, 34, 35, 31, 36, 37]. In most of them Josephson junctions are used as a nonlinear element to provide anharmonicity.

2.3.1 Charge based qubits

The simplest design of a superconducting qubit, known as the Cooper pair box (CPB), was first theoretically described by M. Büttinger [38] in 1987 and experimentally realised for the first time in 1997 by the NEC and Saclay group [39, 40]. Quantum dynamics in the time domain of the Cooper pair box was first observed by the NEC group in 1999 [31].

The Cooper pair box consists of a superconducting island with capacitance C connected to a reservoir of Cooper pairs through a Josephson junction. Cooper pairs can tunnel between the island and reservoir through the Josephson junction. If a voltage gate V_g is added to the circuit capacitatively through C_g, then the tunneling can be modulated. A typical Cooper pair box is shown schematically in Fig. 2.4(a).

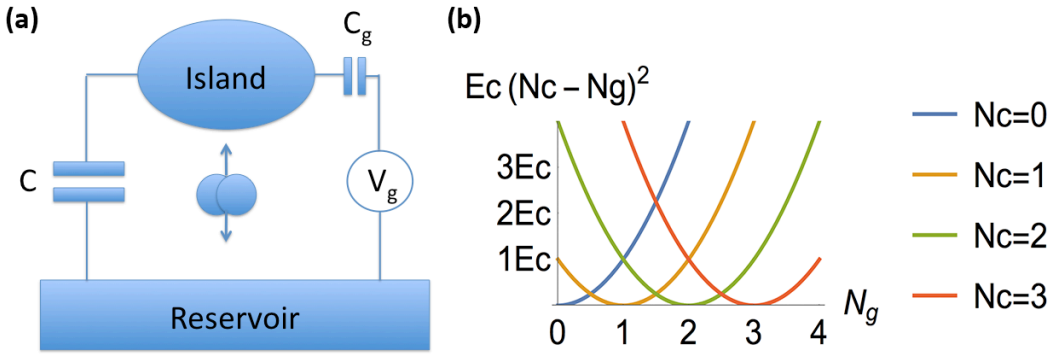

Figure 2.4: (a) Schematic circuit and (b) electrostatic energies of the Cooper pair box (CPB).

The charging energy $E_C = 4e^2/2(C + C_g)$ and the Josephson energy $E_J\hbar I_c/2e$ characterise the system's Hamiltonian

$$H = E_C(N_c - N_g)^2 - E_J cos(\delta) \tag{2.15}$$

where N_C is the integer number of pairs that tunnel through the junction and N_g is an externally applied charge bias through the voltage gate V_g. Introducing the $\hat{N}$- and phase operator $\hat{\delta}$

$$\hat{N} = \sum_N |N\rangle \langle N| , \tag{2.16}$$

$$\begin{aligned} e^{i\hat{\delta}} &= \sum_N |N+1\rangle \langle N| , \\ e^{-i\hat{\delta}} &= \sum_N |N-1\rangle \langle N| \end{aligned} \tag{2.17}$$

and expressing the cosine in the exponential form allows to rewrite the Cooper

pair box Hamiltonian (eq. 2.15) to

$$H = \sum_N \left[E_C(N_c - N_g)^2 \left|N\right\rangle \left\langle N\right| - \frac{E_J}{2} \left(\left|N+1\right\rangle \left\langle N\right| + \left|N-1\right\rangle \left\langle N\right| \right) \right]. \quad (2.18)$$

In the charging regime $E_C >> E_J$, Eq. 2.18 can be truncated to a two-level system

$$H = -\epsilon(N_g)\sigma_z - \frac{E_J}{2}\sigma_x \quad (2.19)$$

where $\epsilon = E_c(N_g - 1/2)$ and the Pauli matrices $\sigma_z = \left|0\right\rangle \left\langle 0\right| - \left|1\right\rangle \left\langle 1\right|$, $\sigma_x = \left|0\right\rangle \left\langle 1\right| + \left|1\right\rangle \left\langle 0\right|$ are defined in terms of the two basis states corresponding to zero and one extra Cooper pair in the box. Figure 2.5 shows the energy spectrum of the Cooper pair box for different ratios of E_J/E_C. The transmon

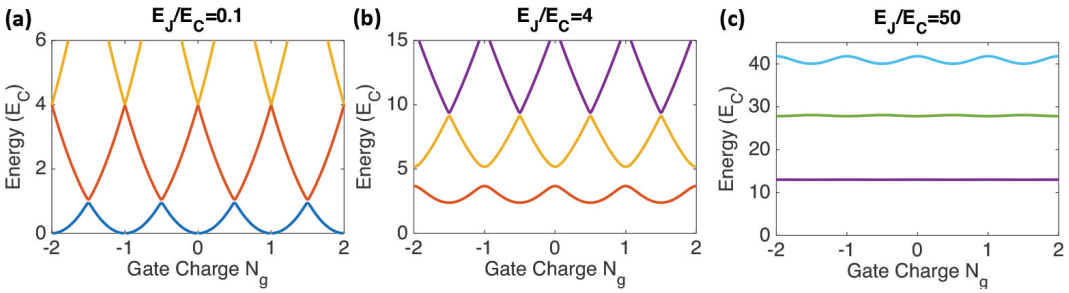

Figure 2.5: Energy spectrum of the Cooper pair box for the ratio (a) $E_J/E_C = 0.1$, (b) $E_J/E_C = 4$, and (c) $E_J/E_C = 50$.

qubit [41, 42] is a Cooper pair box with a large capacitance in parallel to the Josephson junction. This reduces the charging energy E_C, such that the device is operating in the flux regime $E_J >> E_C$. As can be seen in Fig 2.5(c) the energy bands become flat in this regime. This means the charge sensitivity of the device is low, increasing coherence times of the qubit. However, anharmonicity is reduced in this regime ($E_J >> E_C$) increasing the chance of driving errors of the qubit.

2.3.2 The RF-squid

In the RF-squid the Josephson junction with capacitance C is connected through a superconducting loop with inductance L as schematically shown in Fig. 2.6(a). Compared to the CPB, the RF-squid has a large inductance,

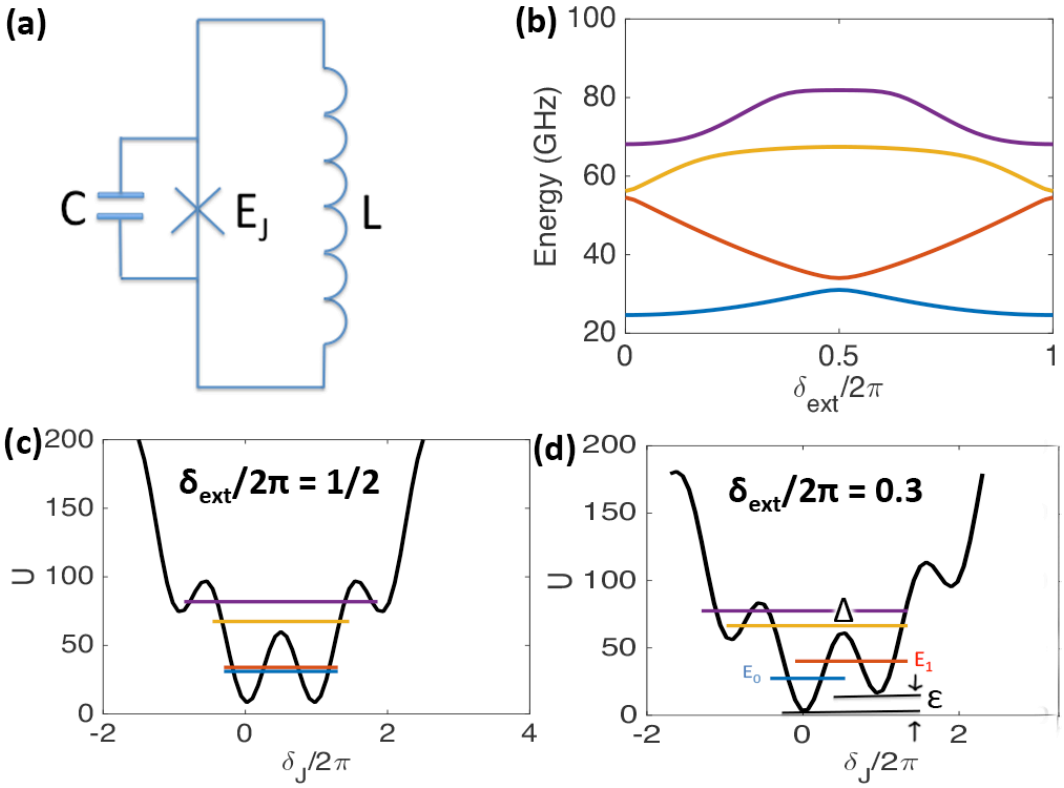

Figure 2.6: (a) Circuit diagram of the RF-Squid. (b) Energy spectrum of the first four levels of the RF-squid with $E_L/h = 70$ GHz, $E_J/h = 30$ GHz, and $E_C/h = 100$ GHz. (c-d) Potential of the RF-squid for $\delta_{ext} = \pi$ and $\delta_{ext}/2\pi = 0.3$ respectively with the first few energy levels.

whose energy E_L is comparable to E_J and E_C (which was neglected in the CPB). The potential energy of the RF-squid is given by

$$U = -E_J cos(\delta_J) + \left(\frac{\Phi_0}{2\pi}\right)^2 \frac{\delta_L^2}{2L} \tag{2.20}$$

where the first term is associated with the energy stored in the Josephson junction and the second term describes the inductive energy. Here δ_J and δ_L are the phase differences across the junction and inductance respectively. Instead of a voltage gate in the CPB, the RF-squid is biased by an external flux Φ_{ext} such that $\Phi_J + \Phi_L = \Phi_{ext}$. Recalling the flux-phase relation $\Phi = \frac{\Phi_0}{2\pi}\delta$, we can substitute $\delta_L = \delta_{ext} - \delta_J$ and $E_L = \left(\frac{\Phi_0}{2\pi}\right)^2 \frac{1}{2L}$ into eq. 2.20 to obtain

the full Hamiltonian

$$H = -E_c \frac{\partial^2}{\partial \delta_J^2} - E_J cos(\delta_J) + E_L(\delta_{ext} - \delta_J)^2, \tag{2.21}$$

where the kinetic energy term $\frac{Q^2}{2C}$ is expressed in terms of the phase difference δ_J across the junction by substituting $Q = 2e\hat{N}$, $\hat{N} = -i\frac{\partial}{\partial \delta}$ (eq. 2.10), and $E_C = \frac{4e^2}{2C}$.

The potential has a parabolic shape with cosine oscillations and is generally asymmetric unless $\Phi_{ext} = \Phi_0/2$. At this point, the two lowest energy levels are degenerate, and are symmetric ($|+\rangle$) and anti-symmetric ($|-\rangle$) combinations of the wavefunctions localised in each well. The energy splitting (Δ) between the the two states can be interpreted as the coupling through the potential barrier between the two wells. Slightly detuned from $\Phi_{ext} = \Phi_0/2$ or equally $\delta_{ext} = \pi$, the energy difference between the two lowest states (located at $\delta_J = 0$ and $\delta_J = 2\pi$) can be defined as $\epsilon = E_1 - E_0 = 4\pi E_L[\delta_{ext} - \pi]$ and an approximate two-level Hamiltonian may be written

$$H \approx -\frac{\epsilon}{2}\sigma_z - \frac{\Delta}{2}\sigma_x. \tag{2.22}$$

Fig. 2.6(c-d) show the potential together with the first few energy levels, which have been experimentally observed for the first time in 1999 [43].

2.3.3 The flux qubit

The flux qubit is based on the RF-squid and consists of a superconducting loop interrupted by one [44], three [45] or four [32] Josephson Junctions (JJ). Although these designs operate similarly, I will concentrate on the four-junction flux qubit which I predominately work with. In this device, three JJs are made identical to each other, while the fourth one, called α-junction, is a fraction (α) smaller in the area overlap and has therefore smaller critical current than the remaining three. The ratio of $\frac{E_J}{E_C} >> 1$ is typically much larger than unity. This means that the magnetic flux (Φ) or the phase difference (δ) in the loop is

the relevant quantum variable. The two lowest eigenstates of the flux qubit are naturally expressed via superpositions of two states with persistent current, I_p, circulating clockwise or counterclockwise in the loop. The qubit is represented by a double-well potential, which is generally asymmetrical. The two states are coupled by quantum-mechanical tunnelling of the phase difference through the barrier separating the wells, giving rise to the superposition of the two basis states.

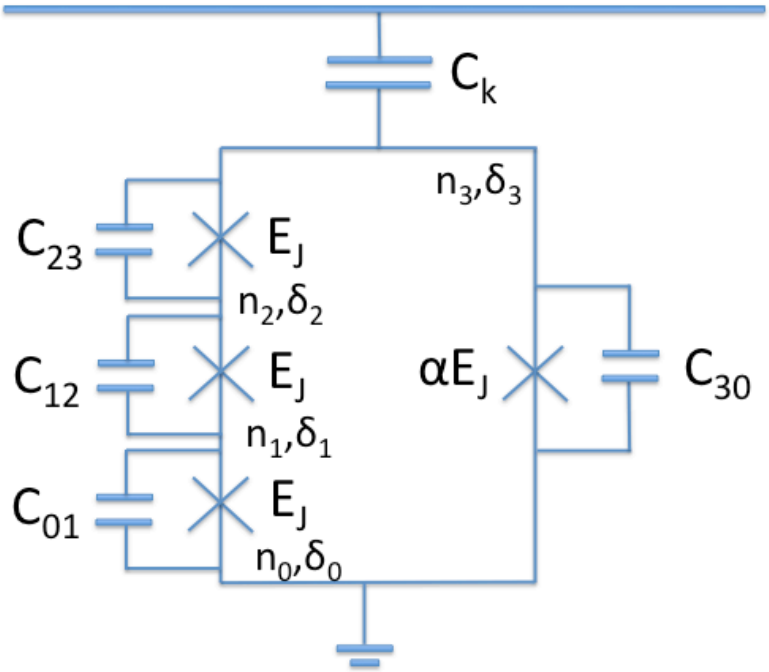

Figure 2.7: Schematic circuit representation of a four junction flux qubit capacitatively coupled through a capacitance C_k to a transmission line.

In electrical circuit theory it is useful to work with node fluxes $\Phi_i(t) = \int_\infty^t V_i(t')dt'$ and node charges $Q_i(t) = \int_\infty^t I_i(t')dt'$ where each node i carries the current $I_i(t)$ and causes a voltage drop $V_i(t)$. Most superconducting circuits can be modelled by various combinations of capacitive and inductive elements. Recalling the relation $\Phi = \frac{\Phi_0}{2\pi}\delta$ and $Q = -2eN$, each node can also be expressed in terms of the superconducting phase δ_i and integer charge n_i as indicated on the schematic circuit representation of a 4-JJ flux qubit in Fig 2.7. Similar to the RF-squid, the 4-JJ flux qubit is biased by an external flux $\Phi_{ext} = \frac{\Phi_0}{2\pi}\delta_{ext}$

such that $\delta_{ext} = \delta_{01} + \delta_{12} + \delta_{23} + \delta_{30}$ where $e^{i\delta_{ij}} = e^{i(\delta_i - \delta_j)}$ are the phase differences between the nodes. The total potential energy comes from all four JJ's

$$U = E_J[3 + \alpha - cos\delta_{01} - cos\delta_{12} - cos\delta_{23} - \alpha cos(\delta_{ext} - \delta_{01} - \delta_{12} - \delta_{23})]. \quad (2.23)$$

The potential landscape of a 4-JJ flux qubit is shown in Fig. 2.8(a-b), in which we can identify a double-well potential. The height of the potential barrier is determined by α as shown in Fig. 2.8(c) while the external flux Φ_{ext} determines the shape of the potential as seen in Fig 2.8(d). When the externally applied magnetic flux is half flux quantum, the double-well potential becomes symmetrical, and the two eigenfunctions become symmetrical ($|+\rangle$) and asymmetrical ($|-\rangle$) superpositions of the two basis states.

To calculate the energy levels of an arbitrary 4-JJ flux qubit that is coupled capacitavely to the transmission line schematically shown in Fig. 2.7, the Schrödinger equation has to be solved. We may start by writing down the Hamiltonian $H = T + U$ where U is the potential energy, that we have already found (see eq. 2.23), and $T = \frac{QV}{2}$ is the electrostatic energy. It is useful to construct a capacitance matrix

$$C = \begin{pmatrix} C_{01} + C_{12} & -C_{12} & 0 \\ -C_{12} & C_{12} + C_{23} & -C_{23} \\ 0 & -C_{23} & C_{23} + C_{30} + C_k \end{pmatrix} \quad (2.24)$$

for the system that links a given integer number charge vector $\vec{n}$ with a potential vector $\vec{V}$ via

$$\vec{n} = \frac{C\vec{V}}{2e}, \quad (2.25)$$

where

$$\vec{n} = \begin{pmatrix} n_1 \\ n_2 \\ n_3 \end{pmatrix}, \quad \vec{V} = \begin{pmatrix} V_1 \\ V_2 \\ V_3 \end{pmatrix}, \quad (2.26)$$

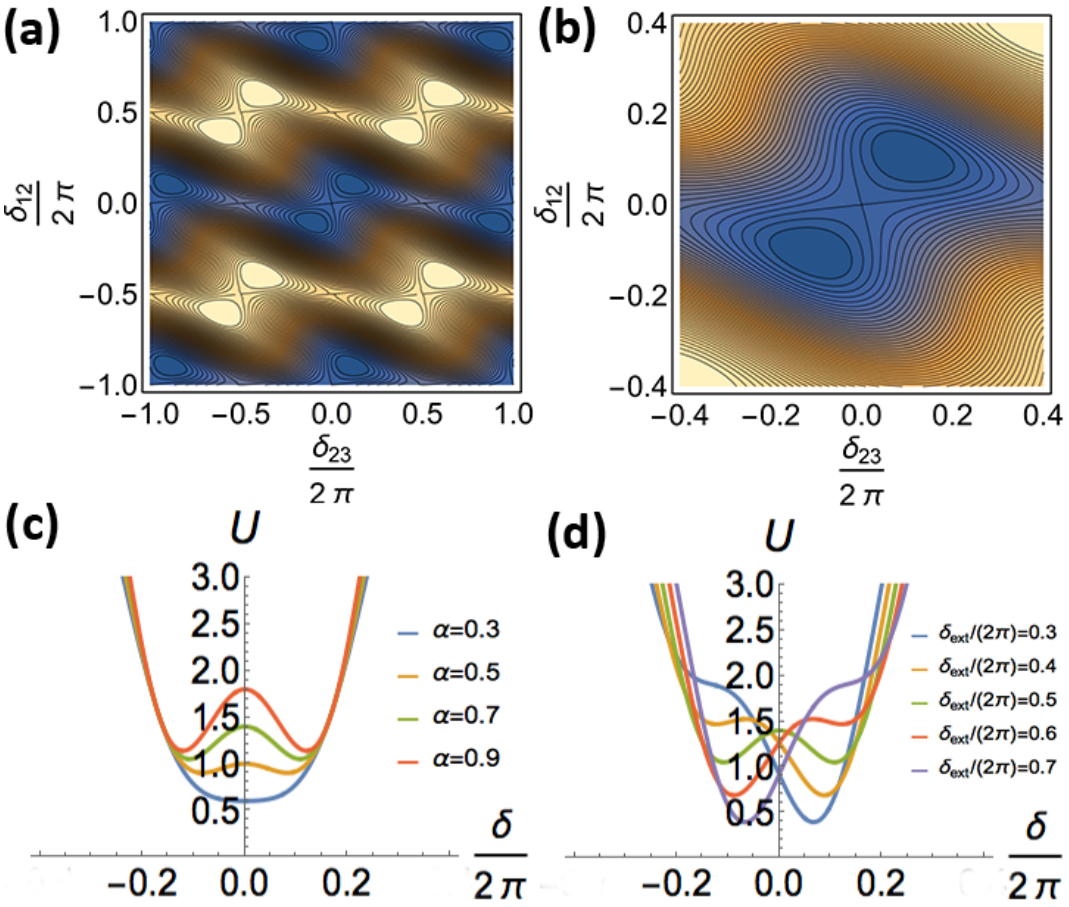

Figure 2.8: Potential of four-JJ flux qubit U/E_J (a-b) for $\alpha = 0.7$, $\delta_{23} = \delta_{12}$ at $\delta_{ext} = \pi$, (c) for α ranging from 0.3 to 0.9 at $\delta_{ext} = \pi$ where $\delta = \delta_{01} = \delta_{12} = \delta_{23}$, (d) for $\delta = \delta_{01} = \delta_{12} = \delta_{23}$, $\alpha = 0.7$ at $\delta_{ext}/2\pi$ ranging from 0.3 to 0.7.

since the charge can be expressed in terms of the number of Cooper pairs tunnelling from one node to another $Q = 2e\vec{n}$ or in terms of the charge on a capacitor $Q = C\vec{V}$. The kinetic energy term can then be written as

$$T = \frac{QV}{2} = \frac{1}{2}(2e\vec{n}^T)(2eC^{-1}\vec{n}) \tag{2.27}$$

leading to the full 4-JJ flux qubit Hamiltonian

$$H = \frac{1}{2}(2e)^2\vec{n}^T C^{-1}\vec{n} + E_J[3+\alpha-cos\delta_{01}-cos\delta_{12}-cos\delta_{23}-\alpha cos(\delta_{ext}-\delta_{01}-\delta_{12}-\delta_{23})]. \tag{2.28}$$

To solve the Schrödinger equation $H|\Psi\rangle = E|\Psi\rangle$, it is instructive to rewrite

the Hamiltonian (eq. 2.28) in the charge basis n

$$\begin{aligned} H =& \frac{4e^2}{2} \sum_{n_1,n_2,n_3}^{\infty} \overrightarrow{n}^T C^{-1} \overrightarrow{n} \left|n_1, n_2, n_3\right\rangle \left\langle n_1, n_2, n_3\right| \\ & - \frac{E_J}{2} \sum_{n_1,n_2,n_3}^{\infty} \Big[\left|n_1 - 1, n_2, n_3\right\rangle \left\langle n_1, n_2, n_3\right| + \left|n_1 + 1, n_2, n_2\right\rangle \left\langle n_1, n_2, n_3\right| \\ & + \left|n_1 + 1, n_2 - 1, n_3\right\rangle \left\langle n_1, n_2, n_3\right| + \left|n_1 - 1, n_2 + 1, n_3\right\rangle \left\langle n_1, n_1, n_3\right| \\ & + \left|n_1, n_2 + 1, n_3 - 1\right\rangle \left\langle n_1, n_2, n_3\right| + \left|n_1, n_2 - 1, n_3 + 1\right\rangle \left\langle n_1, n_2, n_3\right| \\ & + \left|n_1, n_2, n_3 + 1\right\rangle \left\langle n_1, n_2, n_3 - 1\right| \left\langle n_1, n_2, n_3\right| \Big] \end{aligned} \tag{2.29}$$

where I have used the $\hat{N}$- (eq. 2.16) and phase operators (eq. 2.17) to express the cosine terms in exponential form. The Hamiltonian (eq. 2.29) in matrix form is

$$H = \begin{pmatrix} \ddots & \vdots & \vdots & \vdots & \vdots & \vdots & \vdots & \vdots & \\ \cdots & T(-1,0,0) & -\frac{E_J}{2} & 0 & -\frac{E_J}{2} & 0 & 0 & 0 & \cdots \\ \cdots & -\frac{E_J}{2} & T(0,-1,0) & 0 & -\frac{E_J}{2} & 0 & 0 & 0 & \cdots \\ \cdots & 0 & -\frac{E_J}{2} & T(0,0,-1) & -\frac{\alpha E_J}{2} & -\frac{E_J}{2} & 0 & 0 & \cdots \\ \cdots & -\frac{E_J}{2} & -\frac{E_J}{2} & -\frac{\alpha E_J}{2} & T(0,0,0) & -\frac{\alpha E_J}{2} & -\frac{E_J}{2} & -\frac{E_J}{2} & \cdots \\ \cdots & 0 & 0 & 0 & -\frac{\alpha E_J}{2} & T(0,0,1) & -\frac{E_J}{2} & 0 & \cdots \\ \cdots & 0 & 0 & 0 & -\frac{E_J}{2} & -\frac{E_J}{2} & T(0,1,0) & 0 & \cdots \\ \cdots & 0 & 0 & 0 & -\frac{E_J}{2} & 0 & 0 & T(1,0,0) & \\ & \vdots & \vdots & \vdots & \vdots & \vdots & \vdots & \vdots & \ddots \end{pmatrix} \tag{2.30}$$

where the diagonal terms are $T(n_1, n_2, n_3) = \frac{4e^2}{2} \sum_{n_1,n_2,n_3}^{\infty} \overrightarrow{n}^T C^{-1} \overrightarrow{n} \left|n_1, n_2, n_3\right\rangle \left\langle n_1, n_2, n_3\right|$. To calculate the eigenenergies for an arbitrary four-JJ flux qubit numerically, we need to truncate the Hamiltonian to a finite size with number of charge states N_{ch}. This corresponds to summing up to N_{ch} instead of infinity in eq. 2.29. The diagonal terms can be simplified by noting that three JJ are equal, and therefore have equal capacitances such that $C_J = C_{01} = C_{12} = C_{23}$,

whereas the fourth JJ is by α smaller in overlap and therefore its capacitance is by α smaller, such that $C_{30} = \alpha C_J$. Fig. 2.9 shows the numerically sim-

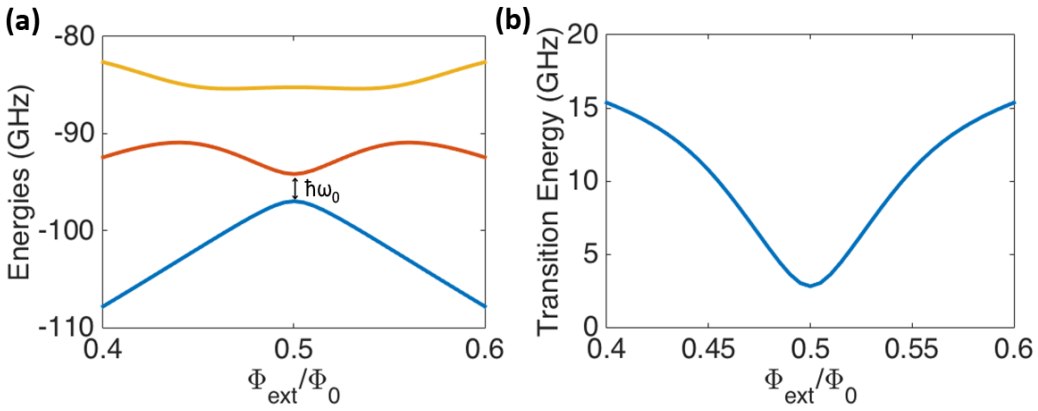

Figure 2.9: (a) First three energy bands and (b) first transition energy of a 4-JJ flux qubit with $E_J/h = 50GHz$, $C_J = 5fF$, $\alpha = 0.5$ as a function of external flux numerically simulated in Matlab.

ulated energy levels and the transition energy f_{12} of a 4-JJ flux qubit with $E_J/h = 50GHz$, $C_J = 5fF$, $\alpha = 0.5$ as a function of external flux. At $\Phi_{ext}/\Phi_0 = 0.5$, where the double-well potential is symmetric, the splitting of the energy levels of the ground and first excited state is ω_0. Away from the degeneracy point ($\Phi_{ext}/\Phi_0 \neq 0.5$), the energy difference is $\delta E = \hbar\sqrt{\omega_0^2 + \epsilon^2}$ where $\epsilon = \frac{2I_p}{\hbar}(\Phi_{ext} - \frac{\Phi_0}{2})$ is the energy bias controlled by the external flux and proportional to the persistent current I_p in the flux qubit loop. If the qubit parameters are chosen such that the excitation energies of the third and higher eigenstates are much larger than δE, the Hamiltonian can be truncated to a two-level system $H = \frac{\delta E}{2}\sigma_z = \frac{\hbar\omega_a}{2}\sigma_z$ where $\omega_a = \sqrt{(\omega_0^2 + \epsilon^2)}$ is the atomic transition frequency.

2.4 Artificial atoms

From the previous sections, we have learned that the energy bands of superconducting qubits can be engineered by tuning their design parameters, such as the charging energy E_C, the Josephson energy E_J, or the difference in junction overlap α for example. This means that we not only can fabricate an effective two-level system, but in fact can also engineer multi-level systems us-

ing superconducting circuits. For this reason, these superconducting circuits are often called artificial atoms.

2.5 Quantum dynamics of open systems

Quantum dynamics of any isolated or closed system is governed by unitary evolution of the Schrödinger equation. Here, however, we are interested in the quantum dynamics of an atom that is not isolated but in open space or equivalently an artificial atom coupled to a one-dimensional transmission line.

2.5.1 The transmission line

A microwave transmission line can be treated as a perfectly conducting wire with inductance per unit length l and capacitance per unit length c as shown in Fig. 2.10. At position x and time t, there are left- and right- propagating

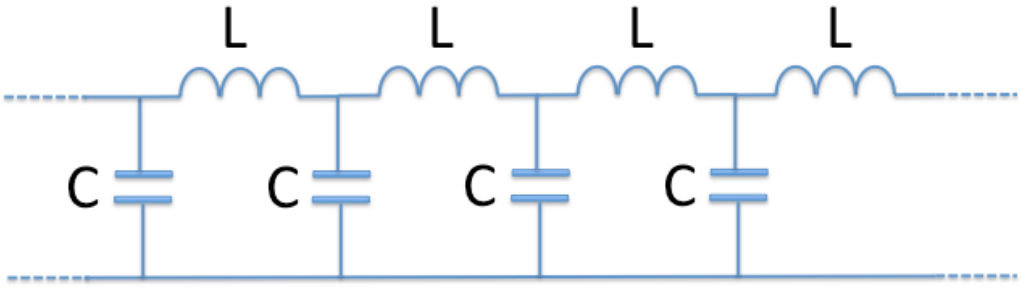

Figure 2.10: Schematic circuit representation of a transmission line modelled as a chain of inductances L and capacitances C.

voltage and current modes in the transmission line

$$\begin{aligned} V_{\pm}(x,t) &= V_0 e^{\pm ikx - i\omega t}, \\ I_{\pm}(x,t) &= I_0 e^{\pm ikx - i\omega t}, \end{aligned} \tag{2.31}$$

which are related to each other via the complex impedance $Z_{\pm} = V_{\pm}(x,t)/I_{\pm}(x,t)$. Substituting eqns. 2.31 into the Telegraphers equations

$$\begin{aligned} \frac{\partial V}{\partial x} &= -l\frac{\partial I}{\partial t}, \\ \frac{\partial I}{\partial x} &= -c\frac{\partial V}{\partial t}, \end{aligned} \tag{2.32}$$

we can see that $Z_0 = \sqrt{l/c}$ and differentiating eq. 2.32 leads to

$$\frac{\partial^2 V}{\partial x^2} = \frac{1}{1/lc}\frac{\partial^2 V}{\partial t}, \tag{2.33}$$

where $1/\sqrt{lc}$ is the wave phase velocity. If we ground one end of the transmission line ($x = 0$), we can impose the boundary condition $I(0,t) = 0$ and arrive to the analog of a mirror in open space. A microwave resonator can be created by introducing two gaps in the transmission line ($x = 0$, $x = L$) with boundary conditions $I(0,t) = I(L,t) = 0$.

2.5.2 The density matrix formalism

In open systems, the atom constantly interacts with the quantum fluctuations of the environment. Due to these interactions the quantum system may become entangled with the environment and therefore the density matrix formalism is required. A general density operator of a system consisting of n states $|\psi_j\rangle$ with probability p_j can be written

$$\rho = \sum_j^n p_j \left|\psi_j\right\rangle \left\langle\psi_j\right|, \tag{2.34}$$

or in terms of an orthonormal basis vectors $|\phi_j\rangle$

$$\rho = \sum_{j,k} \rho_{j,k} \left|\phi_j\right\rangle \left\langle\phi_k\right| \tag{2.35}$$

where $\rho_{j,k} = \langle\phi_j| \rho |\phi_k\rangle$ are the matrix elements of the matrix representation. The density matrix evolves under unitary transformations ($\rho(t) = U(t)\rho U(t)^\dagger$). Every density operator ρ is hermitian ($\rho = \rho^\dagger$), has unit trace ($Tr(\rho) = 1$), and is a positive operator ($\rho \geq 0$). Using the density matrix formalism the expectation value for an operator $\hat{O}$ is given by $\langle\hat{O}\rangle = \sum Tr(\hat{O}\rho)$. The formalism also classifies pure and mixed states. Taking the trace of the squared density matrix is a measure of purity. For pure states $Tr(\rho^2) = 1$, while for mixed

states $Tr(\rho^2) < 1$. Calculating the expectation values of the Pauli matrices

$$\begin{aligned}
\langle\sigma_z\rangle &= Tr(\sigma_z\rho) = \rho_{00} - \rho_{11}, \\
\langle\sigma_x\rangle &= \rho_{01} + \rho_{10}, \\
\langle\sigma_y\rangle &= i(\rho_{01} - \rho_{10}), \\
\langle\sigma_+\rangle &= \frac{\langle\sigma_x\rangle + i\langle\sigma_y\rangle}{2} = \rho_{10}, \\
\langle\sigma_-\rangle &= \frac{\langle\sigma_x\rangle - i\langle\sigma_y\rangle}{2} = \rho_{01},
\end{aligned} \tag{2.36}$$

helps to understand the link to the Bloch sphere (Fig. 2.3), that was introduced in section 2.2. Since every density operator has unit trace, we can express

$$\begin{aligned}
\rho_{00} &= \frac{1 + \langle\sigma_z\rangle}{2}, \\
\rho_{11} &= \frac{1 - \langle\sigma_z\rangle}{2}.
\end{aligned} \tag{2.37}$$

The density matrix may also be expressed in terms of the Bloch vector $\vec{r}$,

$$\rho = \frac{\mathbf{I} + \vec{r}\cdot\vec{\sigma}}{2}, \tag{2.38}$$

with $|\vec{r}| \leq 1$. Then any point on the surface of the Bloch sphere ($|\vec{r}| = 1$) represents a pure state $|\psi\rangle$ while any vector within the Bloch sphere ($\vec{r} < 1$) represents a mixed state.

2.5.3 The master equation

One method to treat open quantum systems is the master equation approach, which assumes a Markovian evolution. This means that the evolution of the system only depends on its reduced state at time t. From the definition of the derivative

$$\dot{\rho}(t) = \lim_{\delta t \to 0} \frac{\rho(t + \delta t) - \rho(t)}{\delta t}, \tag{2.39}$$

and in the limit of $\delta t \to 0$

$$\rho(t + \delta t) = \rho(t) + \dot{\rho}(t)\delta t, \tag{2.40}$$

which shows that an evolution in the form of eq. 2.40, only depends on $\rho(t)$, the state of the system immediately before. Such type of evolution is called Markovian. To derive the master equation, we also assume that the transformation from $\rho(0)$ to $\rho(\delta t)$ has a Kraus decomposition and the derivative of the density matrix can be written as

$$\rho(\delta t) = \sum_j K_j(\delta t)\rho(0)K_j^\dagger(\delta t). \tag{2.41}$$

Comparing $\rho(\delta) = \rho(0) + \delta t\dot{\rho}(0)$ with eq. 2.41, it can be seen that for them to be equal the one Kraus operators must be of the form $K_0 = \mathbf{I} + \delta A$ and the remaining of the form $K_j = \sqrt{\delta t}L_j$ where A and L_j are linear operators. Substituting these Kraus operators into eq. 2.41 and neglecting higher order terms gives

$$\rho(\delta t) = \rho(0) + \delta t\bigg(A\rho(0) + \rho(0)A^\dagger + \sum_{j+1}^{\infty} L_j\rho(0)L_j^\dagger\bigg). \tag{2.42}$$

Comparing eq. 2.42 with $\rho(\delta) = \rho(0) + \delta t\dot{\rho}(0)$, we can read off an expression for $\dot{\rho}(0)$. If we assume the evolution is constant in time and decomposing the operator A into $A = -\frac{i}{\hbar}H + M$ where H and M are Hermitian, we can find an expression for

$$M = -\frac{1}{2}\sum_{j=1}^{\infty} L_j^\dagger L_j, \tag{2.43}$$

and rewrite eq. 2.42

$$\dot{\rho}(t) = -\frac{i}{\hbar}[H_{eff}, \rho(t)] + \sum_{j=1}^{\infty} L_j^\dagger L_j, \tag{2.44}$$

where $H_eff = H - i\frac{\hbar}{2}\sum_{j=1}^{\infty} L_j^\dagger L_j$. This is the Markovian master equation in Lindblad form. If $L_j = 0$, then eq 2.44 reduces to the Von Neumann equation ($\dot{\rho} = -\frac{i}{\hbar}[H, \rho(t)]$) which describes the evolution of an isolated system. Therefore, H_{eff} can be interpreted as the Hamiltonian representing the system alone, without any interaction, and L_j operators (or jump operators) describe pro-

cesses associated with the interaction with the environment, such as relaxation Γ_1 and dephasing Γ_2.

2.5.3.1 Two-level atom interacting with a classical field

We may rewrite the master equation (eq. 2.44)

$$\dot{\rho}(t) = -\frac{i}{\hbar}[H, \rho(t)] + L[\rho], \tag{2.45}$$

and start by writing down the Hamiltonian of a two-level system with a classical interacting field $H = H_a + H_{int}$ where H_a is the time-independent Hamiltonian of the atom and H_{int} is the time-dependent atom field interaction. As we have shown before in eq 2.21, the Hamiltonian of a two-level system is $H_a = \frac{\hbar\omega_a}{2}\sigma_z$ where ω_a is the atomic transition frequency. We consider the atom interacting with a sinusoidal field, and write the interaction Hamiltonian in the dipole approximation as $H_{int} = \hbar\Omega cos(\omega t - \phi)\sigma_x$. The total Hamiltonian is given by

$$H = -\frac{\hbar\omega_a}{2}\sigma_z + \frac{\hbar\Omega}{2}\sigma_x\left(e^{-i(\phi-\omega t)} + e^{i(\phi-\omega t)}\right). \tag{2.46}$$

Applying a unitary transformation $U(t) = exp[-i\omega t/2]$ to the Hamiltonian

$$H' = UHU^\dagger - i\hbar U\dot{U}^\dagger \tag{2.47}$$

and removing all fast oscillating terms leads to the Hamiltonian in the rotating wave approximation (RWA)

$$H = \frac{\hbar\delta\omega}{2}\sigma_z + \frac{\hbar\Omega}{2}(\sigma_+ e^{i\phi} + \sigma_- e^{-i\phi}), \tag{2.48}$$

where the detuning is defined as $\delta\omega = \omega - \omega_a$.

If a two-level atom is excited it will inevitably relax from the excited state to the ground state after some time $T_1 = 1/\Gamma_1$ (relaxation time), causing ρ_{00} to increase and ρ_{11} to decrease. The probability of the system being in an excited state decays exponentially with time as $exp(-t/T_1)$. The dephasing time $T_2 = 1/\Gamma_2$ is the time over which information of the phases are lost.

Here, relaxation rate Γ_1 and dephasing rate Γ_2 are in units of s^{-1}. The jump operators of a two-level system can therefore be written as

$$L[\rho] = \begin{pmatrix} \Gamma_1\rho_{11} & -\Gamma_2\rho_{01} \\ -\Gamma_2\rho_{10} & -\Gamma_1\rho_{11} \end{pmatrix}. \tag{2.49}$$

Finally, we have arrived to the master equation for a two-level atom interacting with a classical field (eq. 2.45) with the Hamiltonian in the rotating wave approximation (2.48) and Lindblad operator (eq. 2.49).

2.5.4 The Bloch equations

We have now seen how to obtain a master equation for a two level system interacting with a classical field. The Bloch equations, that were first developed for a spin 1/2 particle in a magnetic field [46], are a method for analysing the master equation.

Computing the evolution of the expectation values of the Pauli matrices

$$\frac{\partial\langle\sigma\rangle}{\partial t} = Tr[\sigma\dot{\rho}] = Tr\Big[-\frac{i}{\hbar}\sigma[H,\rho] + \sigma L\Big] \tag{2.50}$$

for $H = \frac{\hbar\Omega}{2}\Big(\sigma^+ e^{i\phi} + \sigma^- e^{-i\phi}\Big)$, and $L = \Gamma_1\rho_{11}\sigma_z - \Gamma_2\rho_{01}\sigma^- - \Gamma_2\rho_{10}\sigma^+$ leads to the equations of the form

$$\begin{aligned}
\frac{\partial\langle\sigma_x\rangle}{\partial t} &= -\Gamma_2(\rho_{01}+\rho_{10}) + (\rho_{00}-\rho_{11})\Omega\sin(\phi) \\
&= -\Gamma_2\langle\sigma_x\rangle - \Omega sin(\phi)\langle\sigma_z\rangle \\
\frac{\partial\langle\sigma_y\rangle}{\partial t} &= -i\Gamma_2(\rho_{01}-\rho_{10}) - (\rho_{00}-\rho_{11})\Omega\cos(\phi) \\
&= -\Gamma_2\langle\sigma_y\rangle - \Omega\cos(\phi)\langle\sigma_z\rangle \\
\frac{\partial\langle\sigma_z\rangle}{\partial t} &= -(\rho_{01}+\rho_{10})\Omega\sin(\phi) + i(\rho_{01}-\rho_{10})\Omega\cos(\phi) + 2\Gamma_1\rho_{11} \\
&= \Omega\sin(\phi)\langle\sigma_x\rangle + \Omega\cos(\phi)\langle\sigma_y\rangle - \Gamma_1\langle\sigma_z\rangle - \Gamma_1
\end{aligned} \tag{2.51}$$

where the relation between the Pauli matrices and elements of the density matrix (see eq. 2.36) have become useful. Eqns. 2.51 are called the optical

Bloch equations and can be expressed more compactly as

$$\frac{d\vec{\sigma}}{dt} = \mathbf{B}\vec{\sigma} + \vec{b} \tag{2.52}$$

where

$$\mathbf{B} = \begin{pmatrix} -\Gamma_2 & 0 & -\Omega\sin\phi \\ 0 & -\Gamma_2 & -\Omega\cos\phi \\ \Omega\sin\phi & \Omega\cos\phi & -\Gamma_1 \end{pmatrix}, \quad \vec{b} = \begin{pmatrix} 0 \\ 0 \\ -\Gamma_1 \end{pmatrix}, \quad \vec{\sigma} = \begin{pmatrix} \langle\sigma_x\rangle \\ \langle\sigma_y\rangle \\ \langle\sigma_z\rangle \end{pmatrix}.$$

We can find the general solution by substituting the Ansatz ($\vec{\sigma} = e^{\mathbf{B}t}\vec{A}$) into the Bloch equation

$$\begin{aligned} \frac{\partial}{\partial t}(e^{\mathbf{B}t}\vec{A}) &= \mathbf{B}e^{\mathbf{B}t}\vec{A} + \vec{b} \\ \mathbf{B}e^{\mathbf{B}t}\vec{A} + e^{\mathbf{B}t}\dot{\vec{A}} &= \mathbf{B}e^{\mathbf{B}t}\vec{A} + \vec{b} \\ e^{\mathbf{B}t}\dot{\vec{A}} &= \vec{b} \end{aligned} \tag{2.53}$$

and integrating yields $\vec{A} = -\mathbf{B}^{-1}e^{-\mathbf{B}t}\vec{b} + \vec{c}$ where $\vec{c}$ is a constant of integration. Substituting $\vec{A}$ into the Ansatz gives $\vec{\sigma} = -\mathbf{B}^{-1}\vec{b} + e^{\mathbf{B}t}\vec{c}$. To find an expression for the constant of integration $\vec{c}$, we choose $t = 0$ and obtain $\vec{c} = \vec{\sigma_0} + \mathbf{B}^{-1}\vec{b}$ giving the solution

$$\vec{\sigma} = -\mathbf{B}^{-1}\vec{b} + e^{\mathbf{B}t}(\vec{\sigma_0} + \mathbf{B}^{-1}\vec{b}). \tag{2.54}$$

The vector $\vec{\sigma}$ can be represented on the Bloch sphere. States $|0\rangle$, $|1\rangle$ correspond to $\vec{\sigma} = \{0, 0, 1\}$, $\vec{\sigma} = \{0, 0, -1\}$ respectively and any maximally superposed state ($\rho_{00} = \rho_{11}$) corresponds to $\vec{\sigma} = \{\sin\phi, \cos\phi, 0\}$, where the phase ϕ controls the axis of rotation, i.e. $\phi = 0$ ($\phi = \pi/2$) causes rotations around σ_x (σ_y)-axis.

Fig. 2.11 shows the time evolution of a two-level atom, initially in its ground state $|0\rangle$, under a resonant drive with amplitude Ω and phase $\phi = 0$ resulting in the state rotating around the σ_x-axis. In Fig. 2.11(a), we see that the state is oscillating with time. These oscillations are called Rabi oscillations.

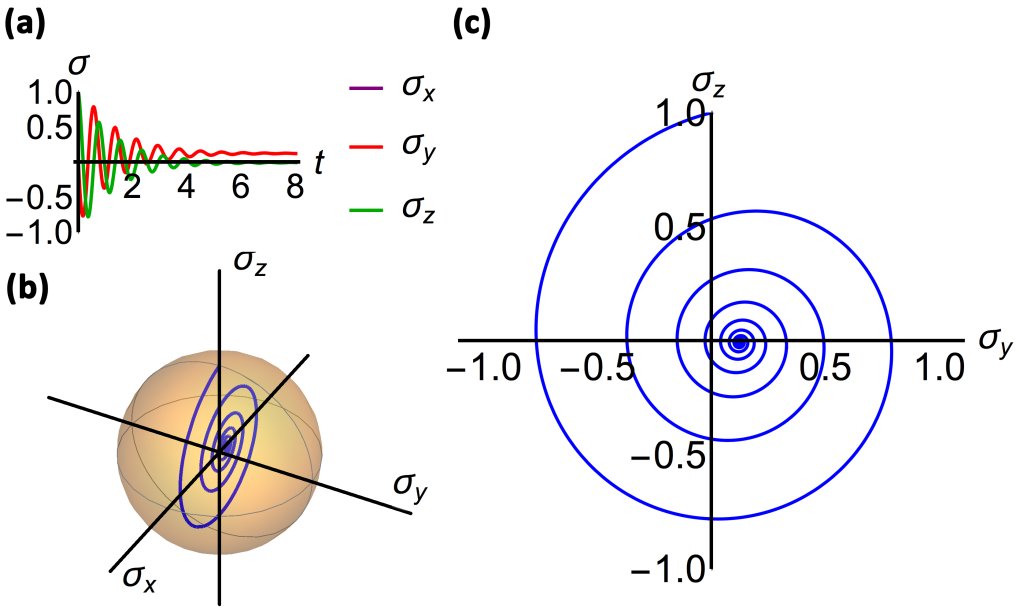

Figure 2.11: Evolution of a two-level atom ($\Gamma_2 = \Gamma_1/2 = 0.5$ arb. u.), initially in its ground state $\vec{\sigma_0} = \{0, 0, 1\}$, under a resonant drive with amplitude $\Omega = 8$ arb. u. and phase $\phi = 0$. a) Rabi oscillations. $\vec{\sigma_x}$,$\vec{\sigma_y}$,$\vec{\sigma_z}$ as a function of time. b) Evolution visualised on the Bloch sphere. c) Evolution as a function of σ_z and σ_y.

2.5.5 Quantum regression theorem

With the master and Bloch equations we can calculate single time-dependent expectation values. However, to obtain products of operators evaluated at two different times a solution of the density matrix is generally insufficient. We are particularly interested in first- and second-order correlation functions since they are needed to calculate the spectrum of the field and give insight into photon statistics respectively. In the Markovian approximation, the quantum regression theorem, attributed to Lax [47, 48], allows to determine the two-time correlation function from a single-time correlation function. In other words, it can be shown that the Bloch equations, i.e. the equations of motion for expectation values of system operators (one-time averages), are also the equations of motion for correlation functions (two-time averages). The quantum regression theorem states, that if expectation values of the column vector of operators

$\langle\hat{\mathbf{A}}\rangle$ obey a set of linear equations coupled through the evolution matrix $\mathbf{M}$

$$\langle\dot{\hat{\mathbf{A}}}\rangle = \mathbf{M}\langle\hat{\mathbf{A}}\rangle, \tag{2.55}$$

then, it can be shown for $\tau \geq 0$

$$\begin{aligned}
\frac{d}{d\tau}\langle\hat{O_1}(t)\hat{\mathbf{A}}(t+\tau)\rangle &= \mathbf{M}\langle\hat{O_1}(t)\hat{\mathbf{A}}(t+\tau)\rangle, \\
\frac{d}{d\tau}\langle\hat{\mathbf{A}}(t+\tau)\hat{O_2}(t)\rangle &= \mathbf{M}\langle\hat{\mathbf{A}}(t+\tau)\hat{O_2}(t)\rangle, \\
\frac{d}{d\tau}\langle\hat{O_1}(t)\hat{\mathbf{A}}(t+\tau)\hat{O_2}(t)\rangle &= \mathbf{M}\langle\hat{O_1}(t)\hat{\mathbf{A}}(t+\tau)\hat{O_2}(t)\rangle,
\end{aligned} \tag{2.56}$$

where $\hat{O}(t)$ can be any system operator. A derivation of the quantum regression theorem can be found in textbooks [49, 50].

2.5.6 Emission spectra

With the quantum regression theorem in hand, and following the procedure of optical spectra calculations in textbooks [49, 50], we can now calculate the spectrum

$$S(\omega) = \frac{1}{2\pi}\int_{-\infty}^{+\infty}\langle\hat{V}^-(0)\hat{V}^+(\tau)\rangle_{ss}e^{i\omega\tau}d\tau, \tag{2.57}$$

of our specific system, a capacitatively coupled artificial two-level atom. The spectrum eventually decomposes into a coherent and incoherent part

$$S(\omega) = S_{coh}(\omega) + S_{inc}(\omega). \tag{2.58}$$

First we need to define Voltage operators $\hat{V}$. We consider a flux qubit capacitatively coupled to a one-dimensional transmission line (at $x = 0$) and its dipole interaction with the external field of incident wave $V_0(x,t) = V_0e^{(ikx-i\omega t)}$ (where ω is the frequency and k is the wavenumber). The artificial atom scatters waves in both directions $V_{sc}(x,t) = V_{sc}e^{(ik|x|-i\omega t)}$ and the net wave in the transmission line $V(x,t) = (V_0e^{ikx} + V_{sc}e^{ik|x|})e^{-i\omega t}$ satisfies the one-

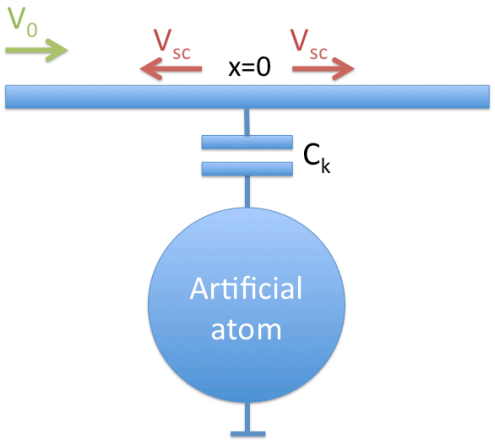

Figure 2.12: Schematic of an artificial atom coupled through a capacitance C_k to a 1-D transmission line. The incident wave indicated by the green arrow is scattered in both directions (red arrows).

dimensional wave equation

$$\frac{\partial^2 V}{\partial x^2} - \frac{1}{v^2}\frac{\partial^2 V}{\partial t^2} = l\delta(x)\frac{\partial^2 \langle Q\rangle}{\partial t^2} \tag{2.59}$$

where $v = 1/\sqrt{lc}$ is the wave phase velocity with inductance l and capacitance c per unit length. Note the resemblance of eq. 2.59 to the wave equation introduced in sec. 2.5.1. The only difference is the term on the right hand side of eq. 2.59, that appears due to the induction of current oscillating in the loop under the external drive. Integrating both sides with respect to x

$$\begin{aligned} \frac{\partial V}{\partial x} &= l\delta(x)\frac{\partial^2 \langle Q\rangle}{\partial t^2} \\ 2ik\frac{V_{sc}}{2} &= -l\omega^2 q_p \langle \sigma^- \rangle \end{aligned} \tag{2.60}$$

where q_p is the matrix transition element due to induced charge (playing the role of atomic polarisation), substituting $l = Z_0 k/\omega$ where Z_0 is the impedance of the transmission line (here 50Ω), and assuming that the relaxation of the two-level atom, $\Gamma_1 = \omega Z_0 q_p^2/\hbar$, is solely caused by the quantum noise of the transmission line as derived in sec. 2.5.7, we rearrange eq. 2.60 to obtain

$$V_{sc}^{\pm}(x,t) = i\frac{\hbar\Gamma_1}{q_p}\langle \sigma^{\mp}\rangle e^{ik|x|-i\omega t}. \tag{2.61}$$

and the operator

$$\hat{V}_{sc}^{\pm}(x,t) = i\frac{\hbar\Gamma_1}{q_p}\sigma^{\mp}e^{ik|x|-i\omega t}. \tag{2.62}$$

follows. Here, we have explicitly derived the expression for the scattered waves for the case of capacititatively coupled qubits. For qubits coupled through mutual inductance, the expression for the scattered waves has already been derived in reference [32]. Substituting eq. 2.62 into eq. 2.57 gives

$$S(\omega) = \frac{\hbar\omega Z_0\Gamma_1}{2\pi}\int_{-\infty}^{+\infty}\langle\sigma^-(0)\sigma^+(\tau)\rangle_{ss}e^{i\omega\tau}d\tau, \tag{2.63}$$

where $\langle\sigma^+(0)\sigma^-(\tau)\rangle_{ss} = \lim_{t\to\infty}\langle\sigma^+(t)\sigma^-(t+\tau)\rangle$ and the subscript (ss) of the correlator denotes the stationary solution. From the solutions of the Bloch equations (eq. 2.52), we see that the atom with initial state $\vec{\sigma_0} = \{0,0,1\}$ decays into the steady state

$$\begin{aligned}\langle\sigma^{\mp}\rangle_{ss} &= \pm\frac{ie^{\mp i\phi}}{2}\frac{\Gamma_1\Gamma_2\Omega}{\Gamma_1\Gamma_2^2+\Gamma_2\Omega^2},\\ \langle\sigma_z\rangle_{ss} &= -\frac{\Gamma_1\Gamma_2}{\Gamma_1\Gamma_2+\Omega^2}.\end{aligned} \tag{2.64}$$

Fluctuations away from this steady state are described by the operators

$$\begin{aligned}\Delta\sigma^{\mp} &= \sigma^{\mp} - \langle\sigma^{\mp}\rangle_{ss},\\ \Delta\sigma_z &= \sigma_z - \langle\sigma_z\rangle_{ss},\end{aligned} \tag{2.65}$$

and by introducing these fluctuations in operators $\sigma^{\pm}$, we expand Eq. 2.63 to

$$S(\omega) = \frac{\hbar\omega Z_0\Gamma_1}{2\pi}\int_{-\infty}^{+\infty}(\langle\sigma^+\rangle_{ss}\langle\sigma^-\rangle_{ss} + \langle\Delta\sigma^+(0)\Delta\sigma^-(\tau)\rangle_{ss})e^{i\omega\tau}d\tau, \tag{2.66}$$

where the first term describes the coherent, and the second term the incoherent part of the spectrum. Using the steady state solutions to the Bloch equations

(eq. 2.64) it is straightforward to calculate the coherent spectrum

$$\begin{aligned} S_{coh}(\omega) &= \frac{\hbar\omega Z_0\Gamma_1}{2\pi}\int_{-\infty}^{+\infty}\langle\sigma^+\rangle_{ss}\langle\sigma^-\rangle_{ss}e^{i\omega\tau}d\tau \\ &= \frac{\hbar\omega Z_0\Gamma_1}{4}\left(\frac{\Gamma_1\Gamma_2\Omega}{\Gamma_1\Gamma_2^2+\Gamma_2\Omega^2}\right)^2\delta(\omega-\omega_a). \end{aligned} \tag{2.67}$$

To calculate the incoherent part of the spectrum

$$S_{inc}(\omega) = \frac{\hbar\omega Z_0\Gamma_1}{2\pi}\int_{-\infty}^{+\infty}\langle\Delta\sigma^+(0)\Delta\sigma^-(t)\rangle_{ss}e^{i\omega t}dt, \tag{2.68}$$

we need to solve for $\langle\Delta\sigma^+(0)\Delta\sigma^-(t)\rangle_{ss}$ using the Bloch equations and the quantum regression theorem. We may start by deriving the set of linear equations

$$\langle\dot{\vec{s}}\rangle = \mathbf{M}\langle\vec{s}\rangle + \vec{m} \tag{2.69}$$

from the master equation as we did in sec. 2.5.4 or find a matrix to the previously derived Bloch equations (2.52) that converts to the frame where the vector of operators is $\vec{s} = \{\sigma^-, \sigma^+, \sigma_z\}$, such that

$$\mathbf{M} = \begin{pmatrix} -\Gamma_2 & 0 & \frac{\Omega}{2}ie^{i\phi} \\ 0 & -\Gamma_2 & -\frac{\Omega}{2}ie^{-i\phi} \\ i\Omega e^{i\phi} & -i\Omega e^{-i\phi} & -\Gamma_1 \end{pmatrix}, \quad \vec{m} = \begin{pmatrix} 0 \\ 0 \\ \Gamma_1 \end{pmatrix}.$$

Since, we are interested in the fluctuations away from the steady state, we replace the vector of operators in eq. 2.69

$$\langle\Delta\dot{\vec{s}}\rangle = \mathbf{M}\langle\Delta\vec{s}\rangle, \tag{2.70}$$

and according to the quantum regression theorem

$$\frac{d}{d\tau}\langle\Delta\sigma^+(0)\Delta\vec{s}(\tau)\rangle_{ss} = \mathbf{M}\langle\Delta\sigma^+(0)\Delta\vec{s}(\tau)\rangle_{ss}. \tag{2.71}$$

The initial conditions ($\tau = 0$) are given by

$$\begin{aligned}\begin{pmatrix} \langle \Delta\sigma^+\Delta\sigma^-\rangle_{ss} \\ \langle \Delta\sigma^+\Delta\sigma^+\rangle_{ss} \\ \langle \Delta\sigma^+\Delta\sigma_z\rangle_{ss} \end{pmatrix} &= \begin{pmatrix} (\sigma^+ - \langle\sigma^+\rangle_{ss})(\sigma^- - \langle\sigma^-\rangle_{ss}) \\ (\sigma^+ - \langle\sigma^+\rangle_{ss})(\sigma^+ - \langle\sigma^+\rangle_{ss}) \\ (\sigma^+ - \langle\sigma^+\rangle_{ss})(\sigma^z - \langle\sigma^z\rangle_{ss}) \end{pmatrix} \\ &= \begin{pmatrix} \frac{1}{2}(1 + \langle\sigma_z\rangle) - \langle\sigma^+\rangle_{ss}\langle\sigma^-\rangle_{ss} \\ -\langle\sigma^+\rangle^2_{ss} \\ -\langle\sigma^+\rangle_{ss}(1 + \langle\sigma_z\rangle_{ss}) \end{pmatrix}\end{aligned} \tag{2.72}$$

since $\sigma^+\sigma^- = \frac{1}{2}(1+\sigma_z)$, and $\sigma^+\sigma_z = -\sigma^+$. The correlation we'd like to solve is the first component of the vector $\langle \Delta\sigma^+(0)\Delta s(\tau)\rangle_{ss}$. Substituting the solutions of the one-time averages (eq. 2.64), we obtain

$$\langle \Delta\sigma^+\Delta s\rangle_{ss} = \frac{1}{2}\frac{Y^2}{(1+Y^2)^2}\begin{pmatrix} 1 + Y^2 + \frac{1}{2}(\frac{e^{i\phi}\Omega Y}{\Gamma_2})^2 \\ \frac{1}{2}(\frac{e^{i\phi}\Omega Y}{\Gamma_2})^2 \\ \frac{ie^{i\phi}\Omega Y^2}{\Gamma_2} \end{pmatrix}, \tag{2.73}$$

where $Y = \Omega/\sqrt{\Gamma_1\Gamma_2}$ and eq. 2.71 can be solved

$$\langle \Delta\sigma^+(0)\Delta s(\tau)\rangle_{ss} = \vec{V^{-1}}\exp(\Lambda t)\mathbf{V}\langle \Delta\sigma^+\Delta s\rangle_{ss} \tag{2.74}$$

where $\Lambda = \mathbf{VMV^{-1}}$ is a diagonal matrix containing the eigenvalues of $\mathbf{M}$, and the matrix $\mathbf{V}$ is formed from the eigenvectors of $\mathbf{M}$.

The shape of the incoherent spectrum (eq. 2.68) behaves drastically different depending on the strength of the drive and it is therefore usually solved for either the weak or strong regime. In the strong driving limit ($\Omega >> \Gamma_1$), the spectrum consists of three Lorentzian components,

$$S_{inc}(\omega) \approx \frac{1}{2\pi}\frac{\hbar\omega\Gamma_1}{8}\left(\frac{\gamma_s}{(\delta\omega+\Omega)^2+\gamma_s^2} + \frac{2\gamma_c}{\delta\omega^2+\gamma_c^2} + \frac{\gamma_s}{(\delta\omega-\Omega)^2+\gamma_s^2}\right) \tag{2.75}$$

where $\gamma_c = \Gamma_2$ and $\gamma_s = (\Gamma_1 + \Gamma_2)/2$ [32]. In literature it is often referred to as the resonance fluorescence or Mollow triplet, named after B. R. Mollow

who first calculated the power spectrum of light scattered by two level systems in 1969 [51]. In 1975, it was experimentally observed for the first time in an atomic beam of sodium [52] and more recently in artificial atoms [53, 32]. Eq 2.75 is the spectral density in one of the two directions (see Fig. 2.12) under strong drive and was published in reference [32].

2.5.7 Relaxation

Relaxation is a process which results in the de-excitation of the artificial atom. Fluctuations in some environmental parameter M (such as the flux Φ or voltage V), can be treated as a perturbation to the qubit Hamiltonian. The noise that leads to relaxation occurs at the qubit frequency ω_q. To find the relaxation rate, we take the two-level atom in its excited state and look at the decay into the ground state. The derivation of the relaxation rate below is based on [54].

Relaxation can be induced by a number of noise processes, including flux fluctuations, quasiparticle tunnelling, and dipolar radiation. However, for the artificial atom where the environment is usually carefully impedance matched (usually to 50Ω) the most dominant noise process is due to voltage noise. We may write the perturbation U due to voltage noise $V(t)$ as

$$U = q_p V(t)\sigma_x, \tag{2.76}$$

where q_p is the dipole moment that couples the field amplitude $V(t)$ and the driving amplitude Ω according to $\hbar\Omega = q_p V$. Strictly speaking $V(t)$ is a quantum operator, however, here for simplicity, we may treat it as a classical variable. We express the state of our two-level artificial atom as

$$|\psi(t)\rangle = \begin{pmatrix} \alpha_0(t) \\ \alpha_1(t) \end{pmatrix}. \tag{2.77}$$

First-oder time-dependent perturbation theory in the interaction picture gives

$$|\psi_I(t)\rangle = |\psi(0)\rangle - \frac{i}{\hbar}\int_0^t V(\tau)\,|\psi(0)\rangle\,d\tau. \tag{2.78}$$

Suppose the two-level atom is prepared in its excited state, then the amplitude to find it in the ground state at time t is

$$\begin{aligned}\alpha_0 &\approx -\frac{iq_p}{\hbar}\int_0^t \langle 0|\, q_p V(\tau)\sigma_x\,|1\rangle\, d\tau \\ &\approx -\frac{iq_p}{\hbar}\int_0^t V(\tau)e^{-\omega_{10}t}d\tau.\end{aligned} \tag{2.79}$$

where we have used the fact that the wavefunction of state $|1\rangle$ evolves with phase $e^{-i\omega_{10}t}$. Then the probability to find the two-level atom in the ground state is

$$p_0(t) \equiv |\alpha_0|^2 = \frac{q_p^2}{\hbar^2}\int_0^t\int_0^t e^{-i\omega_{10}(\tau_1\tau_2)}V(\tau_1)V(\tau_2)d\tau_1 d\tau_2 \tag{2.80}$$

and since we only need to consider the average time evolution of the system, we find

$$\bar{p}_0(t) \approx \frac{q_p^2}{\hbar^2}\int_0^t\int_0^t e^{-i\omega_{10}}\langle V(\tau_1)V(\tau_2)\rangle d\tau_1 d\tau_2. \tag{2.81}$$

Changing variables in the integrals, $\tau = \tau_1 - \tau_2$ and $T = (\tau_1 + \tau_2)/2$, yields

$$\bar{p}_0(t) \approx \frac{q_p^2}{\hbar^2}\int_0^t\int_{-B(T)}^{B(T)}\langle V(T-\tau/2)V(T+\tau/2)\rangle e^{-i\omega_{10}\tau}d\tau dT \tag{2.82}$$

where

$$\begin{aligned}B(T) &= T \text{ if } T < t/2 \\ &= t - T \text{ if } T > t/2.\end{aligned} \tag{2.83}$$

Assuming that the noise correlation function is time translation invariant and has a finite but small autocorrelation time τ_f, we can set the integration bound $B(T)$ to infinity giving

$$\bar{p}_0(t) \approx \frac{q_p^2}{\hbar^2}\int_0^t\int_{-B(T)}^{B(T)}\langle V(0)V(\tau)\rangle e^{-i\omega_{10}\tau}d\tau dT. \tag{2.84}$$

Introducing the zero-temperature voltage spectral density

$$S_V(\omega) = \int_{-\infty}^{+\infty} e^{i\omega\tau}\langle V(t)V(0)\rangle d\tau, \tag{2.85}$$

we find the probability to be in the ground state increasing linearly with time,

$$\bar{p}_0(t) \approx \frac{q_p^2}{\hbar^2} S_V(\omega_{10})t. \tag{2.86}$$

The time derivative of the probability gives the transition rate

$$\Gamma_1 = \frac{q_p^2}{\hbar^2} S_V(\omega_{10}). \tag{2.87}$$

It is known that the voltage quantum noise from the effective impedance Z is

$$S_V(\omega) = 2\hbar\omega Z = \hbar\omega Z_0, \tag{2.88}$$

where Z_0 is the characteristic impedance of the transmission line (usually matched to 50Ω) [54], and the relaxation rate is thus given by

$$\Gamma_1 = \frac{q_p^2 \omega_{10} Z_0}{\hbar}. \tag{2.89}$$

2.5.8 Dephasing

In the Bloch sphere visualisation, dephasing or decoherence corresponds to the length of the Bloch vector shortening in the longitude direction, i.e. on the equatorial plane, and can therefore also be interpreted as the decay of off-diagonal density matrix elements. The off-diagonal elements of a density matrix must obey $|\rho_{01}|^2 \leq \rho_{00}\rho_{11}$ where equality is reached for pure states only. Relaxation causes ρ_{00} to increase, ρ_{11} to decrease, and the coherence to

decrease. We may write

$$\begin{aligned}\delta|\rho_{01}| &\leq \sqrt{\rho_{00}(\rho_{11}+\delta\rho_{11})} - \sqrt{\rho_{00}\rho_{11}} \\ &\leq \sqrt{\rho_{00}\rho_{11}}(\sqrt{1-\Gamma_1 dt}-1) \\ &\approx \sqrt{\rho_{00}\rho_{11}}(-\frac{\Gamma_1}{2}dt) \\ &\approx -|\rho_{01}|\frac{\Gamma_1}{2}dt\end{aligned} \tag{2.90}$$

where we have used $\delta\rho_{11} = -\rho_{11}\Gamma_1 dt$. This means that the decay of the off-diagonal terms cannot be slower than $\Gamma_1/2$. However, other processes also contribute to dephasing. In particular, low-frequency noise interacting with the qubit will result in fluctuations to the qubit transition frequencies. The dephasing rate therefore decomposes into two parts

$$\Gamma_2 = \Gamma_1/2 + \Gamma_\phi \tag{2.91}$$

where Γ_1 is the relaxation rate and Γ_ϕ is the pure dephasing rate [55]. Sources that may contribute to the pure dephasing rates are charge and flux fluctuations. Noise and decoherence in superconducting qubits have been studied theoretically [56, 57, 55, 58] and experimentally [59, 55, 60].

To measure relaxation and dephasing rates, several single [61] and multipulse [62, 63] techniques have been established within the field of nuclear magnetic resonance (NMR) [63] that can be used in experiments with superconducting qubits [64].

For example, to determine the relaxation rate Γ_1 in an experiment, one needs to measure population. Preparing the atom in the excited state by a π-pulse brings the pseudospin to the z-axis of the Bloch sphere. After a time delay, during which the population of the atom decays, a $\pi/2$-pulse is applied rotating the pseudospin from the z- to the y-axis. Then, the emission can be measured as function of the time delay and can be fit with an exponential decay to obtain the relaxation rate.

The dephasing rate Γ_2 is related to the linewidths of the atom. Applying

a $\pi/2$-pulse brings the pseudospin onto the y-axis of the Bloch sphere. The emission decays exponentially with time determining the dephasing rate.

The technique presented above, which allows to separately measure Γ_1 and Γ_2, has been carried out experimentally in [64].

Chapter 3

Experimental principles

3.1 Sample design considerations

Prior to fabrication the behaviour of a flux qubit is numerically simulated using Matlab to facilitate the choice of design parameters. For details of the numerical simulations refer to section 2.3.3. The inputs of the Matlab script are the charging energy E_C and the Josephson energy E_J of a single Josephson junction, the fraction α smaller the α-junction is in area overlap compared to the standard junction, and the coupling constant.

The charging energy is given by

$$E_C = \frac{(2e)^2}{C}, \tag{3.1}$$

where C is the junction capacitance and mainly depends on the geometry of the circuit. The junction can be modelled as a parallel plate capacitor with area A, separation d, and capacitance $C = \epsilon\epsilon_0 A/d$ where ϵ_0 is the permittivity of space and ϵ is the relative permittivity of the dielectric material between the plates (here $\epsilon \approx 10$ for aluminium oxide). Thus, the typical capacitance for a junction size of 100×100 nm^2 with dielectric thickness $d \approx 2$ nm is 0.5 fF. Our standard sized junction is 200×800 nm^2 resulting in a charging energy for a single junction of $E_C/\hbar \approx 19$ GHz.

The maximal Josephson energy,

$$E_J = \frac{I_c}{2\pi}\phi_0, \tag{3.2}$$

is directly proportional to the critical current, I_c, where $\phi_0 = \frac{h}{2e}$ is the flux quantum. The critical current is described by [65]

$$I_c R_n = \frac{\pi\Delta(T)}{2e}\tanh\Big(\frac{\Delta(T)}{2k_B T}\Big), \tag{3.3}$$

where R_n is the normal resistance of the Josephson junction. As the temperature goes to zero, equation 3.3 simplifies to $I_c R_n = \frac{\pi\Delta}{2e}$. Substituting this relation into equation 3.2 gives

$$E_J = \frac{R_q}{R_n}\frac{\Delta(0)}{2} \tag{3.4}$$

where $R_q = \frac{h}{4e^2} \approx 6.4$ kΩ is the quantum resistance. Since the normal resistance of the Josephson junction depends on the oxygen pressure and the oxidation time during the formation of the tunnelling barrier, the oxidation process has to be fine tuned. Figure 3.1 shows the resistance of multiple test tunnel junctions normalised to our standard area of 200×800 nm^2 that have been oxidised for 10 minutes under different oxygen pressures at room temperature. Note that the charging energy is not sensitive to small changes in the thickness of the dielectric whereas the junction resistance, and therefore the Josephson energy is.

Fig. 3.4 shows an example of a sample chip design featuring seven flux qubits coupled to the transmission line via interdigitated capacitors. Since the width of the transmission line on chip, between the bonding pads, is smaller than the wavelength, it works as a point contact and we can therefore choose its width and length arbitrarily. The only formal requirement is that the transmission line on chip should have less inductance than the transmission line off chip, i.e. $Z_L = |i\omega L| << Z_0$. From the numerical simulations, we know the

desired coupling capacitance. To translate the desired capacitance value into the geometry of the interdigitated capacitance, we follow the analytical model presented in [66]. The interdigitated capacitance depends on the dielectric permittivity of the materials, the finger length and width, the gap width between fingers and the number of fingers.

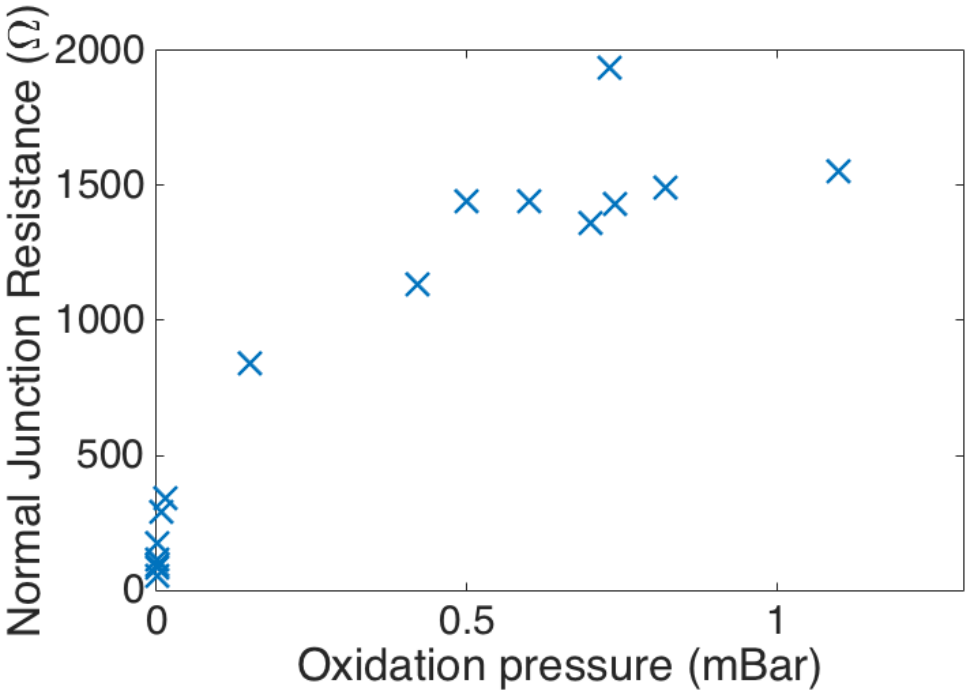

Figure 3.1: Normal resistance R_N (normalised to a junction area of 200×800 nm^2) of several $Al/Al_2O_3/Al$ Josephson junctions plotted against oxygen pressure. All test tunnel junction were oxidised for 10 minutes under different oxidation pressures at room temperature. The variation of the thickness distribution of $Al/AlOx/Al$ tunnel junctions with oxygen pressure and oxidation time has been studied in [2, 3].

3.2 Fabrication

Qubit fabrication is a key element in all experiments presented in this thesis. Reliability and reproducibility can only be achieved with a robust and carefully conducted fabrication process. All samples presented in this thesis were fabricated in the clean room facilities at Royal Holloway, University of London.

We usually start with a 2- or 3-inch wafer (undoped Silicone or Sapphire). The production of a nano-electronic device on this wafer often requires several

lithography steps. Lithography is a process that patterns part of the surface of the substrate. These patterns are subsequently used to define metal structures or etched areas to gradually build the device up.

In our devices, we use both photolithography and electron-beam lithography, where light or electrons pattern the substrate respectively. The smallest feature we can pattern with our photolithograph (limited by its wavelength and tooling factor) is ~ 4 μm and it is therefore used for patterning metal contacts for bonding, ground planes, and markers for subsequent electron-beam lithography. Photolithography acts as bridge connecting nano-sized to macro-sized circuit elements.

The nano-sized structures are patterned using electron-beam lithography. The resolution of the electron-beam lithograph is limited by its beam size and stability, as well as the mechanical stability of the sample stage. All samples presented in this thesis were fabricated using a *JEOL 6460 Scanning Electron Microscope* with a resolution of ~ 30 nm adopted for e-beam lithography and controlled by *NanoMaker*.

Below, we explain the fabrication process in more detail.

3.2.1 Photolithography

Wafer preparation

We do not grow wafers ourselves but they can be purchased. To remove organic contaminants the wafer is immersed into acetone on a hot plate at 55° for around 20 minutes. Then, the wafer is cleaned with isopropanol (IPA) and blown dry using a nitrogen gun. This is followed by etching the wafer with oxygen plasma for 2-4 minutes.

Resist spinning

First, a layer of LOR-5B lift-off resist is spun with 3000 rpm to obtain a thickness of 400 nm. The wafer is then baked at 150° for 5 minutes. The second layer of resist (S1813 photoresist) is spun with 4500 rpm to achieve a thickness of 1200 nm and baked at 90° for 5 minutes. The baking temperature

is important as it defines the development range for LOR5B. Care should be taken to spin the resist evenly since during photolithography the mask is brought into physical contact with the wafer and bumps would distort the projected pattern.

Photolithography

The wafer needs to be well aligned with the photomask. The photomask consists of many elements, each of them acting as a chip later on. The design of a single element of the photomask is shown in Figure 3.2(a). Using our in-house built photolithograph box containing a mercury lamp the wafer is exposed for 4 minutes. During this process the resolution ($\sim 4\ \mu$m) is limited by the wavelength of the light source ($\lambda \approx 436$ nm).

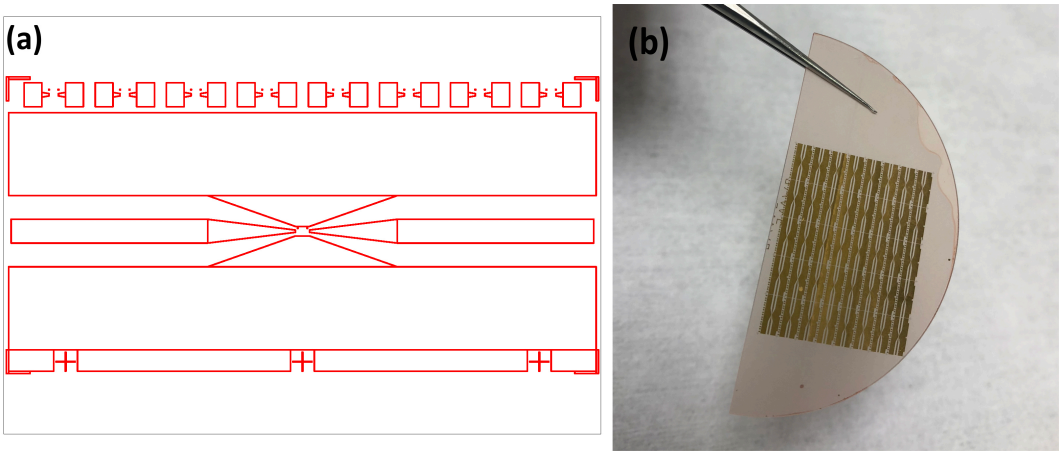

Figure 3.2: (a) Design of one building block of the photomask. On the top, there are eight fields for test structures. The field for the nano circuitry is located in the centre (main field). (b) A sapphire wafer cut into half after photolithography.

Development

The wafer is immersed into the Microposit developer MF319 for 110 seconds. The bottom of the exposed layer develops at a faster rate than the top layer creating a large undercut in the resist.

Etching and evaporation

To ensure good adhesion the wafer is etched with Oxygen plasma for 20 seconds before thermal evaporation. An adhesion layer of Ni/NiCr of 10 nm, followed

by a 80 nm layer of gold is evaporated onto the wafer.

Lift-off

To remove the bulk of the resists the wafer is immersed into Microposit 1165 remover and placed onto a hot plate at 65°. After 20 minutes the remover is replaced and the wafer is soaked for another 20 to 40 minutes to dissolve the residuals of the resist. To cease the lift-off the wafer is flushed with deionised water and dry blown using a nitrogen gun.

Figure 3.2(b) shows a sapphire wafer cut into half after photolithography.

3.2.2 Electron beam lithography

Fig. 3.3 illustrates the fabrication steps for electron-beam lithography.

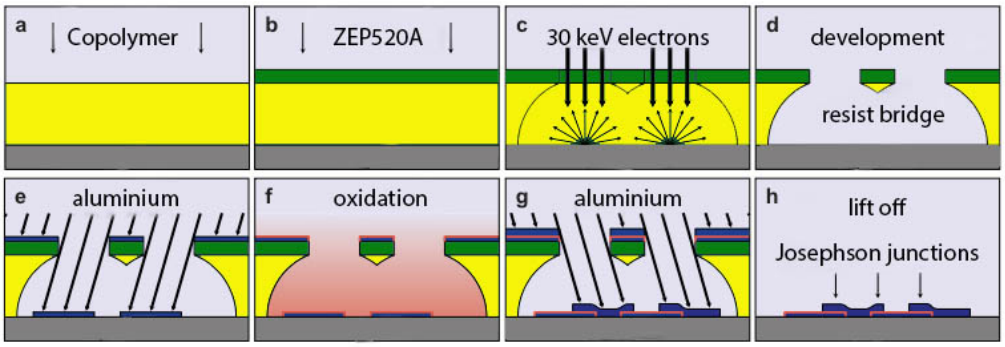

Figure 3.3: Fabrication steps for electron-beam lithography. a) Copolymer of thickness 0.7μ m is spun on the undoped silicone or sapphire substrate. b) After baking, a 60 nm layer of ZEP520A is spun on top of the first layer and baked. c) Electron beam lithography of qubits. d) Development of the exposed resist. e) Evaporation of aluminium. f) Oxidation of aluminium. g) Shadow evaporation technique [4]. h) Resist liftoff. Figure adapted from [5].

Resist Spinning

Two layers of resist are spun directly onto the wafer. The first layer is copolymer (13%) with a thickness of 700 nm. The wafer is then baked for two minutes at 160 °C on a hot plate prior to depositing a 60 nm layer of ZEP520A (1:2) directly on top of the copolymer layer. This is followed by baking both layers for another 2 minutes on the hot plate.

Chip preparation

Suitable wafers with markers are cut into chips of size 2.5×5 mm. Similar to any clean room process, it is paramount to remove contamination from the chips. This is particularly true for thin film Josephson junctions since their critical current can strongly be influenced by the surface roughness of the substrate [5]. The chips are rinsed with isopropanol (IPA) in an ultrasonic bath and are blown dry using a nitrogen gun.

Electron beam lithography

Electron beam lithography is a technique allowing to form arbitrary two-dimensional patterns down to the nanometer scale. It involves the exposure by a highly focused electron beam to dramatically modify the solubility of a resist material during subsequent development [67].

A typical Electron beam lithography (EBL) system has a filament that acts as an electron source. The electron beam is accelerated and highly focused. A pattern can be generated by blanking and deflecting the beam.

Prior to loading the sample into the *JEOL 6460 SEM Scanning Electron Microscope*, the resist on the chip is deliberately scratched directly underneath the main field in the centre of the chip and underneath each test field (see Fig. 3.2(a)). This is to facilitate focusing on the scratches.

The design of the qubit structure are loaded onto the *Nanomaker* software. An electron accelerating Voltage of 30 kV is provided. We set the working distance to 10 m and the beam current to 10 pA by adjusting the spot size of the beam.

One method to test the size of the beam is to "burn" a hole into the resist. This is done by zooming into the maximum magnification ($300000\times$), and switching into the "spot regime", where the beam is no longer scanned, for 30 seconds. We found that our beam spot size for our system on the undoped Silicone substrate is ~ 50 nm.

Another method to test the beam spot size is to perform an α-test [68]. Here α is the beam spot and one of the proximity parameters (α, β, η) for

the "fitting before measurement" procedure [69]. The pattern for the α-test consists of many isolated vertical lines with increasing width from left to right, and increasing dose from bottom to top. After exposing this test pattern for varying α, we expect the top row(s) to be underexposed and the bottom row(s) to be overexposed. However, for the correct value of α the boundary between overexposed and underexposed areas will form a straight horizontal line. We also obtain a beam spot size of $\alpha \approx 50$ nm for our system (undoped Silicone substrate) using the α-test. The beam size is the limiting size of the structures we can reliably fabricate.

We chose a base dose of 70 μCcm^{-2} derived from a dose test for our structures. In a dose test, the development time is fixed (to 30 seconds in our case), and then the test structure is exposed multiple times with varying dose. After the whole fabrication cycle, the test structures are inspected using the SEM, and the best base dose is determined.

The proximity distance determined by electrons backscattered in the substrate, β, is the limiting margin for distortions. For undoped Silicone, an accelerating Voltage of 30 keV, and our resist, β is 4.2 μm [68]. Structures that are larger than β, in our case the transmission line and contact pads, need to be proximity corrected. The dose of structures that are smaller than β still has to be fine tuned due to the nature of the two Gaussians of the beam (formed by primary and backscattered electrons). As illustrated in Fig. 3.4 finer elements of the design are given a greater dose. We assign a dose of 181% for the qubit line's containing Josephson junctions, a dose of 166% for the leads to the qubit, and a dose of 121% for the capacitors.

Before exposure, we find features on a test chip, that has been loaded together with the sample chip. We begin with low magnification and focus on the features, and then gradually increase the magnification and refocus.

Then, to check the aperture alignment we select the "OL Wobbler"-tool on the menu bar of the SEM software. If the image wobbles we adjust the X/Y direction fine adjustment knobs on the Objective aperture to minimise

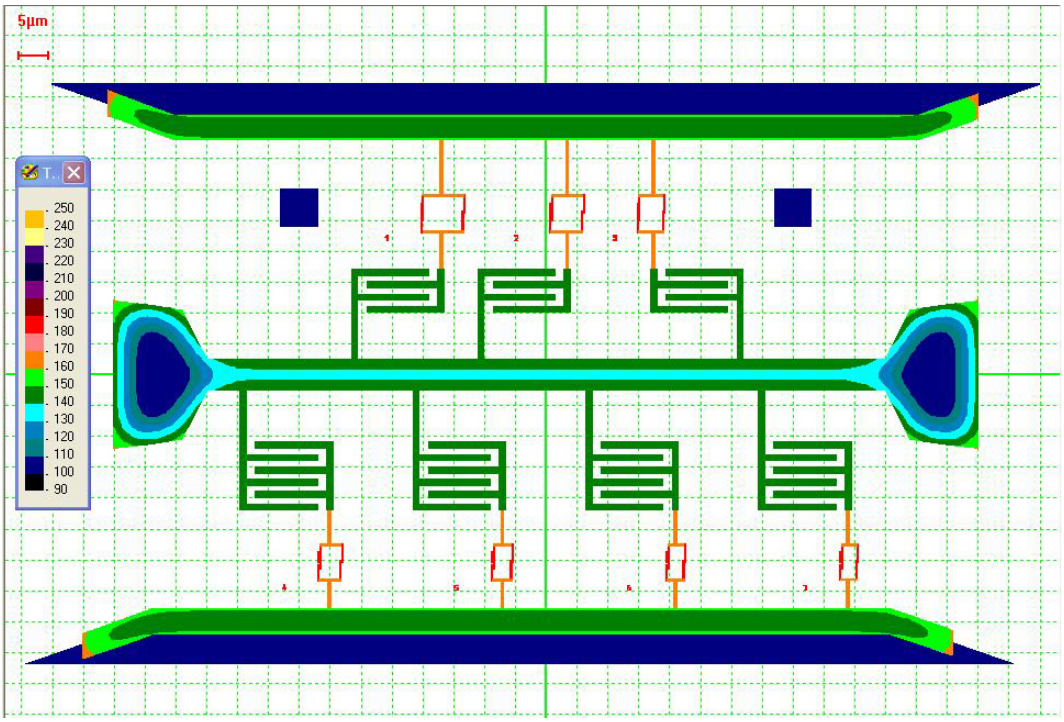

Figure 3.4: Chip design with a base dose of 70 μCcm^{-2} (dark blue). Seven qubits are capacitatively coupled to a transmission line. The transmission line and contact pads have been proximity corrected. A dose of 181 is assigned to the qubit lines containing Josephson junctions (in red). A dose of 166 is assigned to the qubit lines (in orange). A dose of 121 is assigned to the coupling capacitors (in green).

the image shift.

To correct for astigmatism we find a round feature. We focus and defocus on this object to check whether the feature goes out of focus evenly or stretches when out of focus. If there is astigmatism present we correct it by activating the "STIG"-button and adjust the X/Y knobs on the control panel to obtain the sharpest image.

Being in focus is critical during the EBL process. Thus, we fine tune the focus on the scratches on the sample chip before every exposure. Alternatively, we can use the "hole burning" method (described above) if no scratches or other features are visible for focusing. Eight test fields are exposed including Josephson junctions, test wires and a structure imitating our qubit geometry before exposing the central field with the final design geometry.

For an insulating substrate such as sapphire, we need to spin PE-

DOT:PSS [70] or evaporate a thin layer of aluminium (10 nm) prior to e-beam lithography to avoid electrostatic charging effects that can cause distortions or shifts in the exposed patterns. This PEDOT:PSS or aluminium layer ensures quick discharge of the deposited electrons during exposure. Before development, this layer of PEDOT:PSS or aluminium has to be removed again.

PEDOT:PSS is removed by immersing the chip into warm deionised water and placing it onto a heat plate at 45° for 3 minutes. While on the hot plate, we flush the chip using a pipette. Once we are convinced the PDOT is fully removed we blow dry the chip using a nitrogen gun.

The aluminium layer is removed at room temperature with photoresist MF3-19. We wash the chip with deionised water and blow dry with a nitrogen gun.

I recommend to use the layer of aluminium as a discharge layer, because PEDOT:PSS looks rather grainy when imaging.

Development

After the EBL process, the exposed lower molecular weight resist is removed chemically. The first layer is developed using P-Xylene. The development is ceased after 30 seconds by rinsing the sample in IPA. The chip is then blown dry using a nitrogen gun before the 2nd layer is developed by immersing the sample in an $IPA : H_2O$ mixture (93:7) for 10 minutes. The chip is rinsed in IPA and blown dry.

Evaporation and Oxidation

The shadow evaporation technique (Fig. 3.3) is an established process known and used for many years [4]. We use an electron beam evaporator from *Plassys*. The sample is mounted onto the sample holder. Good alignment is crucial since we evaporate at two angles. After loading the sample the loadlock chamber is vacuum pumped. *Plassys* can run fully automatically by following programmable recipes. Typical steps of such a recipe include: Pumping chamber and loadlock, evaporating a 20nm layer of high purity aluminium (purity= 99.999%) at a chosen angle (typically +12 °), dynamic or static ox-

idation (purity= 99.9999%), pumping loadlock, evaporating a 30nm layer of aluminium (purity= 99.999%) at the chosen angle (typically $-12\,^{\circ}$), and static caping.

Lift-off

The resist is dissolved by baking the sample at 55 °C in acetone for 10 minutes. Using a pipette the sample is flushed and all metal that was in direct contact with the resist is removed. Ideally, the aluminium comes off in one piece due to the large undercut and a comparably large resist thickness. The chip is then briefly immersed in IPA and blown dry using a nitrogen gun.

3.3 Room temperature characterisation

We inspect the chip using a microscope. After successful fabrication, we measure the resistance of the test structures using a probe station at room temperature. This is important because we would like to know whether we hit our desired Josephson energy or not.

We measure the resistance of the test tunnel junctions, take the average and subtract the resistance of the structure imitating our qubit structure to obtain the true resistance of the Josephson junction. We can then calculate the expected Josephson energy using Eq. 3.4. It is known that the resistance of Josephson junctions changes at cryogenic temperatures. To quantify this change, we have measured a Josephson junction at room and cryogenic temperatures and found that the Josephson junction resistance increases by $\sim 10\%$ at 15 mK. We take this change in resistance into account when estimating the Josephson energy.

Additionally we measure the resistance of the test wire and the transmission line to ensure it is not open or shortened. We also check that our main structure is not connected to the ground planes. Since our samples are sensitive to static discharge, we ground ourselves, turn on an air ioniser and place the sample chip on an anti static foam.

It is known that Josephson junctions age, their resistance increases with

time. Junction ageing is often attributed to the junction oxidising further when exposed to air, particularly around the edges of the junction. This can be prevented by storing the samples in an evacuated desiccator [71]. In addition, the AlO_x insulator layer is believed to only slowly stabilise to the stable AlO_3 by a diffusive mass transport from the sandwiched oxygen rich surface (AlO_x) to the aluminium layers [72]. Thus, if the sample has to be stored for some time, it is recommended to measure the test Josephson junctions again before loading it into the cryostat for measurement.

3.4 Wire bonding

When satisfied with the obtained Josephson energy and the quality of our sample, we take a printed circuit board (PCB) that has been screwed on a copper stand. The PCB interconnects the sample chip with the rest of the measurement circuit. We glue the sample chip into the space holder of the PCB and onto the copper stand. It is easier to bond when the sample chip is levelled with the PCB. Depending on the thickness of the PCB and sample chip, it is sometimes necessary to use a spacer to level them.

Once the glue (varnish) has dried we bond the sample with aluminium wires of thickness ~ 25 μm using the *Westbond wire bonder 7476E*. The thickness of the bonding wire determines the limiting size of the bonding pads on chip. For our bonding wire (~ 25 μm), bonding pads smaller than 100 μm would make bonding very difficult. We connect the transmission line (or resonator) with 3 bonds on each side. The ground plane of the PCB is bonded to the ground plane of the sample chip, with ~ 6 bonds along the sample chips width and ~ 15 bonds along its length as seen in Fig. 3.5(b). In addition, we connect separated segments of the ground of the PCB (Fig.3.5(a)) to avoid spurious resonances.

3.5 Measurement setup

Typical transition energies of artificial atoms are in the GHz range. This frequency range is convenient since microwave equipment is already well es-

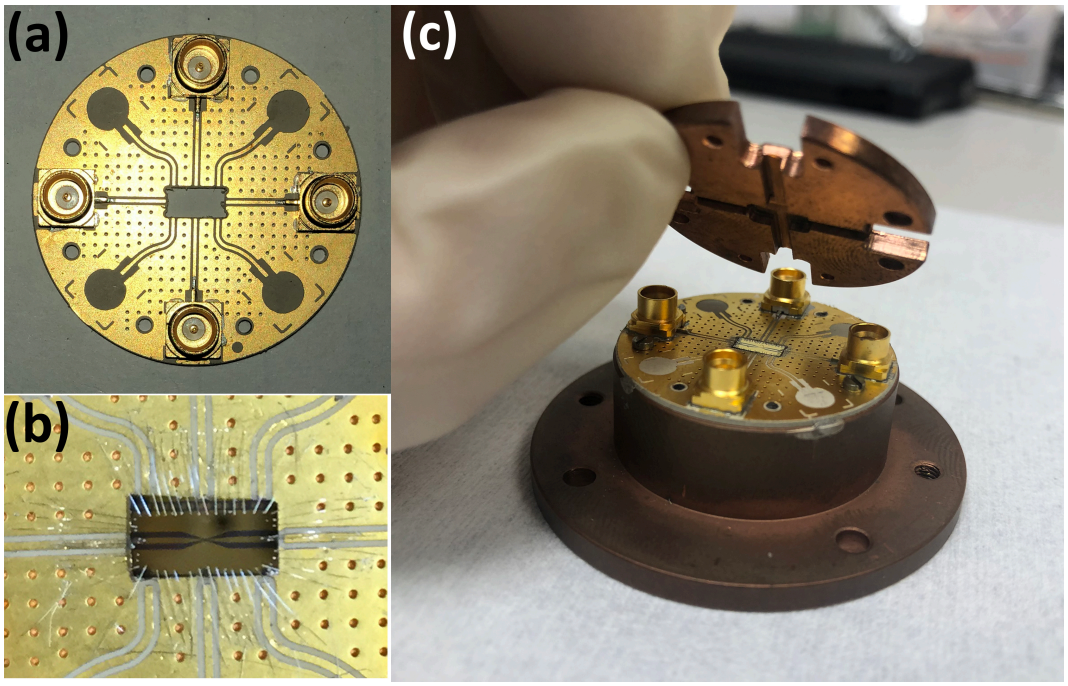

Figure 3.5: Photograph of sample holder assembly. (a) Printed Circuit Board (PCB). (b) Aluminium wire bonds connecting the sample chip with the PCB. The transmission line on chip is connected to the impedance matched line (50Ω) on the PCB with 3 bonds on each side. The ground plane of the PCB is bonded to the ground plane of the sample chip, with ~ 6 bonds along the sample chips width and ~ 15 bonds along its length. (c) PCB with bonded sample chip on copper stand. A copper anti-spacer is screwed on top of the PCB to minimise room for standing waves avoiding parasitic resonances.

tablished due its extensive use in telecommunication applications. Here, we study coherent effects on the level of a single quantum scatterer. The challenge is to control and analyse microwave signals at extremely low powers $P \sim \hbar\omega\Gamma_1 < 10^{-18}$ W.

In addition to careful microwave engineering, experiments with artificial atoms require cryogenics. 1 GHz corresponds to a temperature of 50 mK ($T \approx \frac{hf}{k_B}$). We therefore have to cool the artificial atoms below < 50 mK to suppress thermal excitations. In addition, we have to cool below the critical temperature T_c of the superconducting material we use for our nano-electronic circuits; (for aluminium $T_c \approx 1.3$K).

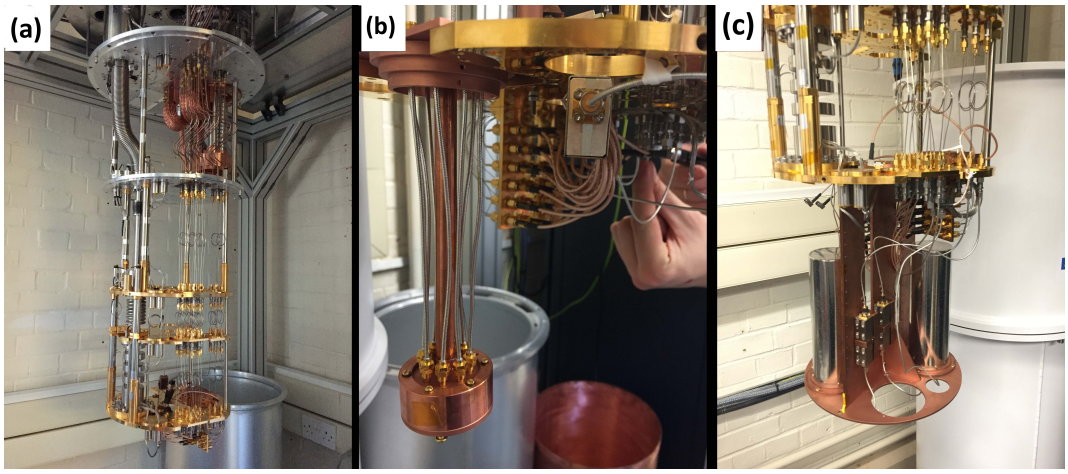

Figure 3.6: Photograph of *Blue Fors* cryostat insert layout. (a) From top to bottom: 50K flange, quasi-4K flange, still flange, cold plate, and mixing chamber flange. (b) Coil assembly for flux qubits. (c) Additional stage for flux qubit sample holders. The coil assemblies are shielded by a *Cryoperm* shield.

3.5.1 Cryogenic Environment

Experiments are performed using a *BlueFors* liquid helium free cryostat shown in Fig. 3.6 reaching a base temperature of 15mK.

There are two different types of wiring in the cryostat: RF and DC. The RF lines require a high bandwidth but carry low power leading to a different kind of noise consideration. At GHz frequencies Johnson noise generated by the thermal motion of charge carriers in the conductor, is the dominant noise source. The power spectral density can thus be estimated to be linear with temperature T and the resistance R as $S_{v^2} = 4k_BTR\Delta f$ where Δf is the bandwidth in Hertz. Since RF signals require a large bandwidth, we do not filter them but pass through attenuators to suppress noise. The DC lines can be filtered using low pass filters and thermal coax since the signal and noise do not coincide in the band.

Thermal conductivity significantly decreases at low temperatures. On the one hand, this is advantageous since it lowers the heat load on the cold stages, but on the other hand it means that good care has to be taken in thermally anchoring all components. As seen in Fig. 3.6, the lines inside the cryostat are not perfectly fitted in length but feature "springs" or "piggy tails" to allow for

thermal expansion/contraction.

We have installed sample holders, for DC-, and for RF-measurements, in the cryostat. The RF sample holder depicted in Fig. 3.5(c) is attached to the coil assembly (Fig. 3.6(b)) and then shielded using a *Cryoperm* shield (Fig 3.6(c)). Fig. 3.7 shows the drawing of the sample holder assembly. The copper stand with the PCB slides into a cylindrical compartment featuring eight through-holes for SMP microwave connectors. The blue region in Fig. 3.7 of the compartment indicates the groove into which a superconducting coil is wound. The superconducting solenoid is wound with a Cu 30Ni/NbTi wire of diameter 0.11mm. The coil consists of $\sim$ 3500 turns around the sample compartment and is used to bias the qubits. The compartment is attached to a rod that is suspended from either the mixing chamber flange or the bottommost stage of the cryostat. The whole sample holder assembly is protected from external magnetic fields by a shield purchased from *Cryoperm*.

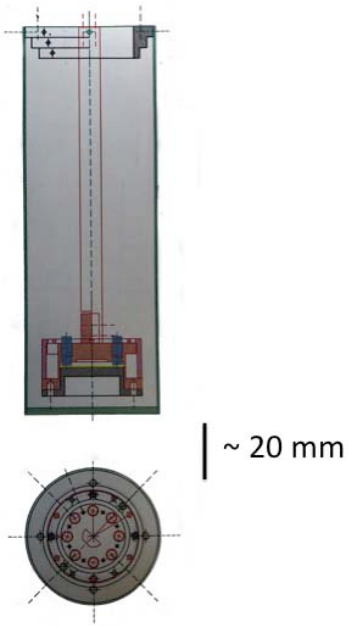

Figure 3.7: Drawing of sample holder assembly.

We connect the PCB (with the sample chip) through two SMP connectors to the input and output lines inside the cryostat. The input line inside the cryostat is attenuated by 10dB at 4K, and 30dB at 15mK and the line

itself attenuates $\sim$ 10dB. The RF output line features a $1-12$ GHz cryogenic amplifier from *Low Noise Factory* (Model LNF-LNC1_ 12A s/n 330B or LNF-LNC1_ 12A s/n 337B) with a gain of $\sim$ 35dB at 4K and one cryogenic isolator from *Quinstar Technology* at $\sim$ 15mK. The isolator allows signal to be transmitted in one direction with negligible attenuation but attenuates the signal by $\sim$ 18dB along the opposite direction. Hence, this microwave element will ensure that the noise from the amplifier does not reach the artificial atom.

3.5.2 Microwave engineering

To control the artificial atoms we need to apply classical phase coherent microwave signals. As a microwave source we either use a *Rohde & Schwarz* Vector Network Analyser (Model ZNB20, 100kHz - 20GHz) or a *Rohde & Schwarz* microwave signal generator (Model SMB 100A, 100kHz-20GHz).

For pulsed measurements, we use *Keysight's* pulse function arbitrary generator (81160A) that generates envelope pulses on two independent channels and allows to modulate the amplitude of the microwave signals with nanosecond resolution. Pulses are shaped with "choppers" that consist of two IQ modulation mixers from *Marki* (M80420LS), a *Mini-circuits* splitter (ZFRSC-42-S+), a *Mini-Circuits* low pass filter (SLP-1200+), and some attenuators. Fig. 3.8 shows a circuit schematic and photograph of a chopper. The classical coherent microwave signal is fed into one of the mixers, the envelope pulse is fed into the other, and both signals are added using the splitter (in reverse). We check the shape of pulses with *Tektronix'* digital phosphor oscilloscope (DPO 72304DX).

To tune the transition frequencies of our artificial atoms we apply an external field through a superconducting coil that is biased by the *Yokogawa* DC Voltage/Current Source (GS200) in the current source mode. Currently, we have three qubit sample cells installed in the cryostat with superconducting coils that produce ~ 0.144, ~ 1.65, and ~ 1.56 Gauss per mA allowing us to tune across many flux quanta for each qubit.

Outside the cryostat, we add another $1-15$ GHz amplifier from *Low Noise*

Factory (Model LNF-LNR1_ 15A) with a gain of 37dB into the output line.

The Vector Network Analyser (VNA), the microwave signal generator (MWG), and the pulse function arbitrary generator are synchronised to each other.

Depending on the measurement, we either read the signal with the VNA or a Spectrum Analyser (SPA) from *Anritsu* (MS2830A, 9kHz-13.5Ghz).

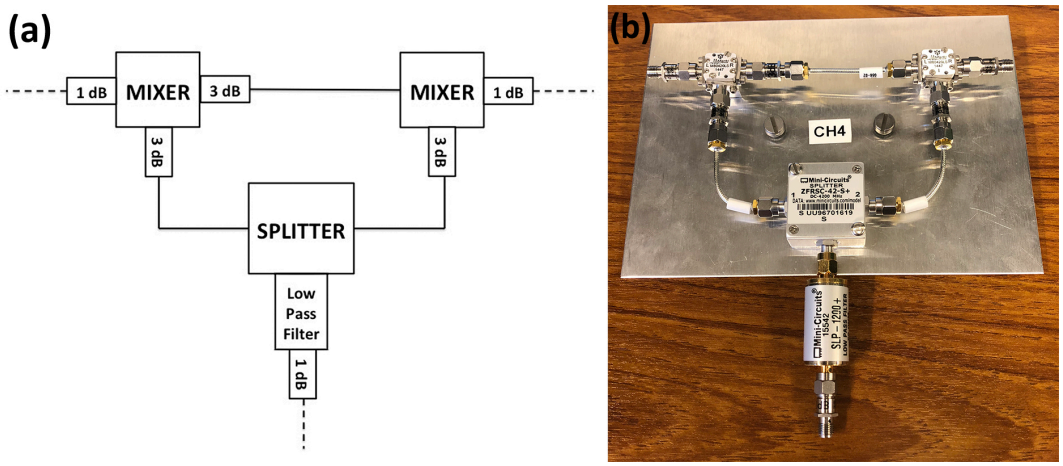

Figure 3.8: (a) Circuit schematic and (b) photograph of a chopper consisting of two mixers, one splitter, a low pass filter and attenuators.

3.6 Qubit characterisation

Once the qubits have been fabricated and cooled down to 15 mK, we start by characterising our sample before moving on to more elaborate experiments.

As an example, we present here the characterisation of the first superconducting qubit (Fig. 3.9(a)) in the UK. We fabricated six qubits in series, each of them coupled through a shared segment of the transmission line (10 squares). As seen in Table 3.1 and Fig. 3.9(b), the area of the loop and α, the area overlap of the α-junction, is systematically decreased from qubit to qubit.

3.6.1 Spectroscopy

The transition frequencies of the artificial atom(s) coupled to open space (or transmission line) are revealed through transmission spectroscopy. Fig. 3.10

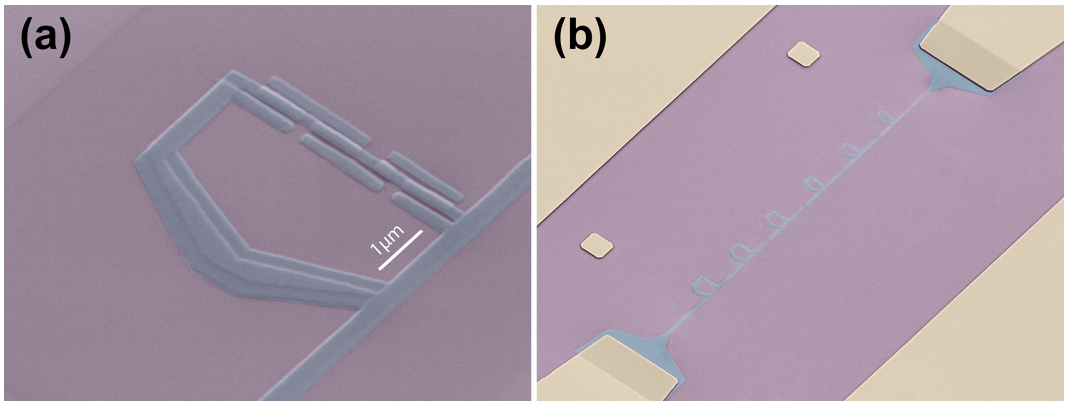

Figure 3.9: The first UK qubits. (a) False-coloured scanning-electron micrograph (SEM) of a flux qubit coupled to a 1D transmission line. The flux qubit consists of a macroscopic superconducting loop interrupted by four Josephson junctions that are inductively coupled to the line. (b) Six flux qubits with varying loop area inductively coupled to the transmission line. Colour-code: Yellow, blue and violet correspond to gold, aluminium and the Si substrate respectively

Qubit ID	Loop Area (μm^2)	α	Area ratio
1	33.06	0.48	0.707
2	27.65	0.45	0.845
3	23.37	0.42	1.000
4	19.48	0.39	1.199
5	16.57	0.36	1.410
6	14.15	0.33	1.652

Table 3.1: Design parameters of six flux qubits inductively coupled to the transmission line. The area of the loop is decreased from qubit to qubit. α quantifies how much the area overlap smaller the α-junction is compared to the standard Josephson junctions.

shows the experimental setup. A Vector Network Analyser provides the microwave signal that is attenuated by 60dB at room temperature, 10dB at 4K, and 30dB at 15mK before reaching the transmission line on chip. The artificial atom is either coupled inductively or capacitatively to the transmission line and is biased through an external field provided by a superconducting coil. The output line features an isolator, a cryogenic amplifier at 4K, and an additional amplifier at room temperature.

We sweep the frequency of the incident microwave in a wide range and step in external field while we monitor the transmission using a VNA. Fig. 3.11

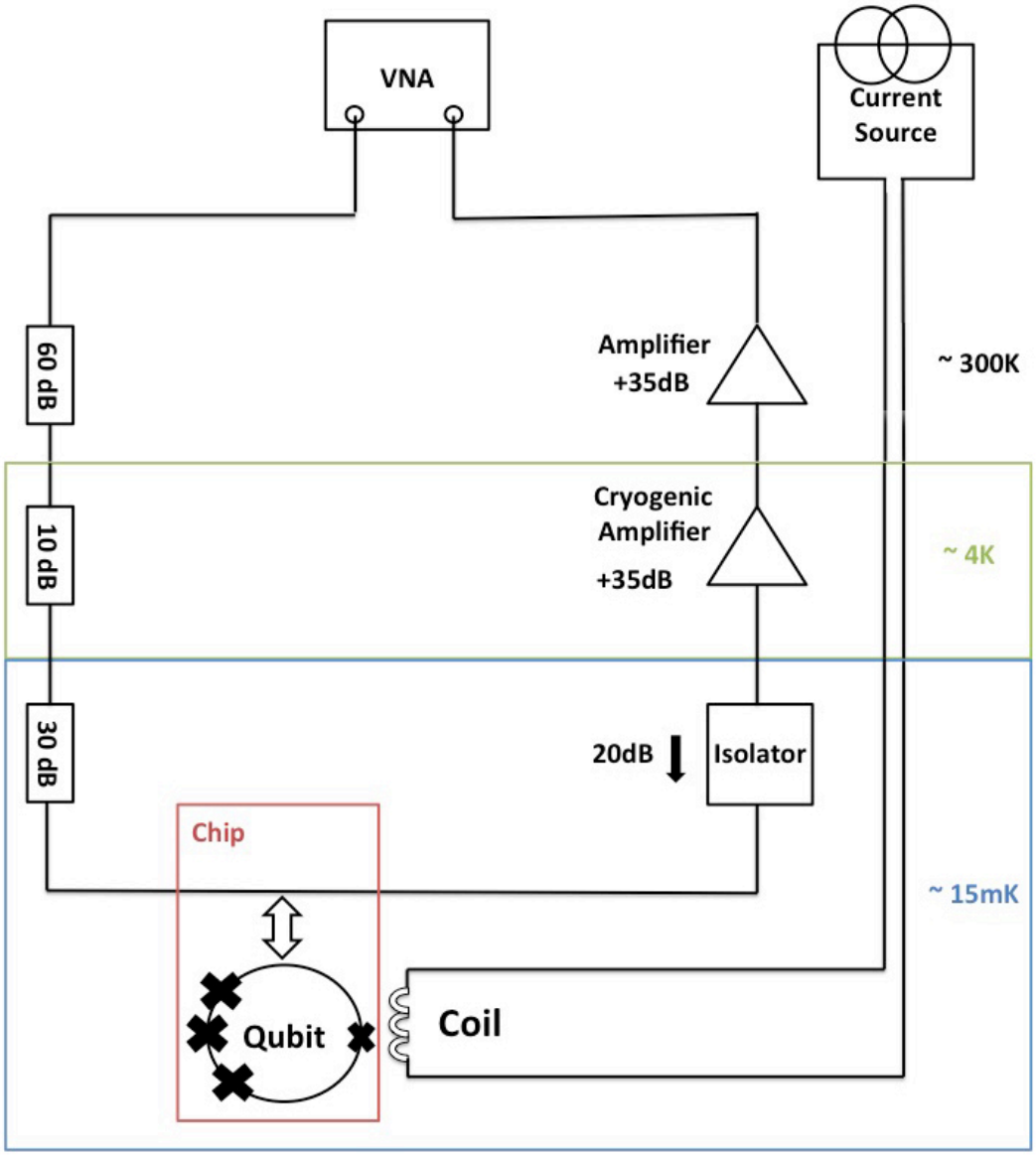

Figure 3.10: Experimental setup for tranmission spectroscopy. The input line is attenuated using 60dB at room temperature, 10dB at 4K and 30dB at 15mK. The flux qubit is coupled through mutual inductance to the transmission line (on chip). The output line includes an isolator giving $\sim$ 20dB attenuation to prevent noise reaching the sample from the output line. The signal is then amplified at 4K and at room temperature. The external flux applied to the artificial atom acts as control.

shows the transmission spectroscopy of one of the qubits.

In chapter 2, we have derived that the capacitatively coupled artificial atom scatters waves backward and forward (see Eq. 6.3). Similarly, we can

derive an expression for inductively coupled qubits

$$I_{sc}(x,t) = i\frac{\hbar\Gamma_1}{\phi_p}\langle\sigma^-\rangle\, e^{ik|x|-i\omega t}, \tag{3.5}$$

where $\phi_p = MI_p$ is the dipole moment matrix element and is proportional to the loop-line mutual inductance M (due to the shared segment of the transmission line) and the persistent current I_p in the superconducting loop.

Defining reflection and transmission coefficients, r and t, as $I_{sc} = -rI_0$ and $I_0 + I_{sc} = tI_0$, and therefore satisfying $t + r = 1$, we find an expression from Eq. 3.5 for the reflection coefficient

$$r = r_0\frac{1 + i\delta\omega/\Gamma_2}{1 + (\delta\omega/\Gamma_2)^2 + \Omega^2/\Gamma_1\Gamma_2}, \tag{3.6}$$

where the maximal reflection amplitude $r_0 = \eta\Gamma_1/2\Gamma_2$ at $\delta\omega = 0$ and η is a dimensionless coupling efficiency to the line field, including nonradiative relaxation. We have found $\langle\sigma^-\rangle$ from solving the master equation $\dot{\rho} = -\frac{i}{\hbar}[H,\rho] + \hat{L}[\rho]$ for $\dot{\rho} = 0$ with $H = -(\hbar\delta\omega\sigma_z + \hbar\Omega\sigma_x)/2$.

At the transition frequency of the artificial atom, we detect a sharp dip in the transmission because the wave scattered forward by the artificial atom is interfering destructively with the incident wave ($I_{sc} = -I_0$ or $V_{sc} = -V_0$). Out of the six qubits, three are revealed through transmission spectroscopy with the remaining three being out of our measurement range. Note that the wide range of energies has been chosen on purpose for optimisation of our fabrication parameters. We observe the systematic change of the energies according to our expectations, indicating a 100% fabrication yield.

We determine the periodicity (in flux or current), which depends on the area of the loop, of the three flux qubits. Comparing the ratio of the loop areas (Table 3.1) with the ratio of the measured periods (Table 3.2), we can thus identify which three out of the six qubits we are measuring.

The persistent current I_p is proportional to the slope of the hyperbolic

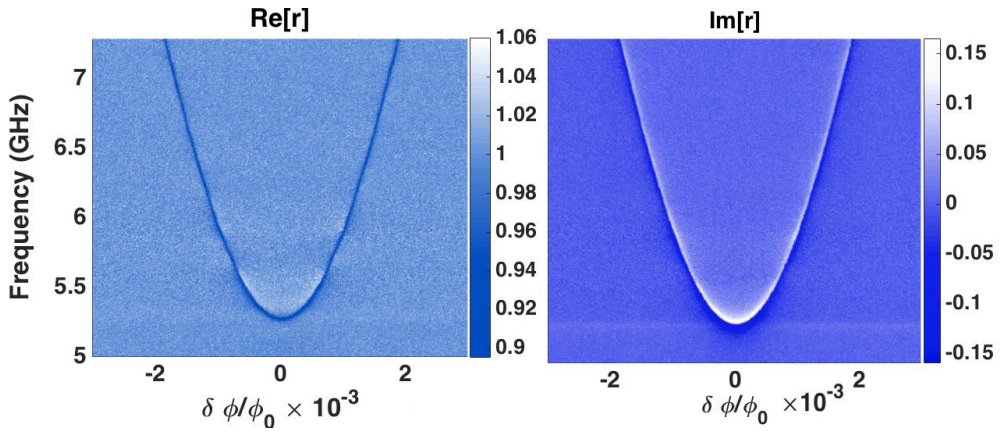

Figure 3.11: Transmission spectroscopy of the flux qubit (Qubit ID 4). Shown is the real and imaginary part of the reflection coefficient r as a function of flux bias $\delta\phi/\phi_0$ and incident microwave frequency $\omega/2\pi$ where $\delta\phi = \phi_{ext} - \phi_0/2$.

resonance curve (Fig. 3.11)

$$I_p = \frac{1}{2}\frac{\hbar\partial(\epsilon)}{\partial(\delta\phi)} = \frac{e\partial(f)}{\partial(I)}I_0, \tag{3.7}$$

where we have substituted $\delta\phi = \phi_0(I/I_0)$ with the flux quantum $\phi_0 = h/(2e)$ and where I_0 is the period in current.

At the degeneracy point ($\delta\phi/\phi_0 = 0$ where $\delta\phi = \phi_{ext} - \phi_0/2$), the power extinction $|t|^2$ reaches its maximal value of $\geq 73\%$ for all three qubits, which suggests that they are well isolated from other degrees of freedom in the surrounding solid state environment and behave as an isolated atom in open space, coupled only to the electromagnetic fields in the transmission line.

Table 3.2 summarises the qubit characterisation through transmission spectroscopy.

3.6.2 Smith chart representation of the microwave transmission

The Smith chart [73] is named after its inventor, Phillip H. Smith, and used in microwave engineering to assist to separate external from internal losses and its elliptical (or circular) shape indicates non-linearity (or linearity).

The measurement set-up for the Smith charts is the same as for spec-

Qubit ID	Frequency, GHz	Period, mA	Period ratio	I_p, nA	$\|t\|^2$
3	2.450	6.147	1.000	465	73%
4	5.216	7.370	1.199	416	88%
5	14.678	8.669	1.410	273	99%

Table 3.2: Qubit characterisation through transmission spectroscopy. From first to last column: Qubit identification, frequency $\omega/2\pi$ at the degeneracy point in GHz, period I_0 in mA, ratio of periods of neighbouring qubits, persistent current I_p in nA and power extinction $|t|^2$ at the degeneracy point.

troscopy since in both cases we measure direct transmission (see Fig. 3.10). We plot real and imaginary parts of the transmission coefficient, $t = 1 - r$ (see Eq.6.4), at the degeneracy point ($\phi_{ext} = n/2$ with integer n) as a function of frequency detuning $\delta\omega/2\pi$ from the resonance at $\omega_0/2\pi$. From fitting Eq. 6.4, we can estimate relaxation and dephasing rates, Γ_1 and Γ_2 respectively. Assuming $\Gamma_2 = \Gamma_1/2$, we find $\Gamma_1 \approx 15$ MHz for qubit ID's 3 and 4, and $\Gamma_1 \approx 28$ MHz for qubit ID 5. As seen in Fig. 3.12, in the vicinity of the resonance $Re[r]$ is positive and reaches its maximum, whereas $Im[t]$ changes its sign from positive to negative. With increasing incident power W_0, the peak in the reflection curve decreases (Fig. 3.12(b)), and the shape of the curve in the Smith chart representation changes from a circle to an ellipse (Fig. 3.12(a)). Fig. 3.12(b) shows that the two-level atom saturates at larger powers and can have high power extinction only for the weak driving regime ($\Omega^2/(\Gamma_1\Gamma_2) << 1$).

3.6.3 Rabi Oscillations

So far we have established through spectroscopy that our qubits are functional, but to study their dynamical behaviour we need to perform measurements in the time domain.

The measurement circuit for Rabi oscillations is depicted in Fig. 3.15.

We drive the artificial atom at its transition frequency ω_a with a microwave pulse (denoted as P) for a time Δt_P. The incident microwave pulse P is shaped by a chopper (Fig. 3.8) connected to a continuous microwave source provided by a Vector Network Analyser (VNA) and a pulse envelope provided by *Keysight's* pulse function arbitrary generator (PFAG). The microwave pulse

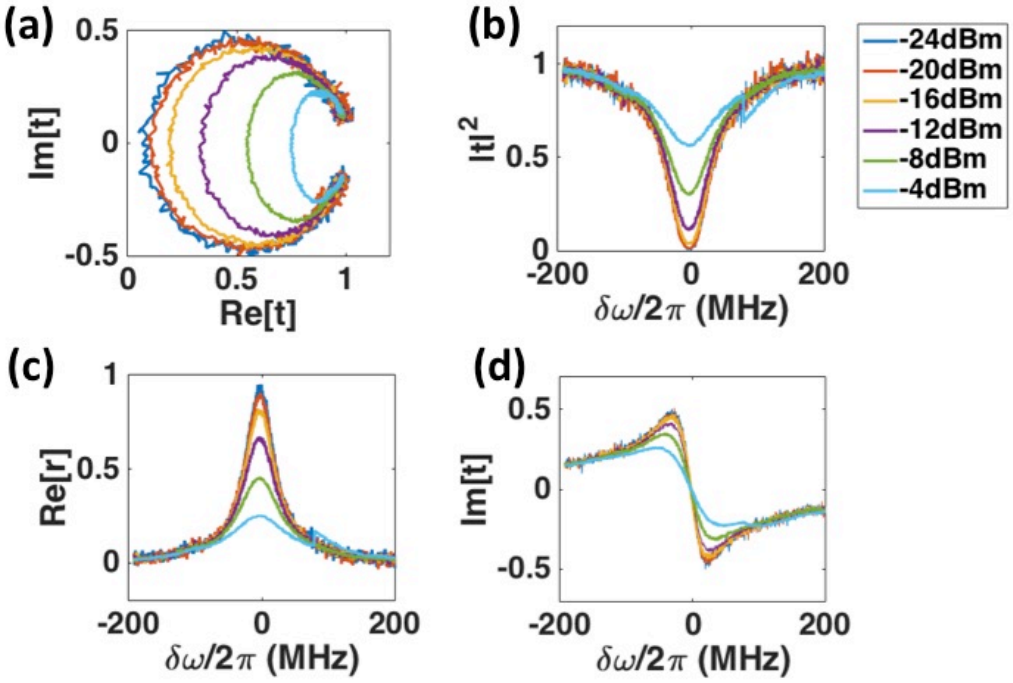

Figure 3.12: Elastic scattering of microwaves on the artificial atom (Qubit ID 5) measured at driving powers −24dBm to −4dBm with a step of 4dBm. (a) Smith chart representation of the microwave transmission for (b) Power extinction $|t|^2$, (c) real part of the reflection coefficient r, and (d) imaginary part of the transmission coefficient t as a function of frequency detuning $\delta\omega/2\pi$ from the atomic transition $\omega_0/2\pi = 14.678$ GHz.

is then delivered to the sample chip through a coaxial cable and attenuated by 40dB at room temperature, 10dB at 4K, and 30db at 15mK before interacting with the qubit.

During Δt_P, the state vector rotates in the $y-z$ plane around the x axis of the Bloch sphere with Rabi frequency Ω that is proportional to the amplitude of the incident microwave pulse P. After time Δt_P, the state vector on the Bloch sphere is at an angle $2\pi\Omega\Delta t_P$ to the z axis.

The output signal is amplified at 4K and at room temperature. We apply a read out pulse for a time Δt_R that is shaped by an additional chopper to detect the dynamics of the qubit using a VNA. A schematic diagram of the pulse sequence is shown in Fig. 3.13(a). The measurement yields Rabi

oscillations as a function of time (Fig. 3.13(b)). We measure the decaying Rabi oscillations as a function of incident pulse length Δt_P and driving power (Fig. 3.14).

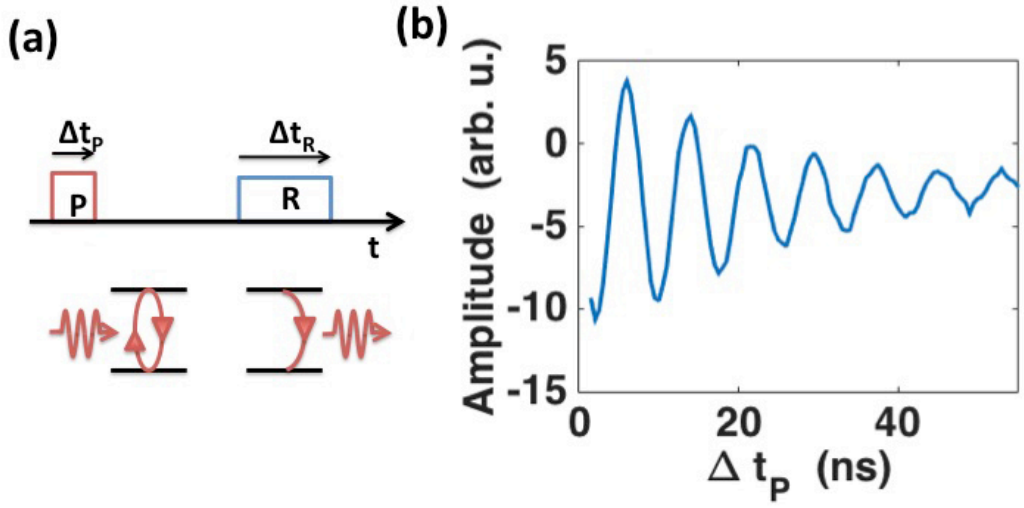

Figure 3.13: Rabi oscillations (a) pulse sequence: The driving pulse P prepares the atomic states, and the emission from the atom is detected during the readout pulse R. (b) The measurement yields decaying Rabi oscillations in time (at fixed driving power of −6dBm.

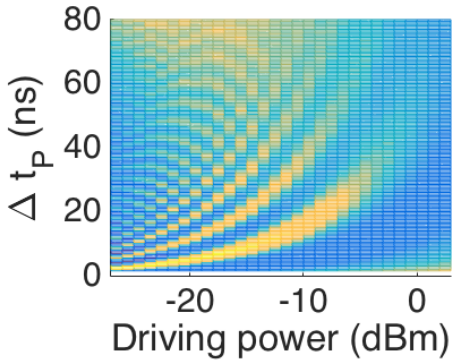

Figure 3.14: Intensity plot of decaying Rabi oscillations as a function of incident pulse length Δt_P and driving power.

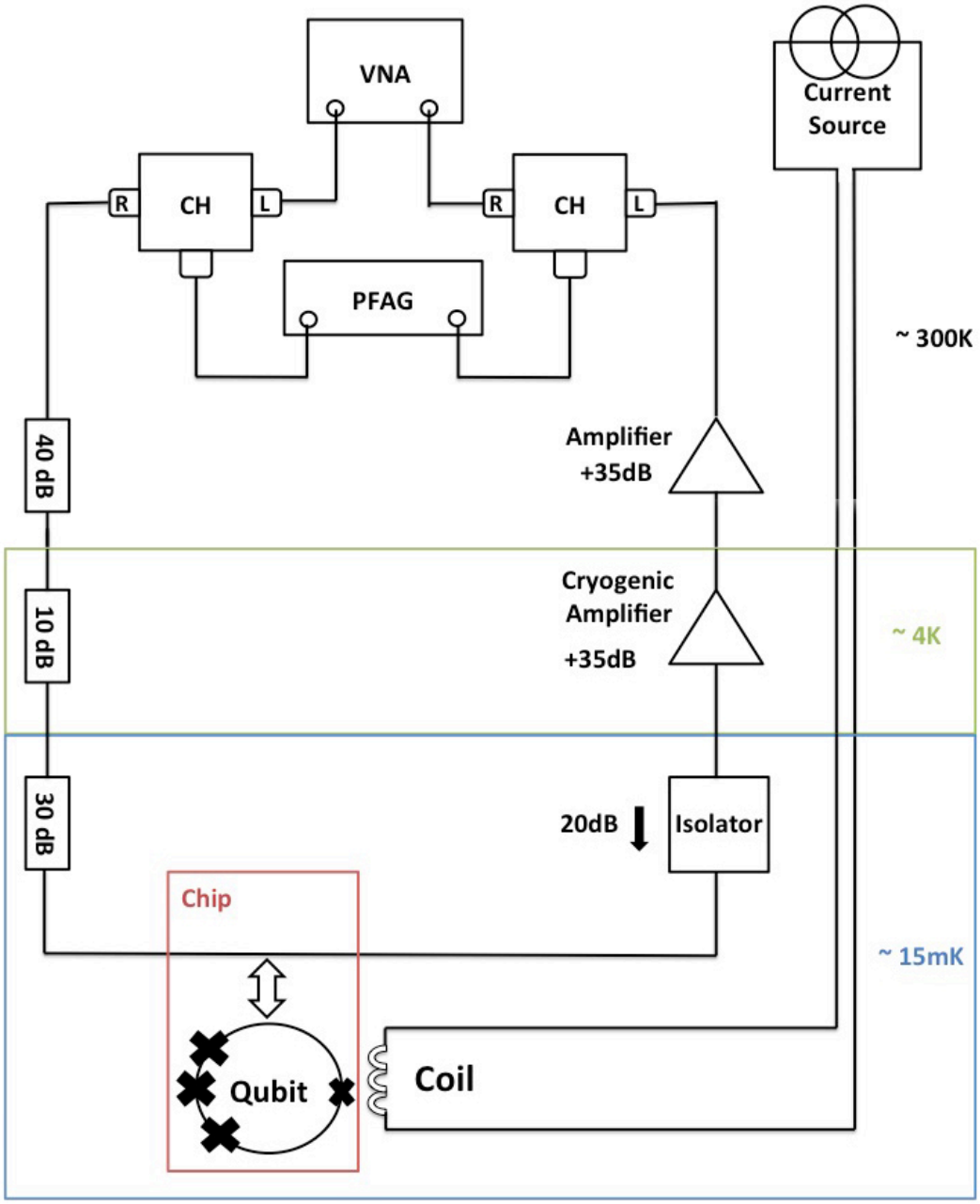

Figure 3.15: Experimental setup for measuring Rabi oscillations. A microwave pulse is formed using a chopper consisting of two IQ modulation mixers, a splitter, a low pass filter, and some attenuators (see Fig 3.8). The Vector Network Analyser (VNA) provides the continuous coherent microwave, while the pulse function arbitrary generator (PFAG) generates the pulse envelope, both of which are fed into the chopper. The microwave pulse is then attenuated by 40dB at room temperature, 10dB at 4K, and 30dB at 15mK before interacting with the flux qubit that is biased through a superconducting coil. The output line features an isolator and two amplifiers, one at 4K and the other at room temperature. A read out pulse is formed through an additional chopper on the output line. The output signal is detected by a VNA.

Chapter 4

Quantum wave mixing and visualisation of photonic states

In this chapter, we demonstrate that when a non-linear medium is scaled down to a single quantum scatterer, a series of effects beyond classical physics are revealed. In particular, Quantum Wave Mixing (QWM) is a result of elastic scattering of electromagnetic waves on a single artificial atom.

First, we study continuous wave mixing on a quantum object and observe a symmetric spectrum with an infinite number of side peaks. Then, we investigate two regimes of QWM: Coherent wave mixing and quantum wave mixing with non-classical superposed states. In the former, two pulsed waves with frequencies slightly detuned to each other are scattered on the single artificial atom resulting in a symmetric spectrum with an infinite number of side peaks. The amplitude of each of these peaks oscillates in time according to Bessel functions with the orders determined by the number of interacting photons. In the latter regime, a time delay between the two pulses is introduced causing a striking difference in the spectrum, which now exhibits a finite number of narrow coherent emission peaks. Furthermore, the spectrum in the latter regime is asymmetric with the number of positive frequency peaks (due to stimulated emission) always exceeding by one compared to the negative frequency peaks (due to absorption).

Thus in QWM, the spectrum of elastically scattered radiation is a fin-

gerprint of the interacting photonic states. Moreover, the artificial atom visualises photon-state statistics, for example distinguishing coherent, one- and two-photon superposed states in the quantum regime. Our results give new insight into nonlinear quantum effects in microwave optics with artificial atoms and have been partly published in Nature Communications [1].

4.1 Introduction

A plethora of quantum optical phenomena have been recently demonstrated on chip with superconducting quantum circuits, establishing the research direction of circuit quantum electrodynamics [33, 42, 74]. In particular, superconducting quantum circuits can be used to resolve photon number states in harmonic oscillators [75], manipulate individual photons [76, 77, 78], generate photon (Fock)- [79] and arbitrary quantum states of light [80], demonstrate the lasing effect from a single artificial atom [81], and study nonlinear effects [82, 83].

Artificial atoms can also be coupled to open space (microwave transmission lines) [84] and reveal many interesting effects such as resonance fluorescence of continuous waves [85, 32], elastic and inelastic scattering of single-frequency electromagnetic waves [86, 64], amplification [87], single-photon reflection and routing [88], non-reciprocal transport of microwaves [89], coupling of distant artificial atoms by exchanging virtual photons [90], and superradiance of coupled artificial atoms [91]. All these effects require strong coupling to propagating waves and are thus more challenging to demonstrate in quantum optics with natural atoms due to low-spatial mode matching of propagating light.

Here, we focus on wave mixing effects. From textbooks, we may recall four wave mixing, an optical effect manifesting itself in a pair of frequency side peaks from two driving tones on a classical Kerr-nonlinearity [7, 50]. Scaling the nonlinear medium down to a single artificial atom, that strongly interacts with incident waves, results in time resolution of instant multi-photon interactions

and reveals effects beyond classical physics.

We demonstrate the physical phenomena of continuous wave mixing and quantum wave mixing (QWM) on a single superconducting artificial atom in the open one-dimensional (1D) space (coplanar transmission line on-chip). We show two regimes of QWM comprising different degrees of quantumness: the first and most remarkable one is QWM with nonclassical superposed states, which are mapped into a finite number of frequency peaks.

In another regime, we investigate the different orders of wave mixing of classical coherent waves on the artificial atom. The dynamics of the peaks exhibits a series of Bessel-function Rabi oscillations, different from the usually observed harmonic ones, with orders determined by the number of interacting photons. Therefore, the device utilising QWM visualises photon-state statistics of classical and non-classical photonic states in the open space. The spectra are fingerprints of interacting photonic states, where the number of peaks due to the atomic emission always exceeds by one the number of absorption peaks.

Below, a summary of the main findings of this work: (1) demonstration of the wave mixing effect on a single quantum system; (2) in the quantum regime of mixing, the peak pattern and the number of the observed peaks is a map of coherent and superposed photonic states, where the number of peaks N_{peaks} is related to the number of interacting photons N_{ph} as $N_{peaks} = 2N_{ph}+1$. Namely, the one-photon state (in two-level atoms) results in precisely three emission peaks; the two-photon state (in three-level atoms) results in five emission peaks; and the classical coherent states, consisting of infinite number of photons, produce a spectrum with an infinite number of peaks; (3) Bessel function Rabi oscillations are observed and the order of the Bessel functions depends on the peak position and is determined by the number of interacting photons.

4.2 Sample description

We study the quantum mixing effects on an artificial atom based on a superconducting qubit geometry shown in Fig. 4.1. The atom is a micron-size loop with four nanometer-scale Josephson junctions fabricated by techniques of electron beam lithography and standard two-angle shadow evaporation in the clean room facilities at Royal Holloway. For more details on the fabrication process refer to section 3.2.

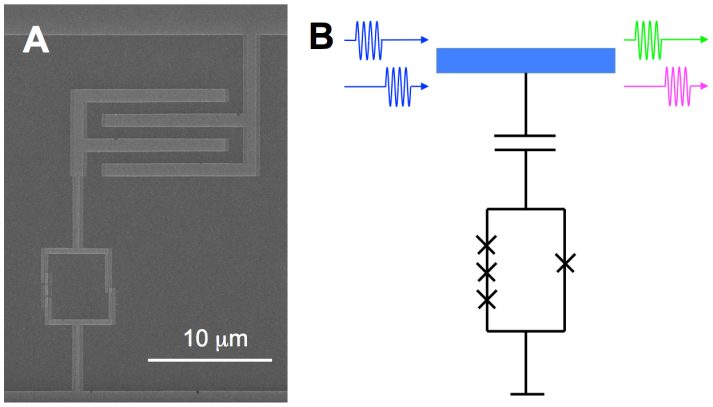

Figure 4.1: The device. (A) SEM image of a flux qubit coupled to the transmission line through an interdigitated capacitance. (B) A schematic circuit representation of the device consisting of a superconducting qubit interrupted by four Josephson junctions.

The artificial atom is coupled through a capacitor to a transmission line. The energy splitting controlled by an external magnetic field is approximated as

$$\hbar\omega_a = \sqrt{(2I_p\delta\Phi)^2 + \Delta^2}, \tag{4.1}$$

where I_p is the persistent current in the loop, $\delta\Phi$ is the magnetic flux threaded through the loop and $\Delta = \hbar\omega_0$ is the tunnelling energy (where ω_0 is the transition frequency of the atom at half flux quantum). Here, we have used the approximation that higher excitation energies of higher eigenstates are much larger than δE, allowing to truncate the Hamiltonian to a two-level system (see sec. 2.3.3). The atom is strongly coupled to the line with negligible dephasing (extinction $|t|^2 \geq 90\%$), comparing to photon emission rate $\Gamma_1/2\pi$.

Experiment	$\Delta = \hbar\omega_0$	α	I_p	C	$\lvert t\rvert^2$	$\Gamma_1/2\pi$
Continuous	$6.4\hbar$ GHz	0.5	~ 50 nA	2 fF	$\geq 95\%$	3 MHz (at $\omega_a \approx 6.4$ GHz)
Pulsed	$6.8\hbar$ GHz	0.45	~ 40 nA	3 fF	$\geq 90\%$	20 MHz (at $\omega_a \approx 9$ GHz)

Table 4.1: Device parameters for this chapter's wave mixing experiments. The artificial atoms are coupled via a capacitance C to the transmission line. Δ is the tunnelling energy, I_p is the persistent current in the loop, and $\delta\Phi$ is the magnetic flux threaded through the loop. Sec. 4.3 is dedicated to the continuous regime, whereas sec. 4.4, 4.5, 4.6 are devoted to the pulsed regime.

We apply coherent microwaves to drive the atom and detect the amplified signal by a spectrum analyser (SPA). We measure in the continuous and in the pulsed regime of the incoming coherent microwave drives. The experimental results presented in this chapter were obtained with the artificial atoms characterised in Table. 4.1.

A transmission spectroscopy of the artificial atom used for the pulsed experiments is shown in Fig. 4.2. At magnetic flux bias $\delta\phi/\phi_0 \approx \pm 0.035$

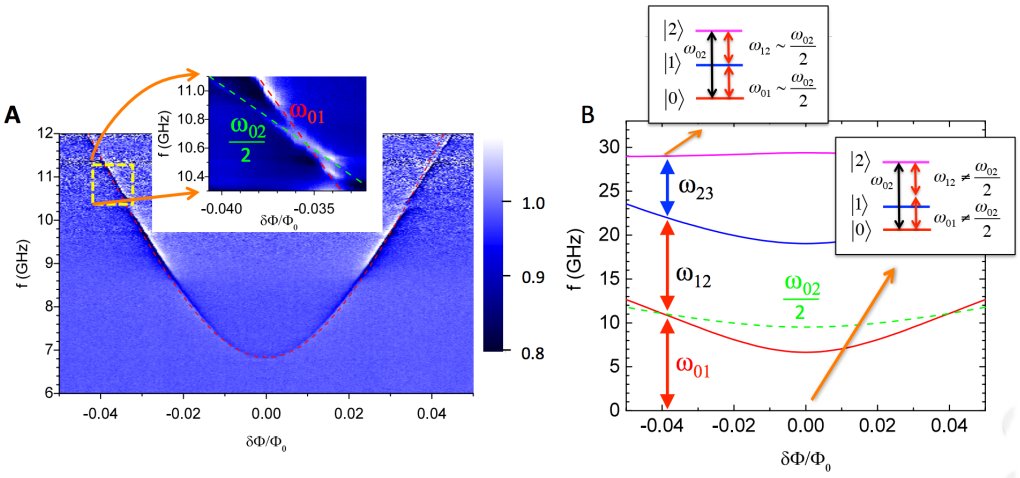

Figure 4.2: Spectroscopy. (A) A transmission spectroscopy of the system as a function of the normalised magnetic flux bias measured by a vector network analyser (VNA). The red dashed curve shows calculations of the energy $\approx \omega_{01}$. An inset shows the transmission phase under a strong drive. A transition line at ω_{01} crosses a line from the two-photon transition process at ω_{02}. The crossing takes place at a point where $\omega_{01} = \omega_{12}$. (B) A simulation of the system energies with parameters close to our artificial atom. The red arrowed lines show two equal transition frequencies $\omega_{01} = \omega_{12} \neq \omega_{23}$. The insets show level schemes at $\delta\Phi/\Phi_0 = \pm 0.035$ and at $\delta\Phi/\Phi_0 = 0$.

transition frequency between the ground and excited state are equal. Therefore the resonant microwave results in population of both levels, which is equivalent to storing the two-photon state $|\gamma\rangle$.

4.3 Stationary coherent wave mixing

We irradiate the artificial atom, described in sec. 4.2, by two continuous propagating microwaves. The experimental set-up is shown in Fig. 4.3. We tune the frequency of the qubit to its degeneracy point $\omega = \Delta/\hbar = 6.4$ GHz. The two microwave tones at frequencies $\omega_+ = \omega + \delta\omega$ and $\omega_- = \omega - \delta\omega$ are slightly detuned from the resonance of the artificial atom. The detuning is chosen to be $\delta\omega = 1\text{kHz} << \Gamma_1, \Gamma_2$ such that both tones are in resonance with the qubit but still spectrally well separated. Since the qubit is essentially a non-linear system, we expect mixing effects to occur.

Naively, we may attribute these mixing effects to elastic scattering events of photons. For example, a photon at $2\omega_- - \omega_+$ is emitted as a result of absorption of two photons from the ω_+-mode and emission of a single photon from the ω_--mode. Similarly a photon at $2\omega_+ - \omega_-$ is created due to absorption of two photons from the ω_--mode and emission of a single photon from the ω_+-mode. These processes are called degenerate four-wave mixing.

As long as the two driving modes consist of many propagating photons in timescales comparable to relaxation and dephasing rates, Γ_1 and Γ_2 respectively, higher-order processes of wave mixing will be present resulting in emitted photons at frequencies $\omega_{\pm(2p+1)} = (p+1)\omega_\pm - p\omega_\mp$ with $(2p+1)$ photons involved in the process, as illustrated in Fig. 4.4(a).

The output spectrum consisting of the two driving microwaves and n side peaks is measured by a spectrum analyser (SPA). We observe up to four side peaks, i.e. 9-photon-processes, as shown in Fig. 4.4(c),(d). To verify that the nonlinear scattering takes place on our single artificial atom, we tune the magnetic field away from the qubit and demonstrate that wave mixing effects no longer occur (Fig. 4.4(b)).

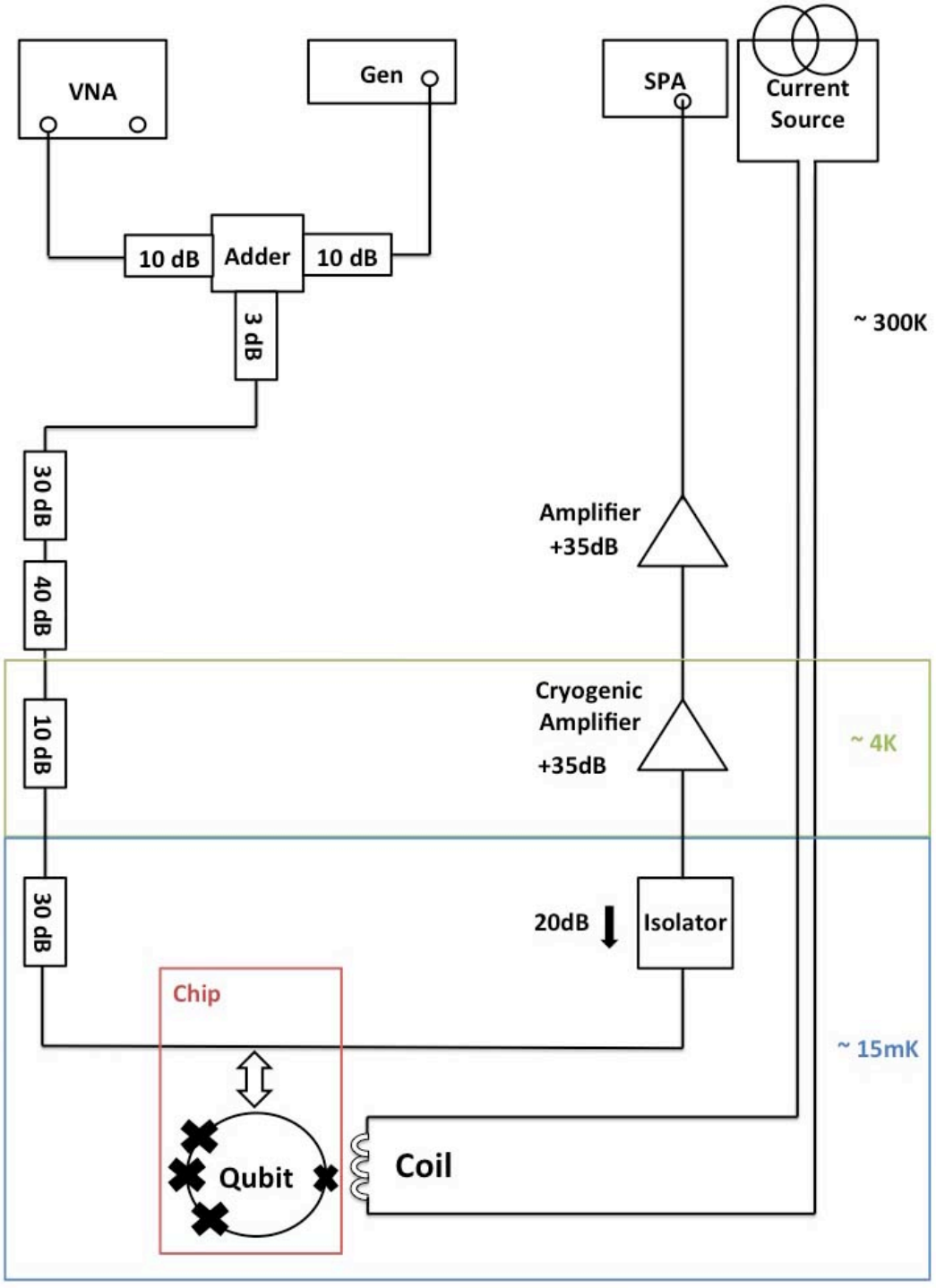

Figure 4.3: Experimental setup for wave mixing in the continuous regime. Two continuous microwaves slightly detuned from each other and from the resonance of the atom are generated, added and delivered to the artificial atom (Fig. 4.1). The output is amplified twice and then measured by a Spectrum Analyser (SPA).

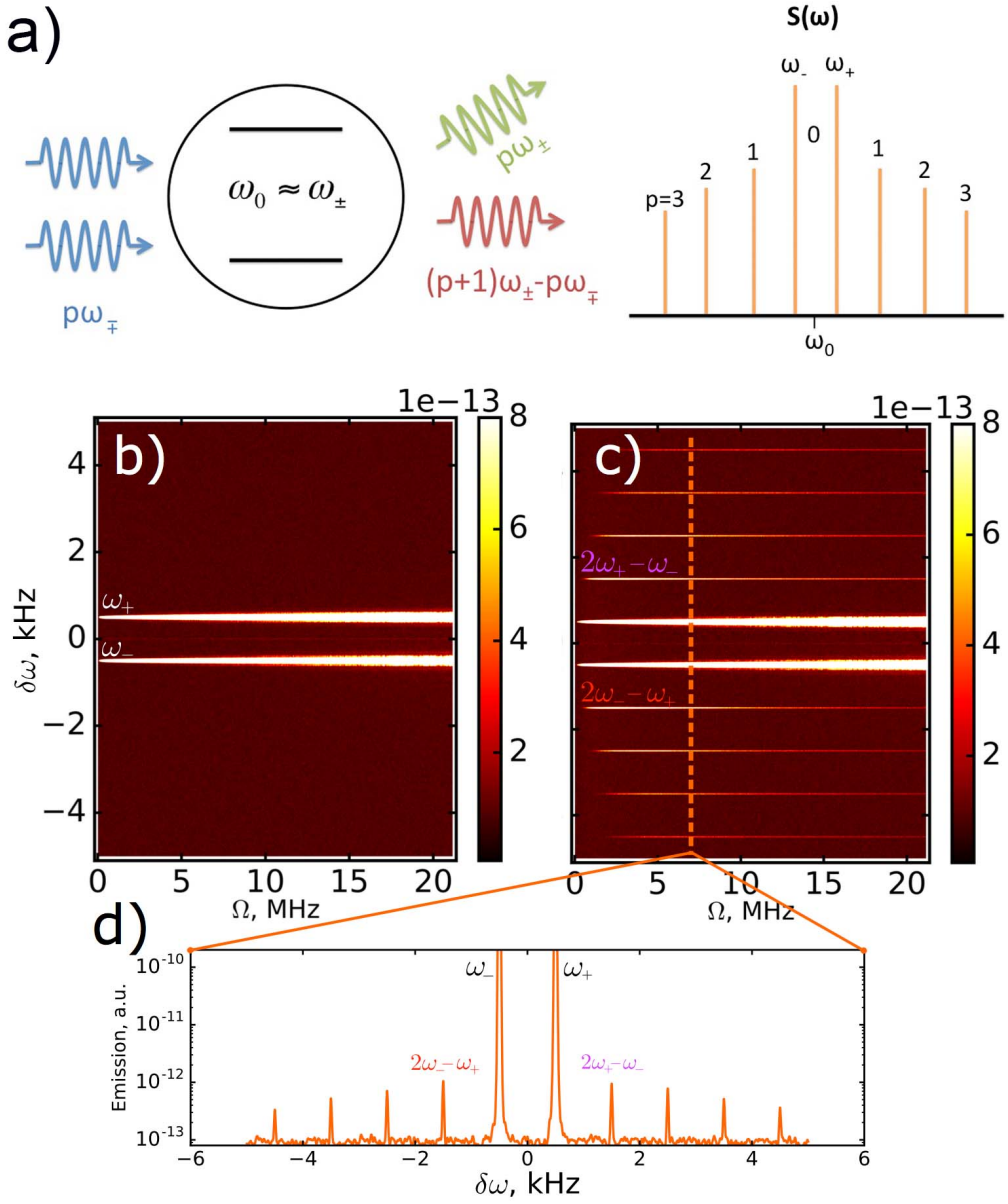

Figure 4.4: (a) Schematic of the concept and resulting spectrum of wave mixing on a single two-level system. (b) and (c) show spectra of coherently scattered radiation measured when the driving tones are either (b) off-resonant or (c) resonant with the qubit, plotted as a function of the amplitude of both drives $\Omega = \Omega_+ = \Omega_-$. (d) An averaged trace at fixed driving amplitude Ω measured by a spectrum analyser.

In sec. 4.7.1 we derived an analytical expression for the intensity of each side peak

$$|\Omega^{em}_{\pm(2p+1)}|^2 = \left(\frac{\Gamma_1 A}{\alpha} y^p (\Omega_\mp + y\Omega_\pm)\right)^2 \tag{4.2}$$

with

$$A = \frac{\Gamma_1 \lambda}{2(\Gamma_1|\lambda|^2 + \Gamma_2(\Omega_-^2 + \Omega_+^2))}, \quad \lambda = \Delta\omega - i\Gamma_2, \quad y = -\sqrt{\frac{(1-\alpha)}{1+\alpha}}, \\ \alpha = \sqrt{(1-\beta^2)}, \quad \beta = \frac{2\Gamma_2\Omega_-\Omega_+}{\Gamma_1|\lambda|^2 + \Gamma_2(\Omega_-^2 + \Omega_+^2)}, \tag{4.3}$$

where we have started from the Hamiltonian of a single two-level system driven by two microwaves with amplitudes Ω_- and Ω_+,

$$H = -\frac{\hbar\omega_a}{2}\sigma_z - \hbar\Omega_-\sigma_x\cos(\omega t - \delta\omega t) - \hbar\Omega_+\sigma_x\cos(\omega t + \delta\omega t). \tag{4.4}$$

We measure the intensity of each spectral component with increasing driving amplitudes, $\Omega = \Omega_- = \Omega_+$, in a wide range. The result is presented in Fig. 4.5(a) and is well fitted by Eq. 4.2 where $\Delta\omega = 1$kHz, $\Gamma_1/2\pi = 2.2$MHz, $\Gamma_2 = 1.1$MHz and peak order parameter p are already predefined by the experimental setting or qubit characterisation and the only fitting parameter is driving amplitude Ω. The measured data is in agreement with our analytical model. Note how each side peak reaches its maximum at an unique optimal driving amplitude

$$\Omega_{max} = \frac{\sqrt{2}}{4}\sqrt{\Gamma_1\Gamma_2 P(P + \sqrt{P^2+4})} \tag{4.5}$$

where $P = 2p + 1$ and we have assumed equal driving tones. For an artificial atom strongly coupled to the transmission line, we may approximate $\Gamma_2 = \Gamma_1/2$, giving for example $\Omega_{max} = 1.11\Gamma_1$ for $p = 1$, $\Omega_{max} = 1.8\Gamma_1$ for $p = 2$, and $\Omega_{max} = 2.5\Gamma_1$ for $p = 3$.

We then explore the regime of unequal driving amplitudes, we increase Ω_- by 1 dB compared to Ω_+, and observe that the amplitudes of the wave mixing pairs are no longer symmetric (Fig. 4.5(b)). Intensities at $\omega_{-(2p+1)}$ are significantly larger than at $\omega_{+(2p+1)}$. Our system proves to be a promising tool to sense relative powers; to obtain symmetric pairs in amplitude of the mixing pattern one has to apply drives with exactly matched amplitudes.

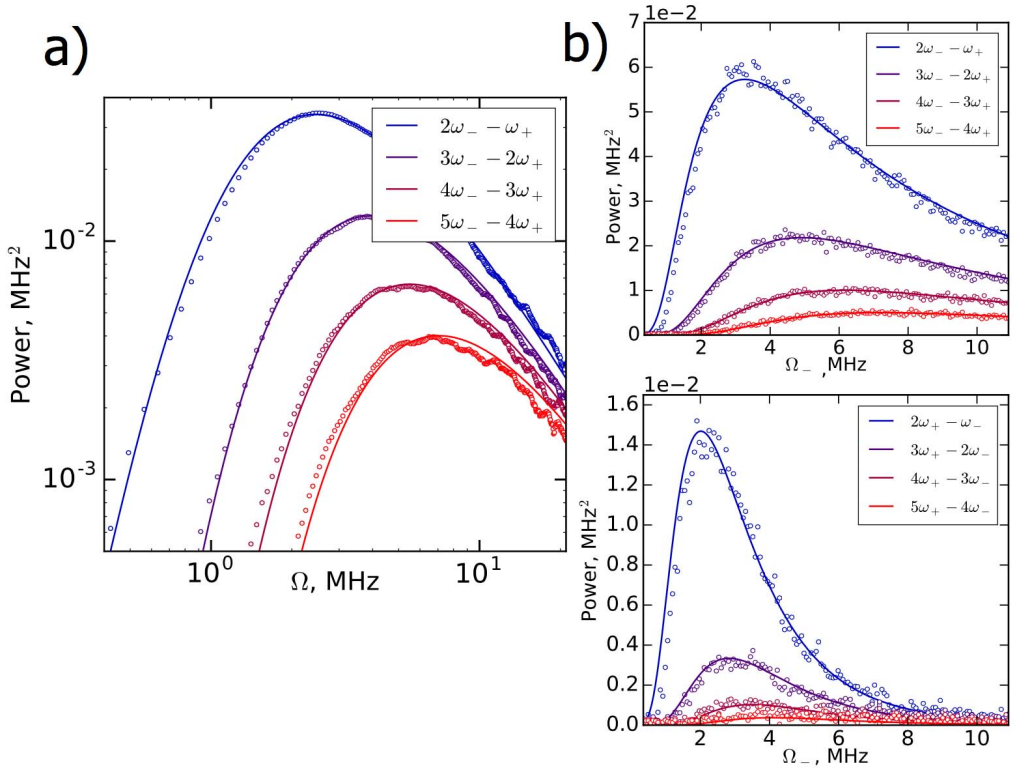

Figure 4.5: Side spectral components of elastically scattered radiation due to wave mixing effects for (a) equal driving amplitudes $\Omega = \Omega_+ = \Omega_-$ and (b) unequal driving amplitudes $\Omega_- > \Omega_+$ by 1dB. The "plus"-components are larger in power compared to the "minus"-components demonstrating high sensitivity of wave mixing peaks to driving amplitudes.

4.4 Pulsed coherent wave mixing

To study the dynamics of wave mixing we perform measurements in the pulsed regime. The experimental measurement circuit is shown in Fig. 4.6.

We may continue to describe the system in the semi-classical picture, however, it does not illustrate the physical entity of QWM. In particular, it fails to separate individual contributions of multi-photon processes into emission and therefore does not illustrate the link to photon statistics of the emitted light. Moreover, the semi-classical picture fails to explain the limited number of spectral components we observe for the case of quantum mixing with delayed pulses. Therefore, for our purposes it is instructive to calculate the same physical quantity from an approach of second quantisation.

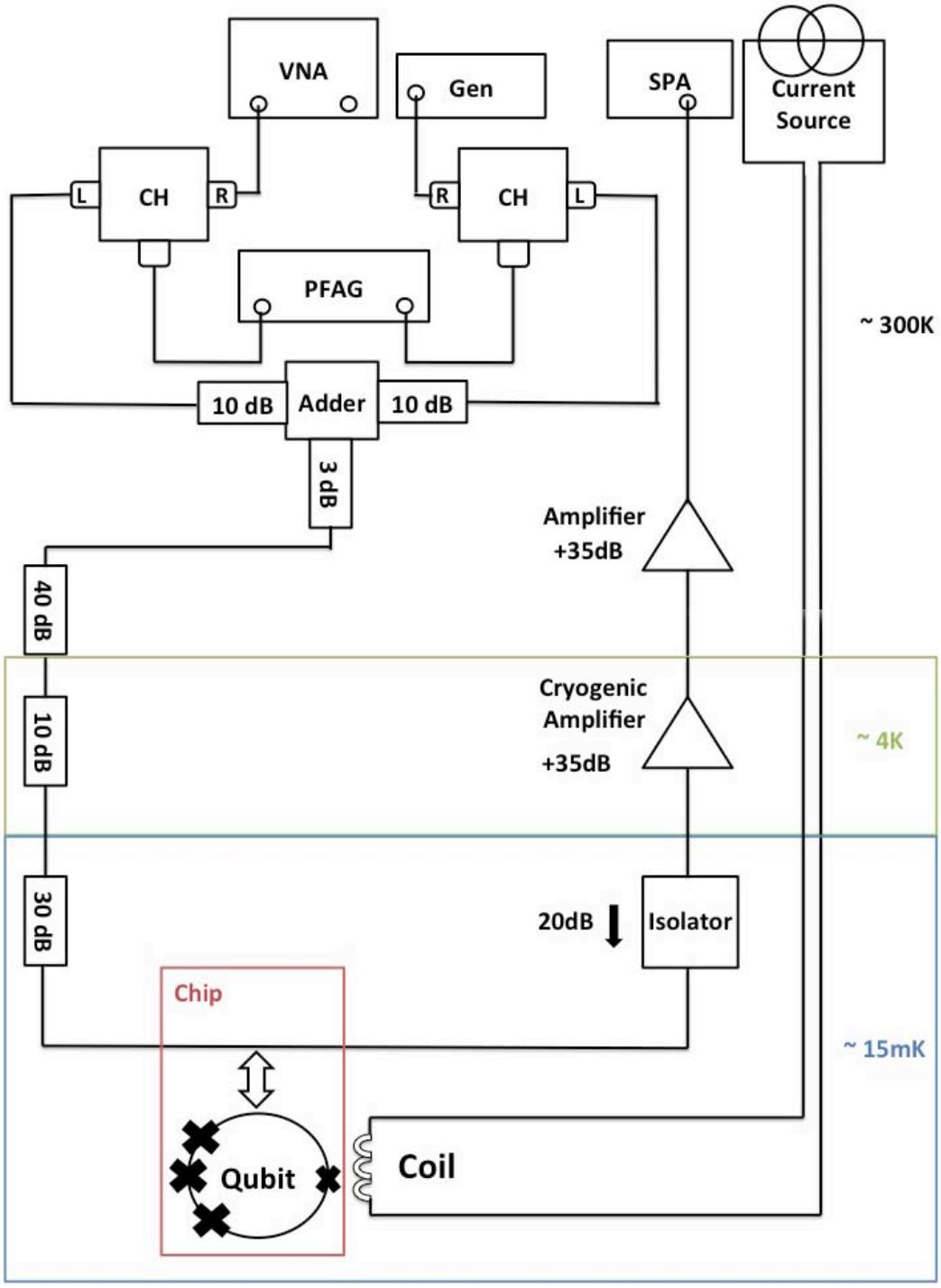

Figure 4.6: Measurement set up for QWM mixing with individual pulse manipulation. A vector network analyser (VNA) and a microwave generator (Gen) are used as microwave sources. The pulse envelope is provided by a pulse function arbitrary generator (PFAG). Pulses are shaped with choppers (CH), added and delivered to the sample. The output is amplified twice and measured using a spectrum analyser (SPA). Additional cables may be added to the circuit to introduce delays between pulses.

4.4.1 Coherent and zero-one photon superposed state

To evaluate the system, we consider electromagnetic waves propagating in a 1D transmission line with an embedded two-level artificial atom [32] as shown in Fig. 4.1(A), and Fig. 4.7(a).

Since we are interested in photon statistics, which will be revealed by QWM, we consider our system in the photon basis. The coherent wave in the photon (Fock) basis $|N\rangle$ is presented as

$$|\alpha\rangle = e^{-\frac{|\alpha|^2}{2}}\left(|0\rangle + \alpha\,|1\rangle + \frac{\alpha^2}{\sqrt{2!}}\,|2\rangle + \frac{\alpha^3}{\sqrt{3!}}\,|3\rangle + ...\right) \tag{4.6}$$

and consists of an infinite number of photonic states. A two-level atom with ground and excited states $|g\rangle$ and $|e\rangle$ driven by the field can be prepared in superposed state $\Psi = \cos\frac{\theta}{2} + \sin\frac{\theta}{2}\,|e\rangle$ and, if coupled to the external photonic modes, transfers the excitation to the mode, creating zero-one photon superposed state

$$|\beta\rangle = \left|\cos\frac{\theta}{2}\right|(|0\rangle + \beta\,|1\rangle), \tag{4.7}$$

where $\beta = -\tan\frac{\theta}{2}$ (sec. 4.7.2). The superposed state comprises coherence, however $|\beta\rangle$ state is different from classical coherent state $|\alpha\rangle$, the latter consisting of an infinite number of Fock states. The energy exchange process is described by the operator $b^- b^+\,|g\rangle\langle g| + b^+\,|g\rangle\langle e|$, which maps the atomic to photonic states, where $b^+ = |1\rangle\langle 0|$ and $b^- = |0\rangle\langle 1|$ are creation/annihilation operators of the zero-one photon state. The operator is a result of a half-period oscillation in the evolution of the atom coupled to the quantised photonic mode (see eq. 4.32) and we keep only relevant terms for the discussed case (an excited atom and an empty photonic mode) (see Sec 4.7.2).

We discuss and demonstrate experimentally an elastic scattering of two waves with frequencies $\omega = \omega_0 - \delta\omega$ and $\omega_+ = \omega_0 + \delta\omega$, where $\delta\omega$ is a small detuning, on a two-level artificial atom with energy splitting $\hbar\omega_0$. The scattering, taking place on a single artificial atom, allows us to resolve instant multi-photon interactions and statistics of the processes. Dealing with the fi-

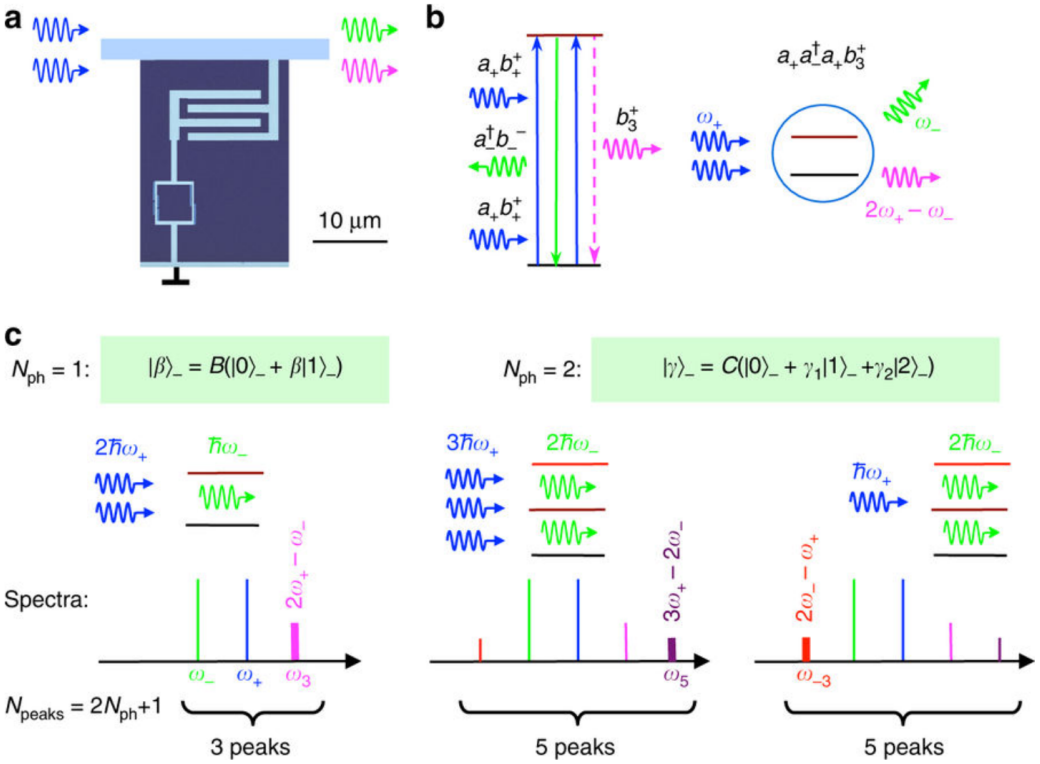

Figure 4.7: Principles of the device operation. (a) False coloured SEM image of the device: an electronic circuit (a superconducting four Josephson junction loop), behaving as an artificial atom, embedded into a transmission line, strongly interacts with propagating electromagnetic waves. (b) The four-wave mixing process results in the zero-one photon field creation at $\omega_3 = 2\omega_+ - \omega_-$. In classical mixing, process $a_+a^\dagger a_+ b_3^+$ comes in a pair with the symmetric one $aa_+^\dagger ab_{-3}^+$. In the mixing with non-classical states, the time-symmetry and, therefore, spectral symmetry are broken. (c) In QWM, the number of spectral peaks is determined by the number of photonic (Fock) states forming the superposed state in the atom. The state is created by the first pulse at ω_- and then mixed with the second pulse of ω_+. Single-photon ($N_{ph} = 1$) state $|\beta\rangle_- = B(|0\rangle + \beta\,|1\rangle)$ can only create a peak at $\omega_3 = 2\omega_+\omega_-$ because only one photon at can be emitted from the atom. Two photon ($Nph = 2$) superposed state $|\gamma\rangle_- = C(|0\rangle + \gamma_1\,|1\rangle + \gamma_2\,|2\rangle)$ results in the creation of an additional peak at $3\omega_+2\omega$, because up to two photons can be emitted. Also two photons of ω_- can be absorbed, creating an additional left-hand-side peak at $2\omega_-\omega_+$.

nal photonic states, the system Hamiltonian is convenient to present as the one, which couples the input and output fields

$$H = i\hbar g(b_-^+ a_- - b_-^- a_-^\dagger + b_+^+ a_+ - b_+^- a_+^\dagger), \tag{4.8}$$

using creation and annihilation operators $a_{\pm}^{\dagger}$ ($a_{\pm}$) of photon states $|N\rangle_{\pm}$ (N is an integer number) and $b_{\pm}^{+}$ and $b_{\pm}^{-}$ are creation/annihilation operators of single-photon output states at frequencies $\omega_{\pm}$. Here $\hbar g$ is the field-atom coupling energy. Operators $b_{\pm}^{+}$ and $b_{\pm}^{-}$ also describe the atomic excitation/relaxation, using substitutions $b_{\pm}^{+} \leftrightarrow e^{\mp i\varphi} |e\rangle \langle g|$ and $b_{\pm}^{-} \leftrightarrow e^{\pm i\varphi} |e\rangle \langle g|$, where $\varphi = \delta\omega t$ is a slowly varying phase (see Sec. 4.7.3). The phase rotation results in the frequency shift according to $\omega_{\pm} t = \omega_0 t \pm \delta\omega t$ and more generally for $b_m^{\pm}$ (with integer m) the varied phase $m\delta\varphi$ results in the frequency shift $\omega_m = \omega_0 + m\delta\omega$.

The system evolution over the time interval $[t, t']$ ($t' = t + \Delta t$ and $\delta\omega\Delta t \ll 1$) described by the operator $U(t, t') = \exp(iH\Delta t/\hbar)$ can be presented as a series expansion of different order atom-photon interaction processes $a_{\pm}^{\dagger} b_{\pm}^{-}$ and $a_{\pm} b_{\pm}^{+}$ - sequential absorption-emission accompanied by atomic excitations/relaxations (4.7.3). Operators b describe the atomic states (instant interaction of the photons in the atom) and, therefore, satisfy the following identities: $b_p^{-} b_m^{+} = |0\rangle_{m-p} \langle 0|$, $b_j^{\pm} b_p^{\mp} b_m^{\pm} = b_{j-p+m}^{\pm}$, $b_p^{\pm} b_m^{\pm} = 0$. The excited atom eventually relaxes producing zero-one superposed photon field $|\beta\rangle_m$ at frequency $\omega_m = \omega_0 + m\delta\omega$ according to $b + m|0\rangle = |1\rangle_m$.

We repeat the evolution and average the emission on the time interval $t > \delta\omega - 1$ and observe narrow emission lines. In the general case, the atom in a superposed state generates coherent electromagnetic waves of amplitude

$$V_m = -\frac{\hbar\Gamma_1}{q_p} \langle b_m^{+} \rangle \tag{4.9}$$

at frequency ω_m , where Γ_1 is the atomic relaxation rate and q_p is the atomic dipole moment [32, 64].

4.4.2 Elastic scattering and Bessel function Rabi oscillations

To study QWM, we couple the single artificial atom (a superconducting loop with four Josephson junctions) to a transmission line via a capacitance (sample description 4.2). The atom relaxes with the photon emission rate found to

be $\Gamma_1/2\pi \approx 20$MHz. The coupling is strong, which means that any non-radiative atom relaxation is suppressed and almost all photons from the atom are emitted into the line. The sample is held in a dilution refrigerator with base temperature 15mK.

We apply periodically two simultaneous microwave pulses with equal amplitudes at frequencies ω_- and ω_+, length $\Delta t = 2$ ns and period $T_r = 100$ns (much longer than the atomic relaxation time $\Gamma_1^{-1} \approx 84$ns). A typical emission power spectrum integrated over many periods (bandwidth is 1kHz) is shown in Fig. 4.8(a). The pattern is symmetric with many narrow peaks (as narrow as the excitation microwaves), which appeared at frequencies $\omega_0 \pm (2k+1)\delta\omega$, where $k \geq 0$ is an integer number.

We linearly change driving amplitude (Rabi frequency) Ω, which is defined from the measurement of harmonic Rabi oscillations under single-frequency excitation. The dynamics of several side peaks versus linearly changed $\Omega\Delta t$ (here we vary Ω, however, equivalently Δt can be varied) is shown on plots of Fig. 4.8(b). Note that the peaks exhibit anharmonic oscillations well fitted by the corresponding $2k+1$-order Bessel functions of the first kind. The first maxima are delayed with the peak order, appearing at $\Omega\Delta t \propto k+1$. Note also that detuning $\delta\omega$ should be within tens of megahertz ($\leq \Gamma_1$). Here, we use $\delta\omega/2\pi = 10$kHz to be able to quickly span over several $\delta\omega$ of the spectrum analyser (SPA) with the narrow bandwidth.

Figure 4.7(b) exemplifies the third-order process (known as the four-wave mixing in the case of two side peaks), resulting in the creation of the right hand-side peak at $\omega_3 = 2\omega_+ - \omega_-$. The process consists of the absorption of two photons of frequency ω_+ and the emission of one photon at ω_-.

More generally, the $2k+1$-order peak at frequency $\omega_{2k+1} = (k+1)\omega_+ - k\omega_-(\equiv \omega_0 + (2k+1)\delta\omega)$ is described by the multi-photon process $(a_+ a_-^\dagger)^k a_+ b_{2k+1}^+$, which involves the absorption of $k+1$ photons from ω_+ and the emission of p photons at ω_-; and the excited atom eventually generates a photon at ω_{2k+1}. The symmetric left hand-side peaks at $\omega_0 - (2k+1)\delta\omega$ are

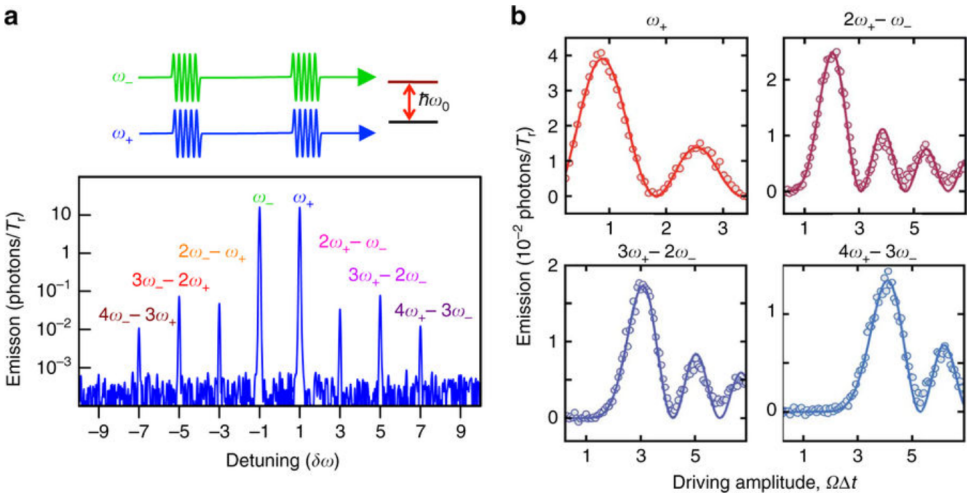

Figure 4.8: Dynamics of coherent wave mixing.(a) An example of a spectrum of scattered microwaves, when two simultaneous periodic pulses of equal amplitudes and frequencies ω_- and ω_+ are applied according to the top time diagram. The mixing of coherent fields $|\alpha\rangle_\pm$, consisting of an infinite number of photonic states results in the symmetric spectrum with an infinite number of side peaks, which is the map of classical states. (b) Four panels demonstrate anharmonic Rabi oscillations of the peaks at frequencies $\omega_0 + (2k+1)\delta\omega$. The measured data (dots) are fitted by squares of $2k+1$-order Bessel functions of the first kind (solid lines). The orders are equal to the interacting photon numbers.

described by a similar processes with swapped indexes ($+ \leftrightarrow -$). The peak amplitudes from Eq. 4.9 are described by expectation values of b-operators, which at frequency ω_{2k+1} can be written in the form of $\langle b^+_{2k+1}\rangle = D_{2k+1}\,\langle (a_+ a^\dagger_-)^k a_+\rangle$. The prefactor D_{2k+1} depends on the driving conditions and can be calculated summing up all virtual photon processes (e.g., $a^\dagger_+ a_+$, $a^\dagger_- a_-$, etc.) not changing frequencies (see Sec. 4.7.3). For instance, the creation of a photon at $2\omega_+ - \omega_-$ is described by $\langle b^+_3\rangle = D_3\,\langle a_+ a^\dagger_- a_+\rangle$.

As the number of required photons increases with k, the emission maximum takes longer time to appear (Fig. 4.8(b)). To derive the dependence observed in our experiment, we consider the case with initial state $\Psi = |0\rangle \otimes (|\alpha\rangle_- + |\alpha\rangle_+)$ and $\alpha \gg 1$. We find then that the peaks exhibit Rabi oscillations described by $\langle b_{2k+1}\rangle = ((-1)^k/2) J_{2k+1}(2\Omega\Delta t)$ (Eq. 4.53) and

the mean number of generated photons per cycle in $2k+1$-mode is

$$\langle N_{\pm(2k+1)} \rangle = \frac{J^2_{\pm(2k+1)}(2\Omega\Delta t)}{4}. \tag{4.10}$$

The symmetric multi-peak pattern in the spectrum is a map of an infinite number of interacting classical coherent states. The dependence from the parameter $2\Omega\Delta t$ observed in our experiment can also be derived using a semiclassical approach, where the driving field is given by $\Omega e^{i\delta\omega t} + \Omega e^{i\delta\omega t} = 2\Omega \cos \delta\omega t$. As shown in Sec. 4.7.3, a classical description can be mathematically more straightforward and leads to the same result, but fails to provide a qualitative picture of QWM discussed below. The Bessel function dependencies have previously been observed in multi-photon processes, however this was in the frequency domain [92, 93, 94].

4.5 Quantum wave mixing

Next, we demonstrate one of the most interesting results: QWM with non-classical photonic states. We further develop the two-pulse technique separating the excitation pulses in time. Breaking time-symmetry in the evolution of the quantum system should result in asymmetric spectra and the observation of series of spectacular quantum phenomena. The upper panel in Fig. 4.9(a) demonstrates such a spectrum, when the pulse at frequency ω_+ is applied after a pulse at ω_-. Notably, the spectrum is asymmetric and contains only one side peak at frequency $2\omega_+ - \omega_-$. There is no signature of any other peaks, which is in striking contrast with Fig. 4.8(a). The background has been subtracted in the measured spectrum shown in the lower panel of Fig. 4.9(a) and the noise is given by $k_B T \Delta f$ where k_B is the Boltzmann constant, T is the temperature of the amplifier, and Δf is the bandwidth of the spectrum analyser. Reversing the pulse sequence mirror reflects the pattern revealing the single side peak at $2\omega_- - \omega_+$ (not shown here).

The quantitative explanation of the process is provided on the left panel of Fig. 4.7(c). The first pulse prepares superposed zero-one photon state $|\beta\rangle_-$

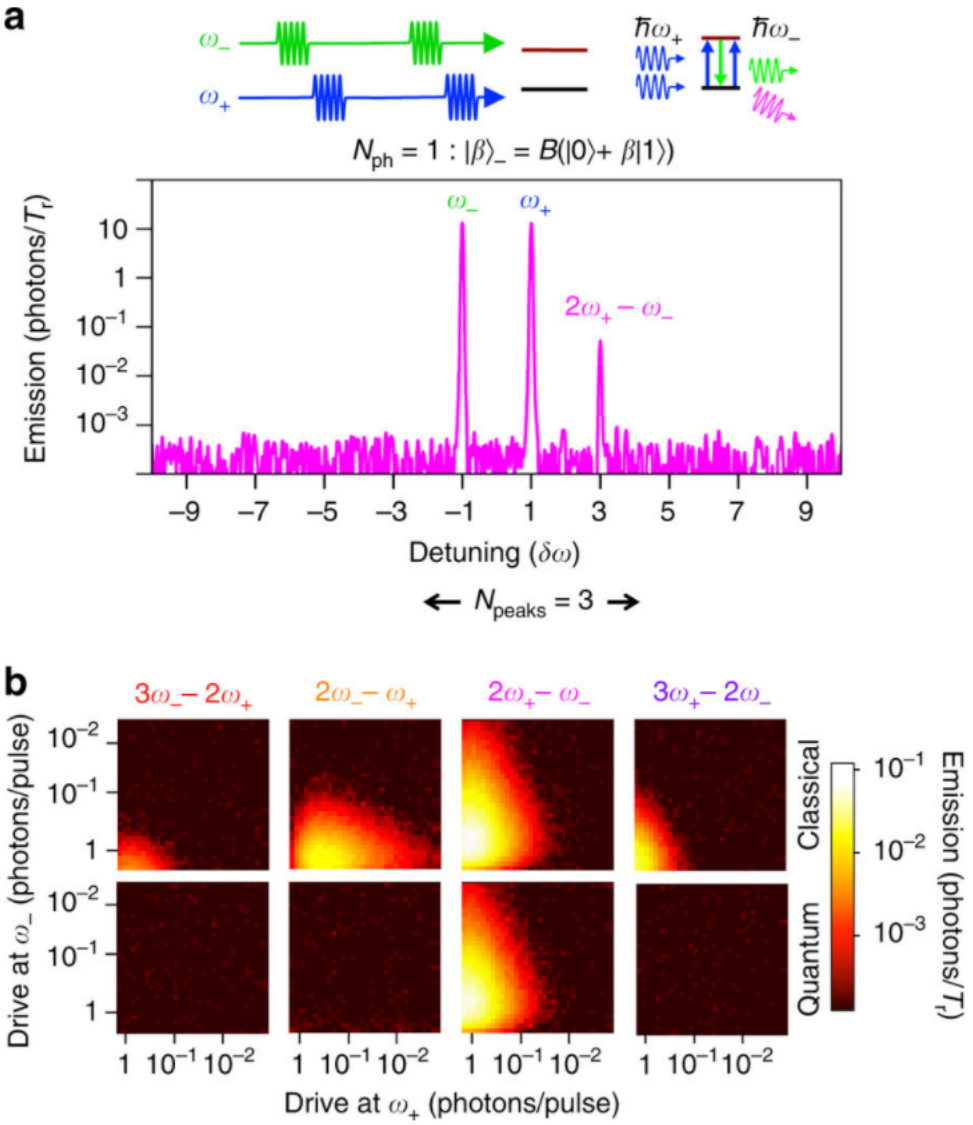

Figure 4.9: Quantum wave mixing with non-classical states. (a) Two consecutive pulses at $\omega_- = \omega_0 - \delta\omega$ and then at $\omega_+\omega_0 - \delta\omega$ are applied to the artificial two-level atom with $\delta\omega = 1$kHz, $\omega_0 \approx 9$GHz. The plot exemplifies the QWM power spectrum from the zero-one photon coherent state $|\beta\rangle_-$. The single side peak at $2\omega_+ - \omega_-$ appears, due to the transformation of $|\beta\rangle_-$ (one photon, $N_{ph} = 1$, from $|\beta\rangle_-$ and two photons from $|\alpha\rangle_+$). (b) The peak amplitude dependences at several side-peak positions in classical (left column) and quantum with the two-level atom (right column) wave mixing regimes as functions of both driving amplitudes ($\alpha_\pm$) expressed in photons per cycle. Several side peaks are clearly visible in the classical regime. This is in striking difference from the quantum regime, when only one peak at $2\omega_+ - \omega_-$ is observed and behaves qualitatively similar to the one in the classical regime.

in the atom, which contains not more than one photon ($N_{ph} = 1$). Therefore, only a single-positive side peak $2\omega_+ - \omega_-$ due to the emission of the ω_--photon, described by $a_+ a_-^\dagger a_+$, is allowed. We describe the process in more detail in sec. 4.7.4.

To experimentally prove that there are no signatures of other peaks, except for the observed three peaks, we vary the peak amplitudes and compare the classical and QWM regimes with the same conditions. Figure 4.9(b) demonstrates the side peak power dependencies in different mixing regimes: classical (two simultaneous pulses) (left panels) and quantum (two consecutive pulses) (right panels). The two cases reveal a very similar behaviour of the right hand-side four-wave mixing peak at $2\omega_+ - \omega_-$, however the other peaks appear only in the classical wave mixing, proving the absence of other peaks in the mixing with the quantum state.

The asymmetry of the output mixed signals, in principle, can be demonstrated in purely classical systems. It can be achieved in several ways, e.g., with destructive interference, phase-sensitive detection/amplification [95], filtering. All these effects are not applicable to our system of two mixed waves on a single point-like scatterer in the open (wide frequency band) space. What is more important than the asymmetry is that the whole pattern consists of only three peaks without any signature of others.

This demonstrates another remarkable property of our device: it probes photonic states, distinguishing the coherent, $|\alpha\rangle$, and superposed states with the finite number of the photon states. Moreover, the single peak at ω_3 shows that the probed state was $|\beta\rangle$ with $N_{ph} = 1$. This statement can be generalised for an arbitrary state. According to the picture in Fig. 4.7(c), adding a photon increases the number of peaks from the left- and right-hand side by one, resulting in the total number of peaks $N_{peaks} = 2N_{ph} + 1$.

4.6 Probing the two-photon superposed state

To gain deeper insight into the state-sensing properties and to demonstrate QWM with different photon statistics, we extended our experiment to two-photon states ($N_{ph} = 2$). The two lowest transitions in our system can be tuned by adjusting external magnetic fields to be equal to $\hbar\omega_0$, though higher transitions are off-resonant ($\neq \hbar\omega_0$, see Fig. 4.2). In the three-level atom, the microwave pulse at ω_- creates the superposed two-photon state

$$|\gamma\rangle_- = C(|0\rangle_- + \gamma_1 |1\rangle_- + \gamma_2 |2\rangle), \tag{4.11}$$

where $C = \sqrt{1 + |\gamma_1|^2 + |\gamma_2|^2}$.

The plot in Fig. 4.10 shows the modified spectrum. As expected, the spectrum reveals only peaks at frequencies consisting of one or two photons of ω_-. The frequencies are $\omega_3 = 2\omega_+ - \omega_-$, $\omega_3 = 2\omega_- - \omega_+$, and $\omega_5 = 3\omega_+ - 2\omega_-$ corresponding, for instance, to processes $a_+ a_-^\dagger a_+ c_3^+$, $a_- a_- a_+^\dagger c_{-3}^+$ and $a_+ a_-^\dagger a_-^\dagger a_+ a_+ c_5^+$, where c_m^+ and c_m^- are creation and annihilation operators defined on the two-photon space ($|n\rangle$, where n takes 0, 1 or 2). The intuitive picture of the two-photon state mixing is shown on the central and right-hand side panels of Fig. 4.7(c). The two photon state ($N_{ph} = 2$) results in the five peaks. This additionally confirms that the atom resolves the two-photon state. For a more detailed description of the two-photon quantum mixing process refer to sec. 4.7.5.

QWM can also be understood as a transformation of the quantum states into quantised frequencies similar to the Fourier transformation. The summarised two-dimensional plots with N_{ph} are presented in Fig. 4.13. The mixing with quantum states manifests itself in an asymmetric spectrum. Note that for arbitrary N_{ph} coherent states, the spectrum asymmetry will remain, giving N_{ph} and N_{ph-1} peaks at the emission and absorption sides.

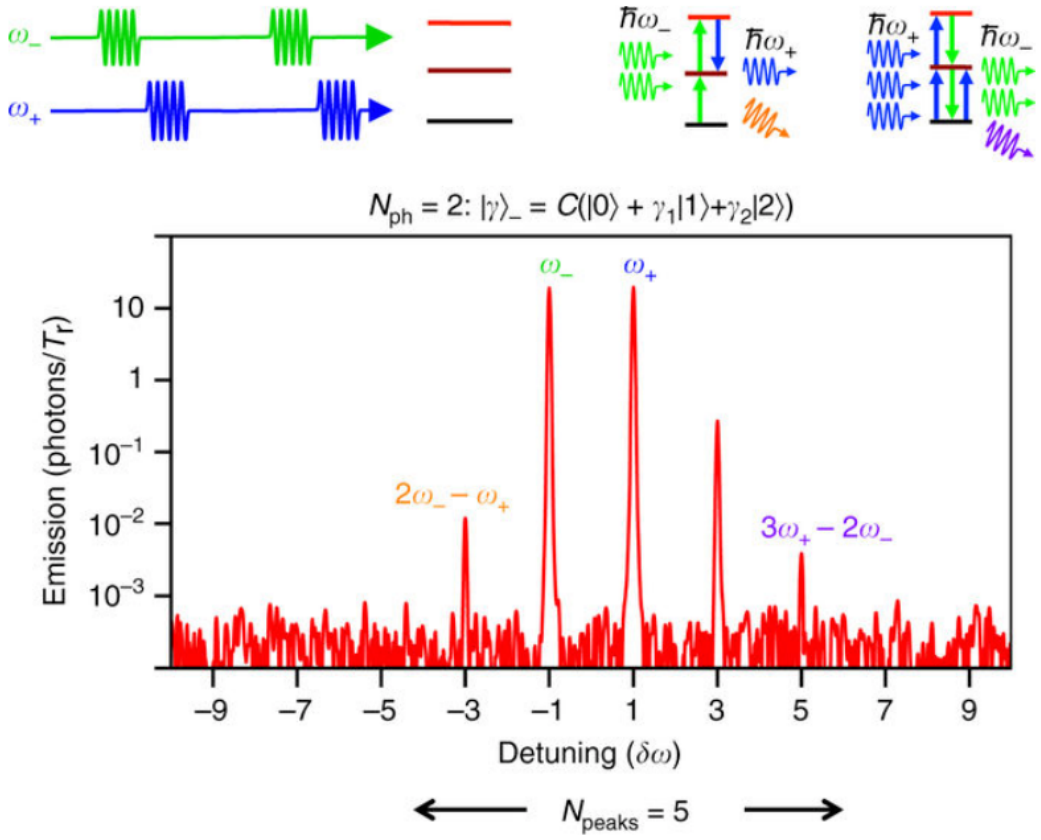

Figure 4.10: Quantum wave mixing with two-photon superposed states and sensing of quantum states. The mixing spectrum with the three-level atom consists of five peaks, which is a result of the mapping of two-photon state $|\gamma\rangle_-$ ($N_{ph} = 2$). Comparing with Fig. 4.9, an additional emission peak at $3\omega_+ - 2\omega_-$ appears, corresponding to two-photon emission from $|\gamma\rangle_-$. The absorption process resulting in a peak at $2\omega_- - \omega_+$ is now possible, as it is schematically exemplified. Importantly, the device probes the photonic states of the coherent field, distinguishing classical (Fig. 4.8(a)) ($N_{ph} = \infty$), one- ($N_{ph} = 1$), and two-photon ($N_{ph} = 2$) superposed states.

4.7 Theoretical description

Having presented the experimental results, we provide an in-depth derivation of the different regimes of wave mixing. My supervisor Prof. Oleg Astafiev developed the theory with contributions from fellow PhD student Aleksei Dimitriev and myself. As far as we are aware, this derivation has not been done before.

4.7.1 Continuous wave mixing on a single two-level atom

In chapter 2, section 2.5.5 we derived the elastic wave scattering amplitude on a two-level system under continuous drive at a single frequency. Similarly, we will obtain an expression for the elastic wave scattering amplitude on an artificial two-level atom under continuous drive at two frequencies.

We start with the Hamiltonian of a two-level atom interacting with two microwaves

$$H = -\frac{\hbar\omega_a}{2}\sigma_z - \hbar\Omega_-\sigma_x\cos(\omega t - \delta\omega t) - \hbar\Omega_+\sigma_x\cos(\omega t + \delta\omega t), \tag{4.12}$$

where Ω_+ and Ω_- are the amplitudes of the classical coherent driving fields. Under unitary transformation $H' = UHU^\dagger - i\hbar U\dot{U}^\dagger$ with $U = \exp(-\frac{\omega_a t}{2}\sigma_z)$ the Hamiltonian in the rotating wave approximation becomes

$$H' = \frac{\hbar\Delta\omega}{2}\sigma_z - \frac{\hbar}{2}\sigma_-(\Omega_- e^{-i\delta\omega t} + \Omega_+ e^{i\delta\omega t}) - \frac{\hbar}{2}\sigma_+(\Omega_- e^{i\delta\omega t} + \Omega_+ e^{-i\delta\omega t}), \tag{4.13}$$

where $\Delta\omega = \omega - \omega_a$. Solving the Master equation $-i(H'\rho - \rho H') + L = 0$ with $L = -\Gamma_1\sigma_z\rho_{11} - \Gamma_2(\sigma_+\rho_{10} + \sigma_-\rho_{01})$, we find

$$\rho_{01} = \frac{1}{2}\frac{\Gamma_1\Omega_-(\Delta\omega - i\Gamma_2)e^{-i\delta\omega t} + \Gamma_1\Omega_+(\Delta\omega - i\Gamma_2)e^{i\delta\omega t}}{\Gamma_1(\Delta\omega^2 + \Gamma_2^2) + \Gamma_2(\Omega_- + \Omega_+^2) + \Gamma_2\Omega_-\Omega_+(e^{i2\delta\omega t} + e^{-i\delta\omega t})}. \tag{4.14}$$

Recalling $\langle\sigma_-\rangle = \rho_{01}$, we rewrite the expectation value of the atomic σ_- operator

$$\langle\sigma_-\rangle = A\frac{\Omega_- e^{-i\delta\omega t} + \Omega_+ e^{i\delta\omega t}}{1 + \frac{\beta}{2}(e^{i2\delta\omega t} + e^{-i2\delta\omega t})}, \tag{4.15}$$

where

$$A = \frac{\Gamma_1\lambda}{2(\Gamma_1|\lambda|^2 + \Gamma_2(\Omega_-^2 + \Omega_+^2))}, \quad \beta = \frac{2\Gamma_2\Omega_-\Omega_+}{\Gamma_1|\lambda|^2 + \Gamma_2(\Omega_-^2 + \Omega_+^2)}, \tag{4.16}$$

with $\lambda = \Delta\omega - i\Gamma_2$. In general, if two waves with frequencies slightly detuned from each other $(\omega - \delta\omega, \omega + \delta\omega)$ propagate within the single quantum scatterer

($\Gamma_1 >> \delta\omega$), acting as a non-linear medium, we expect the waves to "mix" and peaks to appear. To find analytic expressions of the peaks, we need to find a series expansion of Eq. 4.15 and collect the frequency terms. Let $x = e^{i\delta\omega t}$, and expand the term

$$\begin{aligned}\frac{1}{1+\frac{\beta}{2}(x^2+x^{-2})} &= \sum_{k=0}^{\infty}\left(-\frac{\beta}{2}\right)^k (x^2+x^{-2})^k \\ &= \sum_{k=0}^{\infty}\left(-\frac{\beta}{2}\right)^k \sum_{m=0}^{k}\frac{k!}{(k-m)!m!}x^{2k-2m}x^{-2m} \\ &= \sum_{k=0}^{\infty}\left(\frac{\beta}{2}\right)^{2k}\sum_{m=0}^{2k}\frac{(2k)!}{(2k-m)!m!}(x^2)^{2k-2m} \\ &\quad -\sum_{k=0}^{\infty}\left(\frac{\beta}{2}\right)^{2k+1}\sum_{m=0}^{2k+1}\frac{(2k+1)!}{(2k-m)!m!}(x^2)^{2k-2m+1}.\end{aligned} \tag{4.17}$$

For even exponents $2p = 2k - 2m$ the first term of Eq. 4.17 simplifies to

$$\begin{aligned}&\sum_{k=0}^{\infty}\left(\frac{\beta}{2}\right)^{2k}\sum_{m=0}^{2k}\frac{(2k)!}{(2k-m)!m!}(x^2)^{2k+2m} \\ &\rightarrow \sum_{k=|p|}^{\infty}\left(\frac{\beta}{2}\right)^{2k}\frac{(2k)!}{(k+p)!(k-p)!}(x^2)^{2p} = \frac{1}{\alpha}y^{2|p|}x^{4p}\end{aligned} \tag{4.18}$$

where $\alpha = \sqrt{1-\beta^2}$ and $y = -\sqrt{\frac{1-\alpha}{1+\alpha}}$. For odd exponents $2p+1 = 2k+1-2m$ the second term of Eq. 4.17 simplifies to

$$\begin{aligned}&-\sum_{k=0}^{\infty}\left(\frac{\beta}{2}\right)\sum_{m=0}^{2k}\frac{(2k+1)!}{(2k+1-m)!m!}(x^2)^{2k+1+2m} \\ &\rightarrow \sum_{k=|p|}^{\infty}\left(\frac{\beta}{2}\right)^{2k+1}\frac{(2k+1)!}{(k+p+1)!(k-p)!}(x^2)^{2p+1} = \frac{1}{\alpha}y^{|2p+1|}x^{4p+2}.\end{aligned} \tag{4.19}$$

Combining even and odd cases we rewrite

$$\frac{1}{1+\frac{\beta}{2}(x^2+x^{-2})} = \frac{1}{\alpha}\sum_{p=-\infty}^{p=\infty} y^{|p|}x^{2p}. \tag{4.20}$$

Substituting Eq. 4.20 into the expectation value of the σ_- operator

$$\begin{aligned}
\langle\sigma_-\rangle &= \frac{A}{\alpha}(\Omega_- e^{-i\delta\omega t} + \Omega_+ e^{i\delta\omega t}) \sum_{p=-\infty}^{\infty} y^{|p|} e^{i2p\delta\omega t} \\
&= \frac{A}{\alpha}\left[\Omega_- \sum_{p=-\infty}^{\infty} y^{|p|} e^{i(2p-1)\delta\omega t} + \Omega_+ \sum_{p=-\infty}^{\infty} y^{|p|} e^{i(2p+1)\delta\omega t}\right] \\
&= \frac{A}{\alpha}\left[\Omega_- \sum_{p=-\infty}^{0} y^{-p} e^{i(2p-1)\delta\omega t} + \Omega_- \sum_{p=1}^{\infty} y^p e^{i(2p-1)\delta\omega t}\right. \\
&\quad \left. + \Omega_+ \sum_{p=-\infty}^{-1} y^{-p} e^{i(2p+1)\delta\omega t} + \Omega_+ \sum_{p=0}^{\infty} y^p e^{i(2p+1)\delta\omega t}\right] \\
&= \frac{A}{\alpha}\left[\Omega_- \sum_{p=0}^{\infty} y^p e^{i(-2p-1)\delta\omega t} + \Omega_- \sum_{p=0}^{\infty} y^{p+1} e^{i(2p+1)\delta\omega t}\right. \\
&\quad \left. + \Omega_+ \sum_{p=0}^{\infty} y^{p+1} e^{i(-2p-1)\delta\omega t} + \Omega_+ \sum_{p=0}^{\infty} y^p e^{i(2p+1)\delta\omega t}\right] \\
&= \frac{A}{\alpha} \sum_{p=0}^{\infty} y^p \left[(\Omega_- + y\Omega_+) e^{-(2p+1)\delta\omega t} + (y\Omega_- + \Omega_+) e^{i(2p+1)\delta\omega t}\right].
\end{aligned} \tag{4.21}$$

The corresponding emission amplitudes in Ω's are

$$\Omega^{em} = i\Gamma_1\langle\sigma_-\rangle = i\Gamma_1 \frac{A}{\alpha} \sum_{p=0}^{\infty} y^p \left[(\Omega_- + y\Omega_+) e^{-(2p+1)\delta\omega t} + (y\Omega_- + \Omega_+) e^{i(2p+1)\delta\omega t}\right] \tag{4.22}$$

Voltage amplitudes in case of capacitive coupling with dipole moment q_p, which couples voltage amplitude V and Ω according to $\hbar\Omega = q_p V$, are given by

$$V^{em} = \frac{i\hbar\Omega_1\langle\sigma_-\rangle}{q_p} = \frac{i\hbar\Gamma_1}{q_p}\frac{A}{\alpha} \sum_{p=0}^{\infty} y^p \left[(\Omega_- + y\Omega_+) e^{-(2p+1)\delta\omega t} + (y\Omega_- + \Omega_+) e^{i(2p+1)\delta\omega t}\right]. \tag{4.23}$$

The analytic expression for the intensity of each side spectral component is therefore given by

$$|V^{em}_{\pm(2p+1)}|^2 = \left(\frac{\hbar}{q_p}\frac{\Gamma_1 A}{\alpha} y^p (\Omega_\mp + y\Omega_\pm)\right)^2. \tag{4.24}$$

4.7.2 Elastic scattering of electromagnetic waves on an artificial atom

So far, in sec. 2.5.3.1, 4.7.1, we have described a two-level system interacting with a *classical* field or fields. Now, we consider a two-level atom with ground and excited states $|g\rangle$ and $|e\rangle$ and energy splitting $\sim \hbar\omega_0$, interacting with a *quantised* field at frequency ω with the Hamiltonian

$$H = i\hbar g(a^\dagger \sigma^- e^{i\delta\omega t} - a\sigma^+ e^{-i\delta\omega t}), \tag{4.25}$$

in the interaction picture, where $\sim g$ is the coupling energy, $\delta\omega = \omega - \omega_0$ is small detuning, $\sigma^+ = |e\rangle\langle g|$ ($\sigma^- = |g\rangle\langle e|$) is the rising (lowering) operator of the atomic states and $a^\dagger$ (a) is the creation (annihilation) operator of photon states $|n\rangle$ at frequency $\omega = \omega_0 + \delta\omega$ (n is an integer number larger than or equal to zero) [50, 96].

An evolution of the system in a short time interval $\Delta t \ll \delta\omega^{-1}$ is described by operator $U(t', t) = \exp(-\frac{i}{\hbar} H_t \Delta t)$, where H_t is the Hamiltonian at time t, $\Delta t = t' - t$. It can be expanded into an infinite series according to

$$U(t, t') = 1 + \eta(a^\dagger s^- - a s^+) - \frac{\eta^2}{2!}(aa^\dagger s_e + a^\dagger a s_g) - \frac{\eta^3}{3!}(a^\dagger a a^\dagger s^- - a a^\dagger a s^+) + ..., \tag{4.26}$$

where $\eta = g\delta t$ and $s^\pm$ are time dependent operators $s^+(t) = \sigma^+ e^{-i\delta\omega t}$ and $s^-(t) = \sigma^- e^{i\delta\omega t}$. The evolution operator can be simplified to

$$U(t, t') = \cos(\eta\sqrt{a^\dagger a}) s_g + \cos(\eta\sqrt{aa^\dagger}) s_e - \frac{a s^+}{\sqrt{a^\dagger a}} \sin(\eta\sqrt{a^\dagger a}) + \frac{a^\dagger s^-}{\sqrt{aa^\dagger}} \sin(\eta\sqrt{aa^\dagger}), \tag{4.27}$$

where $s_e = s^+ s^-$ and $s_g = s^- s^+$ and can be further rewritten as

$$\begin{aligned} U(t, t') = \sum_{n=0}^{\infty} \Big[& \cos(\eta\sqrt{n}) |n\rangle\langle n| s_g + \cos(\eta\sqrt{n+1}) |n\rangle\langle n| s_e \\ & - |n-1\rangle\langle n| s^+ \sin(\eta\sqrt{n}) + |n+1\rangle\langle n| s^- \sin(\eta\sqrt{n+1}) \Big]. \end{aligned} \tag{4.28}$$

Particularly for initial state $\Psi(t) = |g, n\rangle$, the evolution results in $\Psi(t') = \cos(\eta\sqrt{\eta})\,|g, n\rangle - e^{-i\delta\omega t}\sin(\eta\sqrt{n}\,|e, n-1\rangle$.

When $\Psi(t) = |g, \alpha\rangle$, the evolution is simplified to

$$\Psi(t') \approx \cos\frac{\theta}{2}\,|g, \alpha\rangle - e^{i\delta\omega t}\sin\frac{\theta}{2}\,|e, \alpha'\rangle\,, \tag{4.29}$$

where $\theta = 2\eta\alpha$, $\alpha = \sqrt{\langle n\rangle}$ and $|\alpha'\rangle = \left(1 - e^{-|\alpha|^2}\right)^{-1/2} \sum_{n=1}^{\infty} |n-1\rangle\,\langle n|\alpha\rangle$. It is interesting that for $\alpha \gg 1$, which happens under strong coherent radiation $|\alpha\rangle$, one photon absorption does not effectively change the state: $\alpha' \approx \alpha$. We can rewrite the state in Eq. 4.29 as $\Psi(t') \approx (\cos\frac{\theta}{2}\,|g\rangle - e^{-i\delta\omega t}\sin\frac{\theta}{2}\,|e\rangle) \otimes |\alpha\rangle$. After switching off the pulse, the photon states of the driving field collapse to zero ($|\alpha\rangle \to |0\rangle$) and the system state becomes

$$\Psi' = \left(\cos\frac{\theta}{2}\,|g\rangle - ie^{-i\delta\omega t}\sin\frac{\theta}{2}\,|e\rangle\right) \otimes |0\rangle \tag{4.30}$$

and

$$\langle s^+\rangle = -\frac{i}{2}\sin\theta. \tag{4.31}$$

The superposed system (at $\theta \neq M\pi$, where M is an integer number) acquires phase $\delta\omega t$ from the incident coherent wave [32, 64] and then generates a superposed single-photon state. It is instructive to analyse the evolution of Ψ' (from Eq. 4.30) under the operator from Eq. 4.28. When the accumulated angle $\eta = \pi/2$,

$$U_{ap} = |0\rangle\,\langle 0|\,\sigma^-\sigma^+ - ie^{i\delta\omega t}\,|1\rangle\,\langle 0|\,\sigma^- \tag{4.32}$$

and the atomic superpositions are converted into the superposition of a single-photon field at frequency ω according to

$$U_{ap}\left[\left(\cos\frac{\theta}{2}\,|g\rangle - ie^{-i\delta\omega t}\sin\frac{\theta}{2}\,|e\rangle\right) \otimes |0\rangle\right] = |g\rangle \otimes \left(\cos\frac{\theta}{2}\,|0\rangle - \sin\frac{\theta}{2}\,|1\rangle\right). \tag{4.33}$$

We introduce single-photon creation operator $b^+ = |1\rangle\,\langle 0|$ at frequency ω and

then

$$\langle b^+ \rangle = -\frac{1}{2}\sin\theta. \tag{4.34}$$

Equations (4.31 - 4.34) can now be rewritten using b-operators and the important consequence is that the atomic superposition is converted into the coherent single-photon field by substitution $s^+ \rightarrow ib^+$. In the more general case, the atomic coherence is mapped on the zero-one photon state according to $s^+ \rightarrow ib^+$ and $s^- \rightarrow -ib^-$, where $b^- = |0\rangle\langle 1|$.

The classical coherent and zero-one states can be represented in similar forms

$$\begin{aligned} |\alpha\rangle &= A\left(|0\rangle + \alpha|1\rangle + \frac{\alpha^2}{\sqrt{2!}} + ...\right) \\ |\beta\rangle &= B(|0\rangle + \beta|1\rangle) \end{aligned} \tag{4.35}$$

where $A = \exp(-|\alpha|^2/2)$ and $B = (1+|\beta|^2)^{-1/2}$. Particularly for the coherent photon state in Eq. 4.33, $\beta = -\tan\theta/2$ and $B = \cos\theta/2$.

The Hamiltonian of Eq. 4.25 can be equivalently rewritten through the single-photon creation/annihilation operators as

$$H = i\hbar g(b^+ a - b^- a^\dagger), \tag{4.36}$$

meaning that b-operators describe atomic excitations with phase $\delta\omega t$ and. therefore, satisfy identities similar to s-operators: $b^+b^- = |1\rangle\langle 1|$, $b^-b^+ = |0\rangle\langle 0|$, $b^+b^+ = 0$, $b^-b^- = 0$.

We can simplify Eq. 4.28 for the case of strong coherent drive as

$$U(t,t') \approx \cos(\eta\sqrt{a^\dagger a}) + (ab^+ - a^\dagger b^-)\frac{\sin(\eta\sqrt{a^\dagger a})}{\sqrt{a^\dagger a}}. \tag{4.37}$$

4.7.3 Elastic scattering of two frequencies

Now we will discuss an atom driven by two different frequency waves ($\omega_\pm = \omega_0 \pm \delta\omega$). For this case we can calculate the spectra within our semiclas-

sical approach, using Eqs. 4.29, 4.30. Substituting classical driving field $\theta = \Omega\Delta t e^{i\delta\omega t} + \Omega\Delta t e^{-i\delta\omega t} = 2\Omega\Delta t \cos\delta\omega t$ into Eq. 4.31, we obtain

$$\langle s^+ \rangle = -\frac{1}{2}\sin(2\Omega\Delta t \cos\delta\omega t), \tag{4.38}$$

which is decoupled in Bessel function series according to

$$\langle s^+ \rangle = -\sum_{k=-\infty}^{\infty} (-1)^k J_{2k+1}(2\Omega\Delta t)\cos[(2k+1)\delta\omega t], \tag{4.39}$$

and, therefore, calculating the spectral component $\langle s^+_{2k+1} \rangle$ of the emission at frequency $(2k+1)\delta\omega t$ gives

$$\langle s^+_{2k+1} \rangle = \frac{(-1)^k}{2} J_{2k+1}(2\Omega t) e^{i(2k+1)\delta\omega t}. \tag{4.40}$$

Despite the simplicity of the above derivation, it does not illustrate the physical entity of QWM, in particular, it fails to separate individual contributions of multi-photon processes into emission and therefore does not illustrate the link to photon statistics of the emitted light. Moreover, the semiclassical picture fails to explain the limited number of spectral components we observe for the case of quantum mixing with delayed pulses. Therefore, for our purposes it is instructive to calculate the same physical quantity from an approach of second quantisation.

For this approach, we now take the two continuous coherent driving fields $|\alpha_-\rangle_-$ and $|\alpha_+\rangle_+$ into account, where $\alpha_\pm$ are real amplitudes for simplicity. The Hamiltonian is then modified to

$$H = i\hbar g(s^-_- a^\dagger_- - s^+_- a_- + s^-_+ a^\dagger_+ + s^+_+ a_+), \tag{4.41}$$

where $a^\dagger_\pm$ ($a_\pm$) is the creation (annihilation) operator of a photon at $\omega_\pm$, $s^+_\pm$ ($s^-_\pm$) is time-dependent rising (lowering) operator of the atomic states such that $s^+_\pm = \sigma^+ e^{\mp i\delta\omega t}$ ($s^-_\pm = \sigma^- e^{\pm i\delta\omega t}$), and $\hbar g$ is the coupling energy to the

modes. The evolution operator of the Hamiltonian of Eq. 4.41 can be expanded similarly to Eq. 4.28, however, each term contains sequential combinations of operators $s_{\pm}^{-}a_{\pm}^{\dagger}$ and $s_{\pm}^{+}a_{\pm}$. We can rewrite the Hamiltonian through the b-operators, using substitution $s_{\pm}^{+} \to b_{\pm}^{+}$ and $s_{\pm}^{-} \to b_{\pm}^{-}$,

$$H = i\hbar g(b_{-}^{+}a_{-} - b_{-}^{-}a_{-}^{\dagger} + b_{+}^{+}a_{+} - b_{+}^{-}a_{+}^{\dagger}), \tag{4.42}$$

where $b_{\pm}^{\pm}$ describe atomic excitation/relaxation with phases $\pm\delta\omega t$. The evolution operator $U(t',t) = \exp(-\frac{i}{\hbar}H_t\Delta t)$ can be rewritten in the tensor form

$$\begin{aligned} U =& 1 + \eta(b_m^- a_m^\dagger - b_m^+ a_m) - \frac{\eta^2}{2!}(b_m^+ b_j^- a_m a_m^\dagger a_j) \\ &- \frac{\eta^3}{3!}(b_{m-j+p}^- a_m^\dagger a_j a_p^\dagger - b_{m-j+p}^\dagger a_m a_j^\dagger a_p) + ..., \end{aligned} \tag{4.43}$$

where indexes take values ± 1. Here, we rely on $b_m^+ b_j^- b_p^+ = b_{m-j+p}^+$ because b-operators should satisfy the same relations as s-operators: $s_m^+ s_j^- s_p^+ = e^{-im\delta\omega t}\sigma^+ e^{ij\delta\omega t}\sigma^- e^{-ip\delta\omega t}\sigma^+ = e^{-i(m-j+p)\delta\omega t}\sigma^+ = s_{m-j+p}^+$. Here we expanded the definition of s-operators to an arbitrary l-mode according to $s_l^{\pm} = e^{\mp il\delta\omega t}\sigma^{\pm}$. This, for example, means that the third order terms $a_+ a_-^\dagger a_+ b_3^+$ and $a_- a_+^\dagger a_- b_{-3}^+$ result in creation of the single-photon fields at frequency $\omega_{\pm 3} = \omega_0 \pm 3\delta\omega$.

In general, the output light could be generated at frequencies $\omega_{\pm l} = \omega_0 \pm l\delta\omega$, where $l = 2k+1$, $k = 0, 1, 2, ...$ Among all terms in Eq. 4.43 contributing into creation of the single-photon field at $\omega_{\pm l}$, the one of lowest order consists of $2k+2$ operators: $2k+1$ a-operators $a_{\pm}a_{\mp}^{\dagger}a_{\pm}... = (a_{\pm}a_{\mp}^{\dagger})^k a_{\pm}$ and one $b_{\pm(2k+1)}^{+}$. As it was shown in [32], the superposed atom generates a coherent field $V = \frac{\hbar\Gamma_1}{q_p}\langle s^+\rangle$. Generalising the statement, we can write the expression for the single-photon coherent field generated at frequency $\omega_{\pm l}$:

$$V_{\pm l} = \frac{\hbar\Gamma_1}{q_p}\langle b_{\pm l}^{+}\rangle, \tag{4.44}$$

where q_p is the dipole coupling moment for our case of capacitive coupling of the atom to the transmission line. In order to analyse the evolution, we

start from initial state $\Psi(t) = |\beta\rangle \otimes |n\rangle_- \otimes |n\rangle_+$ consisting of the atom in the superposition described by single-photon coherent state $|\beta\rangle$, and photon states $|n\rangle_\pm$ (where $n \gg 1$) with equal number of photons in both frequency modes. We introduce the following operators

$$\begin{aligned} \hat{A}^{+-}_{2k} &= \begin{cases} (a^\dagger_- a_+)^{-k} & : k < 0 \\ (a^\dagger_+ a_-)^{k} & : k \geq 0 \end{cases} \qquad \hat{A}^{-}_{2k+1} = \begin{cases} (a_- a^\dagger_+)^{-k} a_- & : k < 0 \\ (a_+ a^\dagger_-)^{k} a_+ & : k \geq 0 \end{cases} \\ \hat{A}^{-+}_{2k} &= \begin{cases} (a_- a^\dagger_+)^{-k} & : k < 0 \\ (a_+ a^\dagger_-)^{k} & : k \geq 0 \end{cases} \qquad \hat{A}^{-}_{2k+1} = \begin{cases} (a_- a^\dagger_+)^{-k} a_- & : k < 0 \\ (a_+ a^\dagger_-)^{k} a_+ & : k \geq 0 \end{cases} \end{aligned} \tag{4.45}$$

which satisfy relations $(\hat{A}^{+})^\dagger_{2k+1} = \hat{A}^{-}_{2k+1}$, $(\hat{A}^{+-}_{2k})^\dagger = \hat{A}^{+-}_{-2k}$, $(\hat{A}^{-+}_{2k})^\dagger = \hat{A}^{-+}_{2k}$. The operator

$$\hat{A}^{-}_{2k+1} b^{+}_{2k+1} \tag{4.46}$$

creates a single photon at ω_{2k+1} with the least number of photons created/annihilated at driving frequencies $\omega_\pm$. Particularly, $A^{-}_{2k+1} |n_-, n_+\rangle = \left(\frac{9n_-+k)!}{n_-!} \frac{n_+!}{(n_+-k-1)!}\right)^{\frac{1}{2}}$, when $k > 0$. . In the discussed case of large and equal photon number $n \gg 2k+1$, $A^{-}_{2k+1} |n, n\rangle \approx n^{k+\frac{1}{2}} |n+k, n-k-1\rangle$. The evolution can be simplified to

$$\begin{aligned} U(t', t)\Psi(t) \approx \sum_{k=-\infty}^{\infty} [&\hat{A}^{+-}_{2k} C^{+}_{2k} b^{-}_{k} b^{+}_{-k} + \hat{A}^{-+}_{2k} C^{-+}_{2k} b^{+}_{k} b^{-}_{-k} - \\ &\hat{A}^{-}_{2k+1} C^{-}_{2k+1} b^{+}_{2k+1} + \hat{A}_{2k+1} C^{+}_{2k+1} b^{-}_{2k+1}] \Psi(t), \end{aligned} \tag{4.47}$$

where coefficients C_l depend on the initial state and come from a sum of all possible permutations of combinations of creation-annihilation operators ($a_- a^\dagger_-$, $a^\dagger_- a_-$, $a^\dagger_+ a_+$, $a_+ a^\dagger_+$ for two virtual photons involved, $a_+ a^\dagger_- a_- a^\dagger_+$, $a^\dagger_+ a_- a^\dagger_- a_+$ and two more terms for four virtual photons involved and so on), which do not change neither the occupation nor the frequency of photonic states. Assuming

that $n \ll 2k$ and using the relations $a\,|n\rangle = n\,|n\rangle$, $a^\dagger\,|n\rangle \approx n\,|n\rangle$ we arrive at

$$C_l \approx \frac{1}{(\sqrt{n})^l}\sum_{m=0}^{\infty}\frac{(-1)^{j+m}(\eta\sqrt{n})^{l+2m}}{(l+2m)!}\frac{(l+2m)!}{m!(l+m)!} = \frac{(-1)^j}{(\sqrt{n})^l}J_l(\eta\sqrt{n}), \tag{4.48}$$

where $j = \mod(l,2)$, J_l is the Bessel function of the first kind.

If the initial state $\Psi = |\beta,\alpha,\alpha\rangle$, where α is a real number, Eq. 4.47 is simplified to

$$\begin{aligned}\sum_{k=-\infty}^{\infty} =& \Bigg[\frac{(-1)^k}{\alpha^{2k}}J_{2k}(\theta)\left(\hat{A}^{+-}_{2k}b^-_{-k}b^+_k + \hat{A}^{-+}_{2k}b^+_{-k}b^-_k\right)\\ &+ \frac{(-1)^k}{\alpha^{2k+1}}J_{2k+1}(\theta)\left(\hat{A}^+_{2k+1}b^-_{2k+1} - \hat{A}^-_{2k+1} - \hat{A}^-_{2k+1}b^+_{2k+1}\right)\Bigg]\Psi,\end{aligned} \tag{4.49}$$

and in the case of $\Psi = |0,\alpha,\alpha\rangle$

$$\begin{aligned}U\Psi \approx \sum_{k=-\infty}^{\infty}\Bigg[&\frac{(-1)^k}{\alpha^{2k}}J_{2k}(\theta)\hat{A}^{+-}_{2k}\,|0\rangle_{2k}\otimes|\alpha,\alpha\rangle\\ &+\frac{(-1)^k}{\alpha^{2k+1}}J_{2k+1}(\theta)\,|1\rangle_{2k+1}\otimes|\alpha,\alpha\rangle\Bigg],\end{aligned} \tag{4.50}$$

where $\theta = 2\eta\alpha$. Taking into account that $b^+_{2k+1} = |1\rangle_{2(k+p)+1}\langle 0|_{2p}$, we can directly write an expression for the expectation value of the single-photon creation operator at ω_{2k+1},

$$\langle b^+_{2k+1}\rangle = \sum_{p=-\infty}^{\infty}\frac{(-1)^{k+p+p}}{\alpha^{2(k+p)+1}}J_{2(k+p)+1}(\theta)J_{2p}(\theta)\,\langle\hat{A}^-_{2(k+p)+1}\hat{A}^{+-}_{-2p}\rangle\,. \tag{4.51}$$

Using standard textbook formulae for Bessel functions, it is simplified to

$$\langle b^+_{2k+1}\rangle = \frac{(-1)^k J_{2k+1}(2\theta)}{2\alpha^{2k+1}}\,\langle\hat{A}^-_{2k+1}\rangle\,. \tag{4.52}$$

Here we use the following property: $\alpha^{-(2(k+p)+1)}\,\langle\hat{A}^-_{2(k+p)+1}\hat{A}^{+-}_{-2p}\rangle \approx \alpha^{-(2k+1)}\,\langle\hat{A}^-_{2k+1}\rangle$ for $\alpha \gg 1$. Taking into account that $\langle\hat{A}^-_{2k+1}\rangle \approx \alpha^{2k+1}$,

we simplify the expression further to

$$\langle b^{+}_{2k+1} \rangle = \frac{(-1)^k}{2} J_{2k+1}(2\Omega\Delta t), \tag{4.53}$$

where $\Omega\Delta t = \theta$. The final expression is identical to Eq. 4.40. The coherent emission amplitude at each mode is

$$V_{2k+1} = \frac{\hbar\Gamma_1}{q_p} \langle b_{2k+1} \rangle , \tag{4.54}$$

and power

$$W_{2k+1} = \frac{V^2_{2k+1}}{2Z_0}, \tag{4.55}$$

where Z_0 is the line impedance. We calculate the coherent wave energy at each cycle, substituting Eq. 4.53 into Eq. 4.44 and integrating over time t. Taking into account that $\Gamma_1 = \frac{\hbar\omega q_p^2 Z_0}{\hbar^2}$ and $\int_0^\infty \langle b^2_{2k+1} \rangle \, dt = \int_0^\infty e^{-\Gamma_1 t} dt = \Gamma_1^{-1}$, we find the generated photon number in two directions to be

$$\frac{E_{\pm(2k+1)}}{\hbar\omega} = \frac{J^2_{\pm(2k+1)}(2\Omega\Delta t)}{4}. \tag{4.56}$$

Although we have found the analytical solution for the approximated case of strong drive, it can be generalised for any arbitrary initial driving states as

$$\langle b^{+}_{2k+1} \rangle = D^{-}_{2k+1} \langle \hat{A}^{-}_{2k+1} \rangle , \tag{4.57}$$

where D^{-}_{2k+1} is a coefficient dependent on the driving amplitudes. This means that only states at frequency $\omega_0 \pm (2k+1)\delta\omega$ with odd indexes $2k+1 > 0$ can be created. Creation of the single-photon state, requires annihilation of $k+1$ photons at at ω_+ and creation of k photons at ω_-.

4.7.4 Quantum mixing

We consider an evolution from two sequential pulses with frequencies ω_- and ω_+ as illustrated in Fig 4.11(a). The first pulse results in the atomic excitation described by the single-photon field $|\beta\rangle_-$, which comes from process

$|\beta_-, \alpha, \alpha\rangle = B_-\left(1 + \beta_- \frac{b_-^+ a_-}{\alpha_-}\right)|0, \alpha_-, \alpha_+\rangle$, where $B_- = \sqrt{1+\beta_-^2}$. The state is then interacting with coherent state $|\alpha\rangle_+$ of the second pulse (Fig. 4.11(b)).

Among all processes of the third and higher orders, the only non-trivial one, leading to creation of the new frequency mode, is described by $A_3^- b_3^+ = a_+ a_-^\dagger a_+ b_3^+ = a_+ b_+^+ a_-^\dagger b_-^- a_+ b_+^+$ because at most one photon is emitted from $|\beta\rangle_-$ at ω_-. All other processes are prohibited due to lack of photons at ω_-. It results in creation of the single-photon state at $2\omega_+ - \omega_- = \omega_0 + 3\delta\omega$ as schematically shown in Fig. 4.11(c).

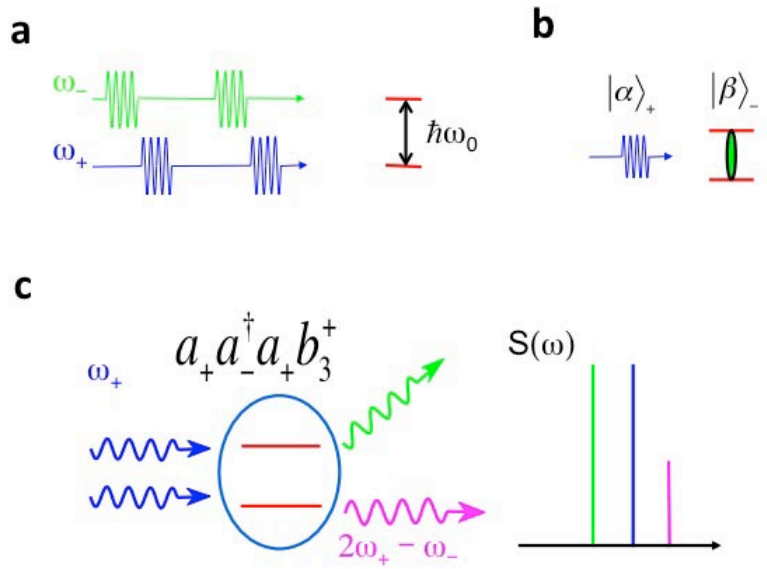

Figure 4.11: a) Pulse sequence b) The first pulse prepares the coherent single-photon state $|\beta\rangle_-$ which interacts with the coherent state $|\alpha\rangle_+$ of the second pulse. c) Schematic presentation of the only non-trivial high order process resulting in a peak at $\omega_0 + 3\delta\omega$.

The evolution is described as

$$\begin{aligned} U(t', t)\,|0, \alpha_-, \alpha_+\rangle \approx & B_+\left(1 + \beta_+ + \frac{a + b_+^+ - a_+^\dagger b_+^-}{\sqrt{a_+^\dagger a_+}}\right) \\ & \times B_-\left(1 + \beta_- \frac{a_- b_-^+}{\sqrt{a_-^\dagger a_-}}\right)|0, \alpha_-, \alpha_+\rangle\,, \end{aligned} \tag{4.58}$$

where operators $\beta_\pm = \tan(\theta_\pm/2)$, $B_\pm = \sqrt{1+\beta_\pm^2}$, $\theta_- = 2g_-\alpha_-(t'-t)$, $\theta_+ =$

$2g_-\alpha_-(t''-t')$. The equation is further simplified to

$$U(t',t'')\,|0,\alpha_-,\alpha_+\rangle \approx B_+B_-\left(1-\hat{\beta}_+^-\hat{\beta}_-^+ + \hat{\beta}_+^+ + \hat{\beta}_-^+\right)|0,\alpha_-,\alpha_+\rangle\,, \qquad (4.59)$$

where operators $\hat{\beta}_\pm^+ = \beta_\pm a_\pm b_\pm^+ (a_\pm^\dagger a_\pm)^{-1/2}$ and $\hat{\beta}_\pm^- = (\hat{\beta}_\pm^+)^\dagger$. Among all possible operators of Eq. 4.46 of orders higher or equal to three, only $A_3^- b_3^+$ creates the new frequency field because only

$$\langle A_3^- b_3^+\rangle = B_+^2 B_- \langle 0,\alpha_-,\alpha_+|\,\hat{\beta}_+^- a_+ a_-^\dagger a_+ b_3^+ \hat{\beta}_+^- \hat{\beta}_-^+\,|0,\alpha_-,\alpha_+\rangle \qquad (4.60)$$

is non-zero. And we find

$$\langle b_3^+\rangle = B_+^2 B_- \beta_+^2 \beta_-. \qquad (4.61)$$

Finally, the field amplitude is found to be

$$\langle b_3^+\rangle \approx \sin^2[\Omega_+(t''-t')]\sin[\Omega_-(t'-t)], \qquad (4.62)$$

where $\Omega_\pm = g\alpha_\pm$.

4.7.5 Two-photon quantum mixing

In the case of an equally spaced three-level system described by $|0\rangle$, $|1\rangle$ and $|2\rangle$, with transition energies $\sim \omega_{10} =\sim \omega_{21}$, the resonance drive results in excitation of the system, leading to state $\Psi = C(|0\rangle + \gamma_1\,|1\rangle + \gamma_2\,|2\rangle)$, where $C = \left[1+|\gamma_1|^2+|\gamma_2|^2\right]^{-1/2}$.

We introduce two-state creation/annihilation operators $c^\dagger$, c with the following properties: $c^\dagger\,|0\rangle = |1\rangle$, $c^\dagger\,|1\rangle = |2\rangle$, $c^\dagger\,|2\rangle = 0$, $c\,|2\rangle = |1\rangle$, $c\,|1\rangle = |0\rangle$, $c\,|0\rangle = 0$. In the case of the same pulse sequence the first pulse applied at ω_- during time $[t',t]$ is followed by another pulse ω_+ during $[t'',t']$ (Fig. 4.12(b).

Similarly to Eq. 4.59, the evolution is presented as

$$U(t'',t) = C_+\left[1+\hat{\gamma}_+^\dagger+\hat{\gamma}_+ + \hat{\gamma}_{2+}^\dagger + \hat{\gamma}_{2+}\right] \times C_-\left[1+\hat{\gamma}_-^\dagger + \hat{\gamma}_{2-}^\dagger\right], \qquad (4.63)$$

where $\hat{\gamma}^{\dagger}_{1\pm} = \gamma^{+}_{1\pm} a_{\pm} c^{\dagger}_{\pm}$, $\hat{\gamma}^{+}_{1\pm} = \gamma^{-}_{1\pm} a^{\dagger}_{\pm} c_{\pm}$, $\hat{\gamma}^{\dagger}_{2\pm} = \gamma^{+}_{2\pm} (a_{\pm} c^{\dagger}_{\pm})^2$, $\hat{\gamma}^{+}_{2\pm} = \gamma^{-}_{2\pm} (a^{\dagger}_{\pm} c_{\pm})^2$.

$$U(t'',t) = C_+ C_- \Big[1 + \hat{\gamma}^{\dagger}_{+} + \hat{\gamma}_{+} + \hat{\gamma}^{\dagger}_{-} + \hat{\gamma}^{\dagger}_{2+} + \hat{\gamma}_{2+} + \hat{\gamma}^{\dagger}_{2-} + \hat{\gamma}^{\dagger}_{+}\hat{\gamma}^{\dagger}_{-} + \hat{\gamma}_{+}\hat{\gamma}^{\dagger}_{-} + \hat{\gamma}_{+}\hat{\gamma}^{\dagger}_{2-} + \hat{\gamma}_{2+}\hat{\gamma}^{\dagger}_{2-}\Big]. \tag{4.64}$$

As an example, some terms contributing into the peaks, additionally to the single-photon wave mixing, are

$$\begin{aligned} 3\omega_+ - 2\omega_- : \quad & \langle \hat{\gamma}^{\dagger}_{+} A^{-}_{5} c^{+}_{5} (\hat{\gamma}_{2+}\hat{\gamma}^{\dagger}_{2-})^{\dagger} \rangle = \langle \hat{\gamma}^{\dagger}_{+} A^{-}_{5} c^{+}_{5} \hat{\gamma}_{2-} \hat{\gamma}^{\dagger}_{2+} \rangle \quad \rightarrow \langle a_+ a^{\dagger}_{-} a^{\dagger}_{-} a_+ a_+ \rangle \\ 2\omega_- - \omega_+ : \quad & \langle \hat{\gamma}^{\dagger}_{2-} A^{-}_{3} c^{+}_{-3} (\hat{\gamma}_{+})^{\dagger} \rangle \quad \rightarrow \langle a_- a_- a^{\dagger}_{+} \rangle \end{aligned} \tag{4.65}$$

where the former is schematically shown in Fig. 4.12(d).

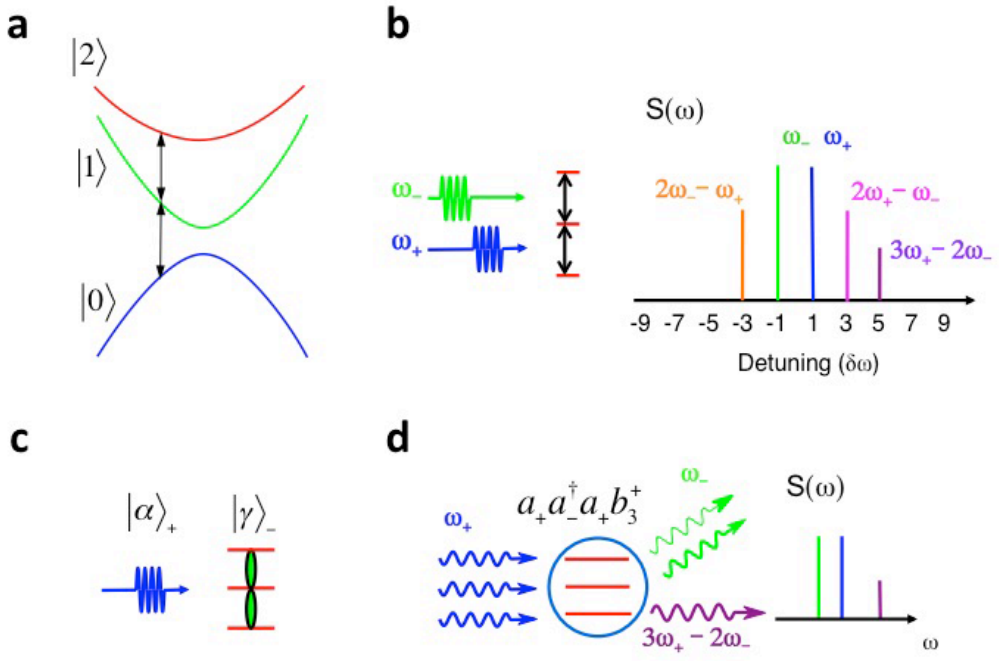

Figure 4.12: a) The system can be tuned to a working point where the transition from the ground state to the first excited state and from the first excited state to the ground state are equal and other energies are far away. b) We consider two sequential pulses at frequencies ω_- and ω_+ interacting with the equally spaced three-level atom resulting in the spectrum exhibiting five peaks. c) The first pulse prepares the coherent two-photon state $|\gamma\rangle_-$ which interacts with the coherent state $|\alpha\rangle_+$ of the second pulse. d) Schematic of the physical process resulting in a peak at $3\omega_+ - 2\omega_-$.

4.8 Conclusion

According to our understanding, QWM has not been demonstrated in systems other than superconducting quantum ones due to the following reasons. First, the effect requires a single quantum system because individual interaction processes have to be separated in time [97] and it will be washed out in multiple scattering on an atomic ensemble in matter. Next, although photon counters easily detect single photons, in the visible optical range, it might be more challenging to detect amplitudes and phases of weak power waves [98, 99]. On the other hand, microwave techniques allow one to amplify and measure weak coherent emission from a single quantum system [64, 100], due to strong coupling of the single artificial atom; the confinement of the radiation in the transmission line; and due to an extremely high phase stability of microwave sources. The radiation can be selectively detected by either spectrum analysers or vector network analysers with narrow frequency bandwidths, efficiently rejecting the background noise.

To conclude, we have demonstrated wave mixing on a single artificial atom (Fig. 4.13(a)) and QWM (Fig. 4.13(b-d)) - interesting phenomena of quantum optics.

We consider the time evolution of a two-level system illuminated by two microwaves with frequencies $\omega_{\pm} = \omega_0 \pm \delta\omega$, where ω_0 is the transition frequency of the atom and the detuning $\delta\omega$ is much smaller than the atom's relaxation rate Γ_1, which can be written as a series expansion with each term describing a multi-photon process. What's important is that each term in the expansion consists of pairs of annihilation (creation) a ($a^{\dagger}$) operators of the driving field and creation (annihilation) b^{+} (b^{-}) operators of the single photon field, i.e. sequential absorption (emission) accompanied by atomic excitations (relaxations) thus conserving energy.

We have explored different regimes of QWM and proved that the superposed and coherent states of light are mapped into a quantised spectrum of narrow peaks. The number of peaks is determined by the number of interacting

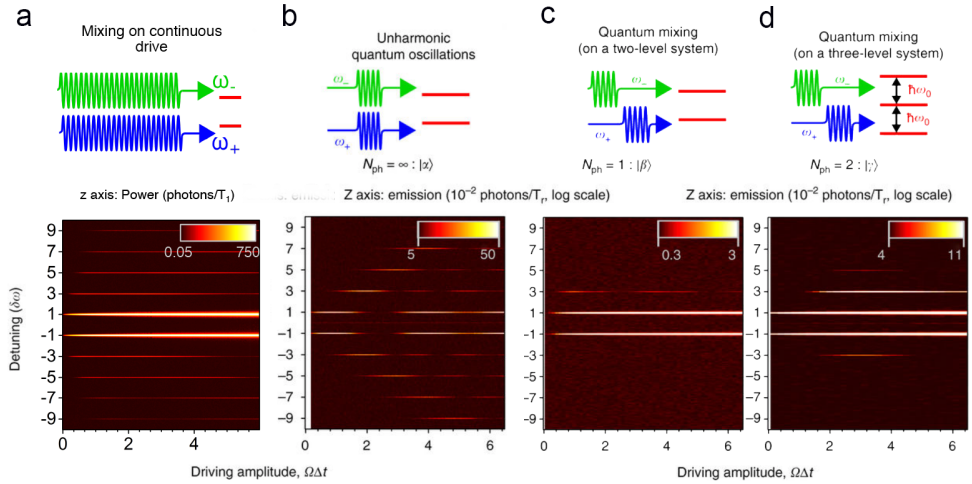

Figure 4.13: Different regimes of mixing and dynamics of photonic states. (a) Coherent wave mixing on a single artificial atom in the continuous driving regime. (b) Anharmonic Rabi oscillations in classical wave mixing on a single artificial atom. (c) Quantum wave mixing with a two-level atom. The single emission side peak appears. (d) Quantum wave mixing on a three-level atom. Two more side peaks at $3\omega_+ - 2\omega_-$ and $2\omega_- - \omega_+$ appear because the two-photon field is stored in the atom at ω_-.

photons. As the number of required photons increases with order k, the emission peaks take longer to appear. For continuous drives we observe many order peaks at frequencies $\omega_0 \pm (2k+1)\delta\omega$ (Fig. 4.13(a)). Pulsing the two coherent drives results in the emission peaks oscillating according to Bessel functions of their order (Fig. 4.13(b)). Introducing a time-delay between pulses leads to an asymmetric spectrum (Fig. 4.13(c-d)). The first pulse prepares the atom in a superposed state, or in other words stores the coherent single photon field, which subsequently interacts with the second pulse. The asymmetry arises from the two-level atom only being able to provide one photon at most that can mix with the coherent photon field. As seen in Fig. 4.13(c), if the first pulse is at frequency ω_- the only allowed higher order peak is at $2\omega_+ - \omega_-$. There is no peak at $2\omega_- - \omega_+$ as this would require two photons from the two-level atom. However, extending the experiment to a three-level atom with equally spaced transition frequencies causes two additional side peaks to appear (Fig. 4.13(d)), amounting to five peaks in the spectrum. Now, the two-photon state interacts

with the coherent photon field provided by the second pulse.

Thus, QWM can probe photonic states and could serve as a powerful tool for building new types of on-chip quantum electronics.

Chapter 5

Mixing of coherent waves on a single three-level artificial atom

We report coherent frequency conversion in the gigahertz range via three-wave mixing on a single artificial atom in open space. All frequencies involved are in vicinity of transition frequencies of the three-level atom. A cyclic configuration of levels is therefore essential, which we have realised with an artificial atom based on the flux qubit geometry. The atom is continuously driven at two transition frequencies and we directly measure the coherent emission at the sum or difference frequency. Our approach enables coherent conversion of the incoming fields into the coherent emission at a designed frequency in prospective devices of quantum electronics.

5.1 Introduction

For a long time research in experimental quantum optics focused on studying ensembles of natural atoms [101, 30]. However, there have been huge advances in performing analogous quantum optics experiments using other systems [102, 103, 104]. In particular, superconducting artificial atoms are remarkably attractive to study quantum optics phenomena. The artificial atoms are nano-scale electronic circuits that can be fabricated using well established techniques and can therefore be easily scaled up to larger systems. Their energy levels can be engineered as desired, and strong coupling can be achieved

with resonators and transmission lines [85, 105, 32, 90].

This greater control of parameters allows one to reproduce quantum optics phenomena with improved clarity or even reach regimes, that are unattainable with natural atoms. For instance coherent population trapping [106], electromagnetically induced transparency [107, 108], Autlers-Townes splitting [109, 53, 110, 111, 112], and quantum wave mixing [1] have been experimentally observed in superconducting three-level systems [113, 114, 115, 116, 117]. Moreover, three-level atoms can be used to cool quantum systems [118, 119], amplify microwave signals [87] and generate single or entangled pairs of photons [120] – important applications for future quantum networks.

Here we investigate three-wave mixing, a nonlinear optical effect that can occur in cyclic three-level atoms, which are lacking in nature [121], but can easily be realised with superconducting artificial atoms. The only suitable natural systems for the three-wave mixing are chiral molecular three-level systems without inversion symmetry [122]. However, these systems cannot be tuned in frequency.

Different to Josephson junction based parametric three-wave mixing devices [123], that rely on mixing on a classical non-linearity, we implement here another method to generate three-wave mixing using a single cyclic or Δ-type artificial atom. This was considered theoretically in references [121, 124].

We directly measure the coherent emission of the cyclic three-level atom under two external drives corresponding to two atomic transitions. The emission occurs at a single mixed frequency (sum or difference). This emission is a corollary of coherent frequency conversion but inherently differs from classical frequency conversion [7, 50] which would result in sidebands at the sum and difference frequencies.

Previously, coherent atomic excitations using two frequencies have been studied in a single dc-SQUID phase qubit circuit with two internal degrees of freedom [125]. However, in this work, we realise coherent frequency conversion with a cyclic artificial atom in open space, which offers some advantages over

placing it in a cavity. In particular, it allows to directly detect the coherent (elastic) component of the emitted field at sum or difference frequencies of the artificial atom by a vector network analyser (VNA) [64].

This work establishes innovative quantum electronics that enables three-wave mixing, and coherent frequency conversion.

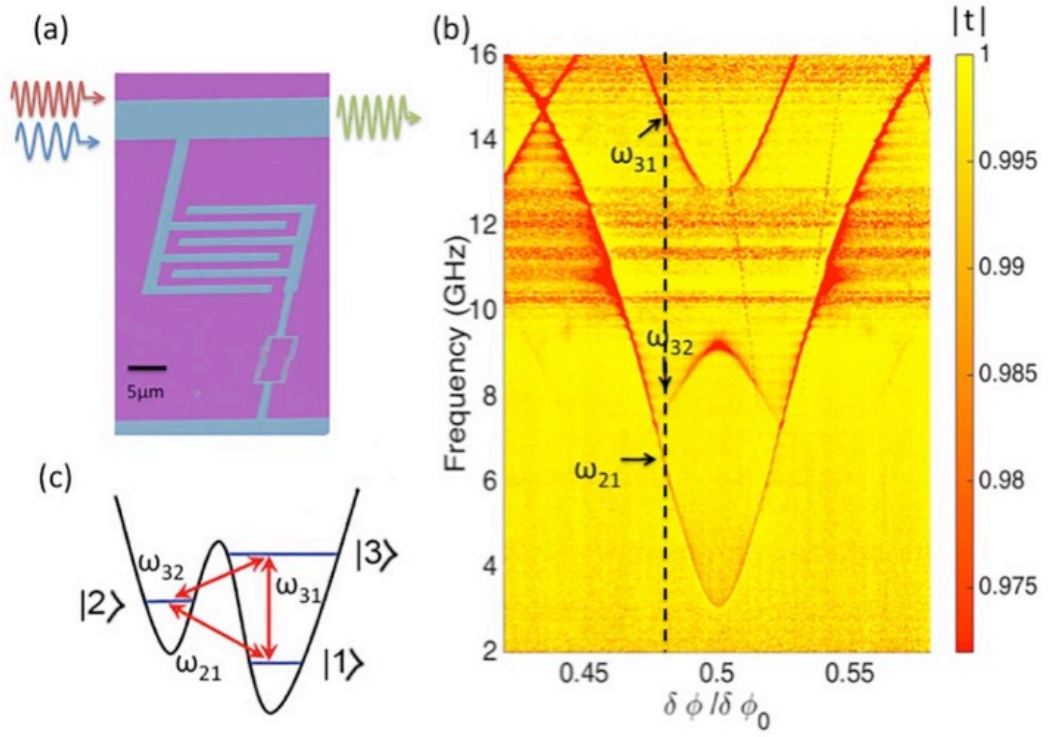

Figure 5.1: (a) False-coloured micrograph of the device taken at an angle. The three-level artificial atom consisting of a superconducting loop with four Josephson junctions is capacitatively coupled to the transmission line. (b) Spectroscopy of the single artificial three-level atom. The transition frequencies are detected by transmission as a function of flux bias and probe driving frequency. Choosing a working point away from the degeneracy point $\delta\Phi \neq 0$ indicated by the dashed line in (b) results in (c) a cyclic-type artificial atom with transition frequencies $\omega_{21}/2\pi = 6.48$ GHz, $\omega_{32}/2\pi = 8.35$ GHz, and $\omega_{31}/2\pi = 14.83$ GHz.

5.2 Sample description

Our device consists of a superconducting loop ($\sim 10\mu m^2$) interrupted by four Josephson junctions. This geometry is based on the flux qubit [126] where one of the Josephson junctions, the α-junction, has a reduced geometrical overlap

by a factor of α. It is capacitatively coupled to a 1D transmission line via an interdigitated capacitance of $C = 5$ fF (see Fig 5.1(a)). The device parameters (Josephson energy $E_J/h = 65$ GHz, charging energy ($E_C = e^2/2C$) $E_C/h = 19$ GHz, and $\alpha = 0.45$) have been chosen such that the three lowest transition frequencies fall into the frequency measurement band of our experimental setup. The coupling to the transmission line is strong enough to suppress non-radiative atom relaxation and hence the majority of photons from the atom are emitted into the transmission line.

The device was fabricated by means of electron-beam lithography and shadow evaporation technique with controllable oxidation. For a detailed description of the fabrication process refer to sec. 3.2.

The transition frequencies, ω_{12}, ω_{23}, and ω_{13} are controlled by the external magnetic flux threaded through the loop, $\Phi = \Phi_0/2 + \delta\Phi$, where Φ_0 is the flux quantum and $\delta\Phi$ is the detuning from the energy degeneracy point of the artificial atom. The atomic transition energies are found by performing transmission spectroscopy. We sweep the frequency of a probe microwave against the flux bias $\delta\Phi$, as seen in Fig. 5.1(b). The working point is set away from the degeneracy point $\delta\Phi \neq 0$, where all transitions are allowed, forming a cyclic or Δ-type atom with transition frequencies $\omega_{21}/2\pi = 6.48$ GHz, $\omega_{32}/2\pi = 8.35$ GHz, and $\omega_{31}/2\pi = 14.83$ GHz ($\omega_{31} = \omega_{21} + \omega_{32}$), as schematically shown in Fig. 5.1(c).

5.3 Coherent frequency conversion

The experiment is performed in a dilution refrigerator at base temperature $T = 12$ mK, at which point thermal excitations are suppressed and negligible. We investigate coherent emission of the three-level artificial atom under two continuous drives. The measurement circuit is schematically illustrated in Fig. 5.2. All regimes shown in Fig. 5.3(a-c) have been measured with different driving field amplitudes, Ω_{ij}, between states $|i\rangle$ and $|j\rangle$, where i and j are 1, 2 or 3.

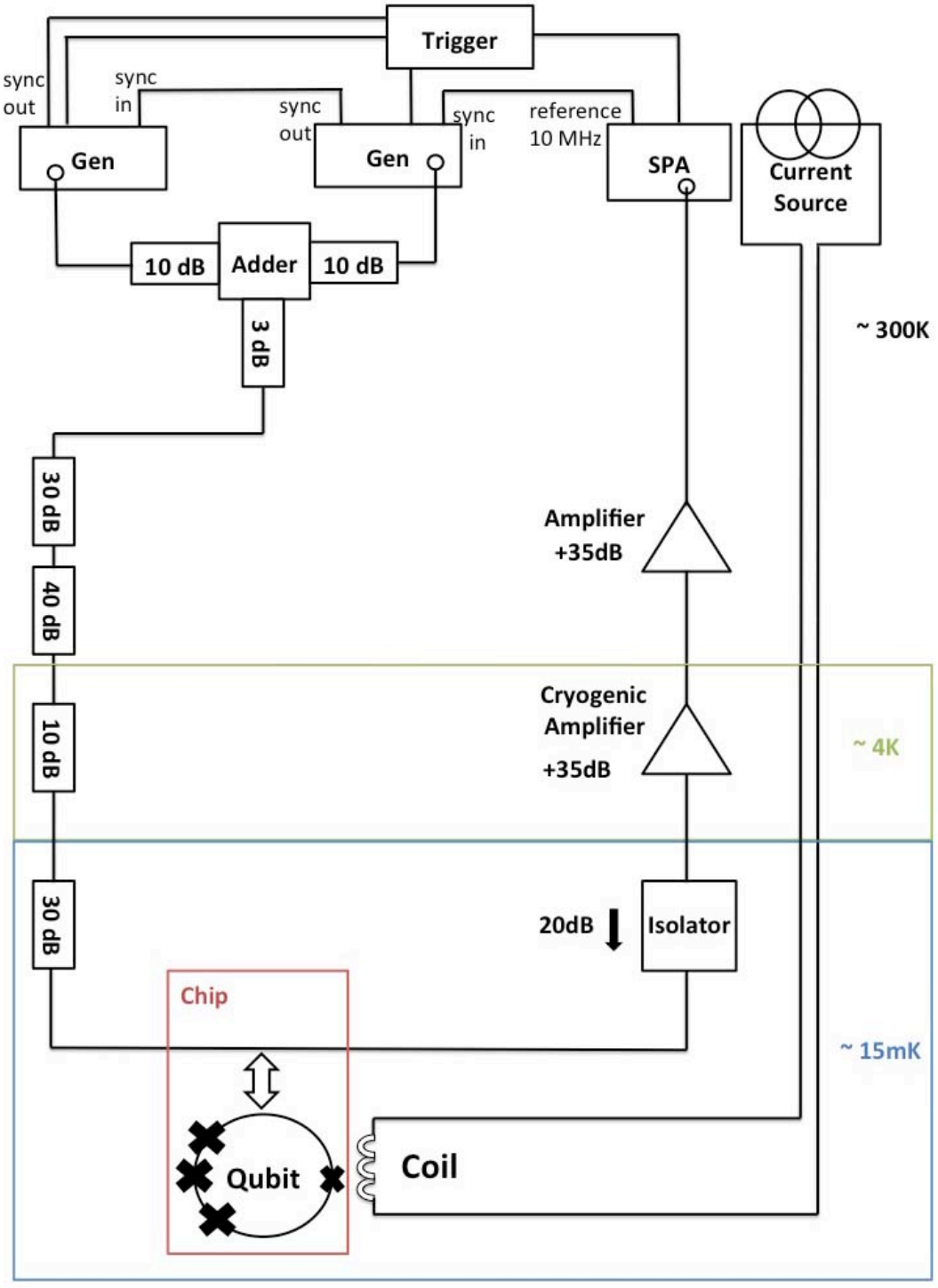

Figure 5.2: Measurement setup for coherent mixing of a three-level artificial atom under two continuous driving tones.

First, let us focus on the case when transitions $|1\rangle \rightarrow |3\rangle$ and $|2\rangle \rightarrow |3\rangle$ are driven with excitation frequencies $\omega_{31}^d = \omega_{31} + \delta\omega_{31}$, $\omega_{32}^d = \omega_{32} + \delta\omega_{32}$

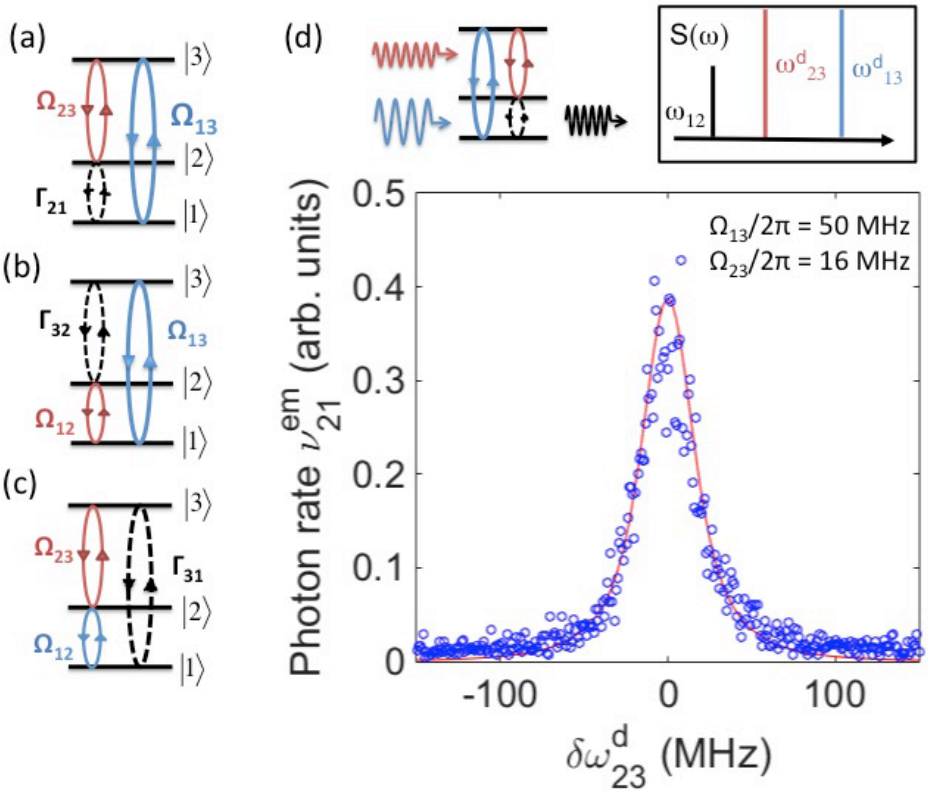

Figure 5.3: Coherent emission in a driven three-level atom with energy diagrams of the pumping schemes. (a) The three-level atom is continuously driven with driving amplitudes Ω_{23} and Ω_{13}, in b) with driving amplitudes Ω_{12} and Ω_{13}, and in c) with driving amplitudes Ω_{12} and Ω_{23}. d) The measured coherent emission peak at ω_{12} in terms of photon rate, ν_{em}^{21}, under driving amplitudes $\Omega_{23}/2\pi = 16$ MHz, $\Omega_{13}/2\pi = 50$ MHz, as a function of detuning of the driving frequency, $\delta\omega_{23}^{d}$. The inset schematically shows the typically measured spectrum.

(Fig. 5.3(a)) and emission at $|2\rangle \rightarrow |1\rangle$ is measured. Here $\delta\omega_{ij}$ are small detunings from their corresponding atomic transition frequencies $\omega_{ij} = \omega_i - \omega_j$ with $i > j$. In the rotating wave approximation, the three-level artificial atom under two drives ω_{31}^{d}, ω_{32}^{d} coupling the atomic states through the dipole interaction $\hbar\Omega_{ij} = \phi_{ij}V_{ij}$, with ϕ_{ij} the atomic dipole moment, is described by the Hamiltonian

$$\begin{aligned} H = & -\hbar(\delta\omega_{31}\sigma_{11} + \delta\omega_{23}\sigma_{22}) \\ & -\hbar\left[\frac{\Omega_{13}}{2}(\sigma_{13} + \sigma_{31}) + \frac{\Omega_{23}}{2}(\sigma_{32} + \sigma_{23})\right], \end{aligned} \tag{5.1}$$

where $\sigma_{ij} = |i\rangle\langle j|$ is the transition operator. The dynamics of the system are

governed by the Markovian master equation.

The atom interacting with 1D open space emits a coherent wave [32, 64]

$$V_{ji}^{em}(x,t) = i\frac{\hbar\Gamma_{ji}}{\phi_{ji}}\left\langle\sigma_{ij}\right\rangle e^{i(k_{ji}|x|-\omega_{ji}t)} \tag{5.2}$$

where $\langle\sigma_{ij}\rangle = \rho_{ji}$ is found from the stationary solution ($\dot{\rho} = 0$) of the master equation. The spectral density $S(\omega) = \frac{1}{2\pi}\int_{-\infty}^{+\infty}\langle\hat{V}_{ij}^{em}(0)\hat{V}_{ji}^{em}(\tau)\rangle_{ss}e^{i\omega\tau}d\tau$, where the subscript (ss) of the correlator denotes the stationary solution, decomposes into incoherent and coherent parts [49]. Using a spectrum analyser we monitor the narrow emission peak, corresponding to the coherent component of the emission $S_{coh} = \hbar\omega Z_0\Gamma_{ji}\langle\sigma_{ij}\rangle_{ss}\langle\sigma_{ji}\rangle_{ss}\delta(\omega-\omega_{ij})$ with the impedance of the transmission line Z_0 and where we have substituted $\Gamma_{ji} = \frac{\omega Z_0}{\hbar\phi_{ji}}$ [32]. The narrow peak power (mathematically a delta function) in the emission spectrum is expected to be

$$P(\omega) = \frac{\hbar\omega\Gamma_{ji}}{2}|\left\langle\sigma_{ij}\right\rangle|^2, \tag{5.3}$$

where $P = \frac{|V_{ji}^{em}|^2}{2Z_0}$. Here ω is in the vicinity of the transition frequency $\omega_{21}/2\pi = 6.48$ GHz as schematically shown above Fig. 5.3(d). The linewidth of the emission peak is as narrow as the linewidths of the generator emission that is driving the artificial atom. If our device is used as a single side band mixer, the maximum power it would sustain is limited by the relaxation time of the transition and must be $\leq \hbar\omega\Gamma_{ij}/8$ since $|\langle\sigma_{ji}\rangle| \leq 1/2$. Due to the operating principle, the bandwidth of such a device is restrained by the transition frequencies of the cyclic atom. Quantum mechanics dictates that there can only be emission at a frequency corresponding to an atomic transition within the atom.

To explain this in an alternative way, it is instrucitve to use the second quantization approach. For the interaction of waves on the single quantum system only one scattering process can occur at the same instant. Introducing creation (annihilation) operator, $a_{ij}^{\dagger}$ (a_{ij}) of a photon at frequency ω_{ij}, the

allowed multi-photon processes, limited by the transitions of the atom, are described by $a_{31}a_{32}^{\dagger}a_{21}^{\dagger}$, and $a_{31}^{\dagger}a_{32}a_{21}$. These two processes conserve energy and explain the creation of the field in Fig. 5.3(a-c) denoted as dashed black lines.

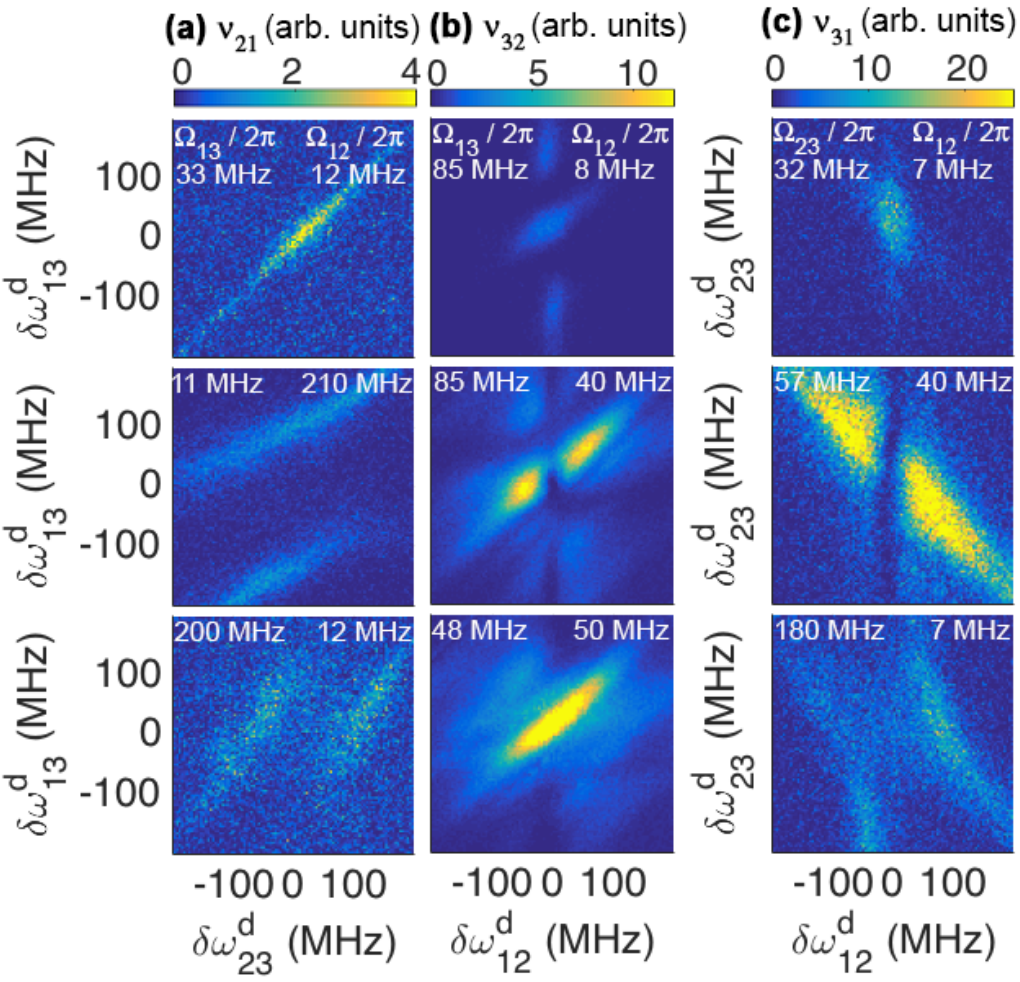

Figure 5.4: Measurement of coherent emission photon rate ν^{em} in arbitrary units as a function of frequency detuning $\delta\omega^d$ of the two drives with amplitudes Ω_{ij} indicated on the panels. (a) Emitted photon rate of the transition from $|2\rangle \rightarrow |1\rangle$, ν_{21}^{em}, with Rabi frequencies corresponding to the respective field strengths Ω_{13}, Ω_{23}. (b) Emitted photon rate of the transition from $|3\rangle \rightarrow |2\rangle$, ν_{em}^{32}, with Rabi frequencies corresponding to the respective field strengths Ω_{13}, Ω_{12}. (c): Emitted photon rate of the transition from $|3\rangle \rightarrow |1\rangle$, ν_{em}^{31}, with Rabi frequencies corresponding to the respective field strengths Ω_{12}, Ω_{23}.

Fig. 5.3(d) shows the measured coherent emission peak as a function of detuning of the driving frequency, $\delta\omega_{23}^d$, expressed as photon rate, $\nu_{21}^{em} = \frac{P(\omega)}{\hbar\omega}$

under weak pumping amplitudes ($\Omega_{13} << \gamma_{13}$, $\Omega_{23} << \gamma_{23}$, where γ_{ij} are dephasing rates). Note that we are measuring only the elastically scattered coherent emission from the atom. Each point in Fig. 5.3(d) corresponds to the narrow emission peak exemplified as series of dotted peaks.

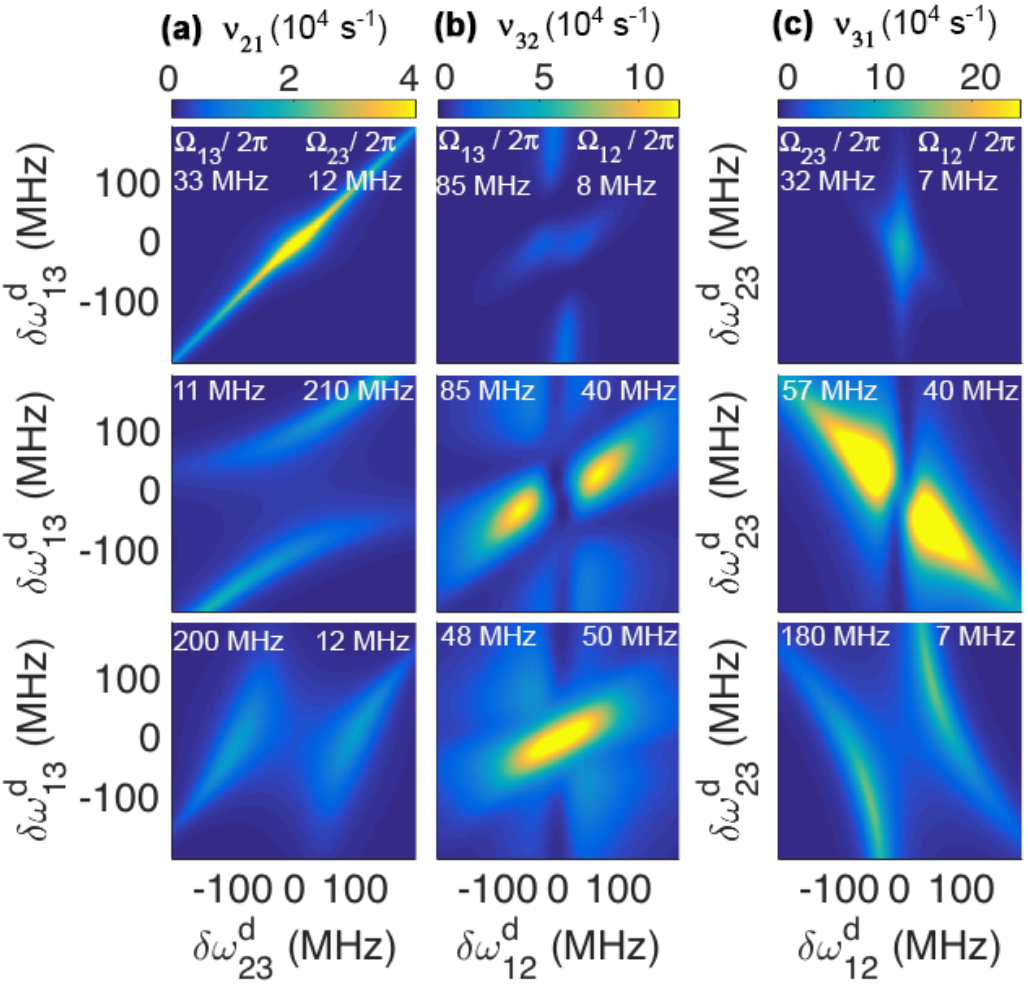

Figure 5.5: Numerical simulations of coherent emission photon rate ν_{em} as a function of frequency detuning $\delta\omega^d$ of the two drives with amplitudes Ω_{ij} indicated on the panels. (a) Emitted photon rate of the transition from $|2\rangle \rightarrow |1\rangle$, ν_{21}^{em}, with Rabi frequencies corresponding to the respective field strengths Ω_{13}, Ω_{23}. (b) Emitted photon rate of the transition from $|3\rangle \rightarrow |2\rangle$, ν_{32}^{em}, with Rabi frequencies corresponding to the respective field strengths Ω_{13}, Ω_{12}. (c) Emitted photon rate of the transition from $|3\rangle \rightarrow |1\rangle$, ν_{31}^{em}, with Rabi frequencies corresponding to the respective field strengths Ω_{12}, Ω_{23}.

We then measure the coherent emission as a function of detuning of $\delta\omega_{23}^d$ for varying values of Ω_{13}, while keeping Ω_{23} constant. Splitting of the coherent

emission under large driving amplitude Ω_{13} is observed which appears due to level splitting induced by driving fields. This splitting is investigated further by recording the coherent emission photon rate versus detuning of the two drives for various combinations of powers. As seen in Fig. 5.4(a), the direction of the splitting is determined by the stronger drive: $\Omega_{13} >> \Omega_{23}$ leads to Ω_{13} splitting level $|1\rangle$; $\Omega_{23} >> \Omega_{13}$ leads to Ω_{23} splitting level $|2\rangle$ and the splitting pattern in the coherent emission V_{21}^{em} is turned by 90 degrees.

In an analogous way, we pump transitions between states $|3\rangle$ and $|1\rangle$ with driving frequency $\omega_{31}^{d} = \omega_{31} + \delta\omega_{31}$ and transitions between states $|2\rangle$ and $|1\rangle$ with driving frequency $\omega_{21}^{d} = \omega_{21} + \delta\omega_{21}$ (Fig. 5.3(b)) resulting in the Hamiltonian

$$\begin{aligned} H = & -\hbar(\delta\omega_{21}\sigma_{22} + \delta\omega_{31}\sigma_{33}) \\ & -\hbar\left[\frac{\Omega_{12}}{2}(\sigma_{12} + \sigma_{21}) + \frac{\Omega_{13}}{2}(\sigma_{32} + \sigma_{23})\right]. \end{aligned} \tag{5.4}$$

In this pumping scheme, the emission power of the coherent emission of transitions between states $|3\rangle$ and $|2\rangle$, V_{32}^{em}, is read out and a narrow peak in the power spectrum at $\omega_{32}/2\pi = 8.35$ GHz is recorded.

The photon rate of coherent emission between states $|3\rangle$ and $|2\rangle$ is monitored as a function of detuning of the drives, $\delta\omega_{13}^{d}$ and $\delta\omega_{12}^{d}$, for several combinations of driving amplitudes, Ω_{13} and Ω_{12}, Fig. 5.4(b), the result being more complex than in the previous driving configuration. It becomes apparent that the coherent emission from the atom depends on all relaxation and dephasing rates. The bright coherent emission line stretching diagonally from the bottom left to the top right corner in Fig. 5.4(b) is primarily determined by dephasing on the $|3\rangle$ to $|2\rangle$ transition, γ_{23}. The vertical coherent emission line that appears for some combinations of powers strongly depends on the dephasing rate γ_{12}. Emission lines broaden when the two driving frequencies are comparable to each other and larger than their dephasing rates.

To achieve coherent frequency upconversion we pump transitions between states $|2\rangle$ and $|1\rangle$ with driving frequency $\omega_{21}^{d} = \omega_{21} + \delta\omega_{21}$ and transitions be-

tween states $|3\rangle$ and $|2\rangle$ with driving frequency $\omega_{32}^d = \omega_{32} + \delta\omega_{32}$, see Fig. 5.3(c). The Hamiltonian for this configuration is

$$\begin{aligned} H = & -\hbar(\delta\omega_{21}\sigma_{11} + \delta\omega_{32}\sigma_{33}) \\ & -\hbar\left[\frac{\Omega_{12}}{2}(\sigma_{12}+\sigma_{21}) + \frac{\Omega_{23}}{2}(\sigma_{32}+\sigma_{23})\right]. \end{aligned} \tag{5.5}$$

As expected, we observe a single narrow coherent emission peak in the emission power spectrum only at the sum frequency $\omega_{12}/2\pi + \omega_{23}/2\pi = 14.83$ GHz, but not at the difference frequency $\omega_{12} - \omega_{23}$, confirming that our results cannot be explained by mixing with a classical nonlinearity. Similar to the previous pumping configurations, the coherent emission peak is split under a strong driving amplitude. Fig. 5.4 (c) shows the behaviour of the coherent emission V_{13}^{em} as a function of detuning of the drives $\delta\omega_{12}/2\pi$ and $\delta\omega_{23}/2\pi$ for a range of driving powers.

Finally, we numerically simulate our experimental results using the master-equation formalism with the Lindblad term

$$\begin{aligned} L[\rho] = & (\Gamma_{31}\rho_{33} + \Gamma_{21}\rho_{22})\sigma_{11} + (\Gamma_{32}\rho_{33} - \Gamma_{21}\rho_{22})\sigma_{22} \\ & -(\Gamma_{31}\rho_{33} + \Gamma_{23}\rho_{22})\sigma_{33} - \sum_{i\neq j}\gamma_{ij}\rho_{ij}\sigma_{ij}. \end{aligned} \tag{5.6}$$

Here $\gamma_{ij} = \gamma_{ji}$ is the damping rate of the off-diagonal terms (dephasing) and Γ_{ij} is the relaxation rate between the levels $|i\rangle$ and $|j\rangle$. In the numerical simulations we chose $\Gamma_{21}/2\pi = 8$ MHz, $\gamma_{21}/2\pi = 8$ MHz, $\Gamma_{32}/2\pi = 38$ MHz, $\gamma_{32}/2\pi = 42$ MHz, $\Gamma_{31}/2\pi = 41$ MHz, and $\gamma_{31}/2\pi = 39.5$ MHz which give the best correspondence between the experiment, Fig. 5.4, and simulations, Fig. 5.5.

5.4 Conclusion

In conclusion, we have demonstrated three-wave mixing and coherent frequency conversion using a single cyclic three-level artificial atom. The fundamental difference from classical Josephson junction based parametric three-

wave mixing devices [123] is that here transition frequencies of the artificial atom are mixed to generate a single coherent emission peak at the sum or difference frequency. A requirement for this phenomena to occur is a cyclic-type atom, which is absent in nature due to electric-dipole selection rules, but can easily be realised with superconducting artificial atoms. Thus we suggest a unique method of generating coherent fields at designed frequency by mixing on the single artificial atom.

Chapter 6

Quantum sensor of absolute power

6.1 Introduction

Superconducting quantum systems are good candidates for developing new quantum devices [81, 87]. They are nanoscale electronic circuits that can be connected to electronic devices and they easily reach the strong coupling regime [32]. Progress in development of superconducting circuits, in particular applications in quantum optics, quantum computing and quantum information, demand calibration of microwave lines and knowledge of applied powers to the circuits situated on a chip at low temperatures. To date, there is no direct method for measuring the absolute power of a microwave signal in a transmission line at cryogenic temperatures since power meters and spectral analysers rely on semiconductor based electronics. Usually, one resorts to room temperature characterisation. However, when the setup including several microwave components (wiring, attenuators, circulators, amplifiers, etc) are cooled down to millikelvin temperatures, their scattering parameters or transfer functions are changed. Furthermore, the circuits on chip are omitted from room temperature characterisations.

There have been several proposals to tackle these challenges. Some of them have limited time resolution due to the finite length of the Π-pulse [80],

are suitable for correcting pulse imperfections [127], or only applicable to specific systems [128]. For example, photon numbers have been accurately calibrated via the Stark shift of a qubit-cavity system [129]. This idea has been extended to multi-level quantum systems (qudits) to deduce the unknown signal frequency and amplitude from the higher level AC Stark shift [130]. Others are based on the shot noise of a known microwave component [131], or on the transmission scattering parameter S21 of a device under test to a reference transmission line [132, 133, 134]. These methods may require separate cool downs or multiple switched cryogenic standards. Another recent proposal uses a transmon qubit coupled to a readout resonator to characterise qubit control lines in the range of 8 to 400 MHz in situ but is limited by the decoherence time of the qubit [135].

In this chapter, we demonstrate that a two-level system strongly coupled to the open space can act as a quantum sensor of absolute power. We realise the quantum sensor using a superconducting flux qubit [136] but in principle it can be implemented with any two-level system that is strongly coupled to the environment. The quantum sensor is independent of dephasing of the two-level system used and in the case of superconducting qubits also of its material.

6.2 Sample description and working principle

We benchmark our absolute power sensor at 7.48 GHz by using four flux qubits with different device parameters. Each flux qubit consists of an Al superconducting loop and four Al/AlOx Josephson junctions, where one of the Josephson junctions, the α-junction, has a reduced geometrical overlap by a factor of α. The coupling capacitance to the 1D transmission line and α-junction was varied; two qubits have been designed to have a coupling capacitance of 3fF with $\alpha = 0.5$, while the remaining two qubits have $C = 5$fF, $\alpha = 0.45$. All four qubits have been co-fabricated on one sample chip using electron-beam lithography and shadow evaporation technique with controllable oxidation (sec. 3.2).

The qubits are revealed through transmission spectroscopy as seen in

Fig. 6.1. Although, by design, two in four qubits should be identical (apart from their position in magnetic field, since their loop area was varied), a clear spread of energies is visible due to technological limitations. We fit the shape of the transition frequency for each qubit to numerical simulations (Fig. 6.2). At 7.48 GHz, we measure power extinction $|t|^2$ and relaxation rate Γ_1, which agree with numerical simulations (Fig. 6.2) of each qubit. Results are tabulated in Table. 6.1.

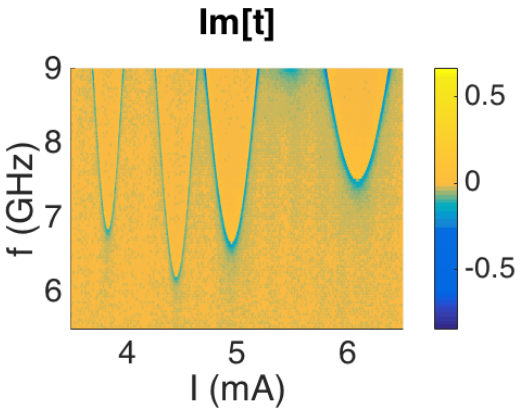

Figure 6.1: Transmission spectroscopy, $Im[t]$, of four flux qubits. We benchmark the absolute power sensor at 7.48 GHz.

Qubit	$\Delta = \hbar\omega_0$	$\lvert t\rvert^2$	$\Gamma_1/2\pi$
A	$6.83\hbar$ GHz	92%	11.5 MHz
B	$6.19\hbar$ GHz	87%	12.36 MHz
C	$6.63\hbar$ GHz	93%	20.8 MHz
D	$7.46\hbar$ GHz	94%	23.27 MHz

Table 6.1: Tunnelling energy Δ, power extinction $|t|^2$ and relaxation rate $\Gamma_1/2\pi$ at $\omega_a = 7.46$ GHz of the four flux qubits used to sense the absolute power at $\omega_a = 7.46$ GHz.

Our quantum sensor relies on the principle that when a two-level system is illuminated by electromagnetic waves with incident photon rate, ν, only a fraction of incident photons is absorbed with rate Ω. The incident electromagnetic wave couples to the two-level system via the dipole interaction energy, $\hbar\Omega = \mu V_0$, where μ is the dipole moment, and V_0 is the Voltage amplitude of the microwave signal we aim to sense. The incident photon rate is $\nu = V_0^2/(2Z\hbar\omega)$, where Z is the impedance of the transmission line that guides the microwave photons to the two-level system with frequency ω. Substituting Voltage amplitude $V_0 = \hbar\Omega/\mu$ and relaxation rate $\Gamma_1 = \mu^2\omega Z/\hbar$ into the

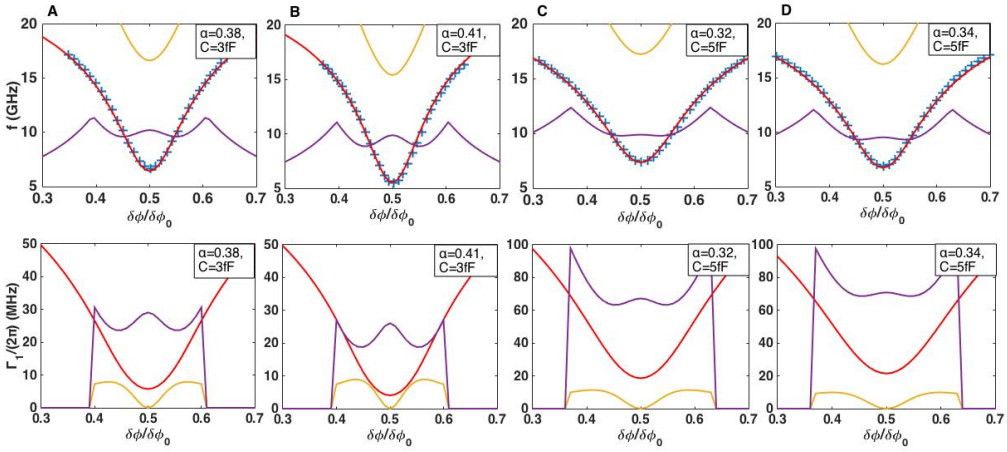

Figure 6.2: Transition frequencies (top row), and relaxation rates (bottom row) $f_{12}, \Gamma_{1(12)}$ in red, $f_{13}, \Gamma_{1(13)}$ in yellow and $f_{23}, \Gamma_{1(23)}$ in violet as a function of flux $\delta\phi/\delta\phi_0$ of artificial atoms A,B,C and D. Blue markers are experimental points taken from transmission spectroscopy (Fig. 6.1). Solid lines are numerical simulations calculated with fitting parameters $E_C = 16$ GHz, $E_J = 53$ GHz with α and coupling capacitance C shown in the insets.

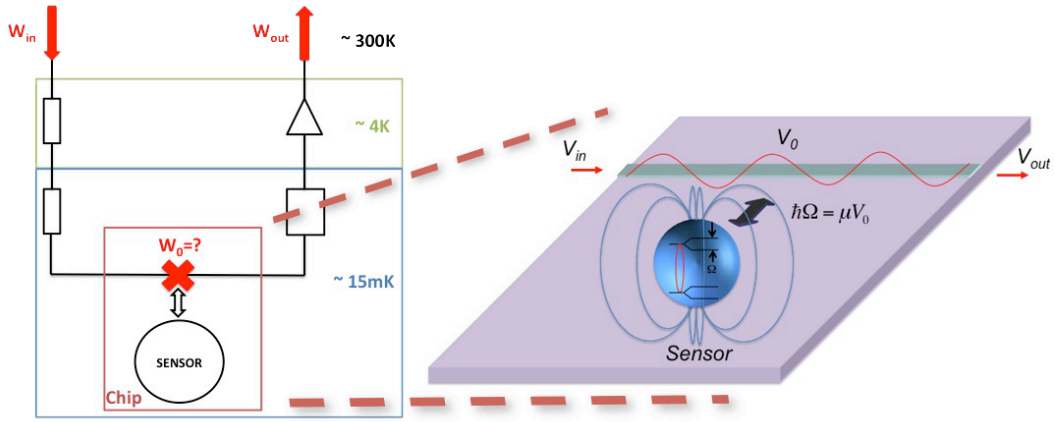

Figure 6.3: Schematic of a cryogenic environment together with an illustration of the chip containing a two-level system - the absolute power sensor - coupled to a transmission line. Knowledge of absolute powers W_0 supplied to a chip at cryogenic temperatures, are important for most quantum technologies with superconducting circuits. The two-level system with dipole moment μ interacts with the field V_0 containing many photons giving rise to coherent oscillations at Rabi frequency Ω.

incident photon rate gives

$$\nu = \frac{\Omega^2}{2\Gamma_1}. \tag{6.1}$$

From Eq. 6.1 it becomes clear that to sense the incident power,

$$W_0 = \nu\hbar\omega, \tag{6.2}$$

or the incident photon rate, ν, the Rabi frequency or absorption rate, Ω, and the relaxation rate, Γ_1, (or the dipole moment μ) should be found.

We study different methods of measuring the required quantities (Ω and Γ_1), in particular by measuring reflection through the transmission line, quantum oscillations, the Mollow triplet and wave mixing [1] on the two-level system.

6.3 Reflection through the transmission line

The two-level atom driven by a resonant microwave is described in the rotating wave approximation by the Hamiltonian $H = \frac{\hbar\omega}{2}\sigma_z - \frac{\hbar\Omega}{2}(\sigma^+ e^{i\phi} + \sigma^- e^{-i\phi})$, where ω is the atomic transition frequency, and $\sigma^\pm = (\sigma_x \pm i\sigma_y)/2$ with the Pauli matrices $\sigma_x, \sigma_y, \sigma_z$. The dynamics of the system are governed by the master equation $\dot{\rho} = -\frac{i}{\hbar}[H, \rho] + \hat{L}[\rho]$ with the Lindblad term $\hat{L}[\rho] = -\Gamma_1\sigma_z\rho_{11} - \Gamma_2(\sigma^+\rho_{10} + \sigma^-\rho_{01})$ where Γ_2 are dephasing rates. When the artificial two-level atom is driven close to its resonance, it acts as a scatterer and generates two coherent waves propagating forward and backward with respect to the driving field [32]

$$V_{sc}(x,t) = i\frac{\hbar\Gamma_1}{\mu}\langle\sigma^-\rangle e^{ik|x|-i\omega t}, \tag{6.3}$$

where $\langle\sigma^-\rangle = \rho_{10}$ is found from the stationary solution of the master equation. The reflection coefficient is defined as $V_{sc} = -rV_0$ and inserting Eq. 6.3 gives

$$r = \frac{\Gamma_1}{2\Gamma_2}\frac{1 + i\delta\omega/\Gamma_2}{1 + (\delta\omega/\Gamma_2)^2 + \Omega^2/\Gamma_1\Gamma_2}. \tag{6.4}$$

We detect the qubit resonances as a sharp dip in the power transmission coefficient. We reach a power extinction $|t|^2 > 85\%$ for all qubits at 7.48 GHz confirming strong coupling to the transmission line. Assuming strong drive ($\Omega >> \Gamma_1\Gamma_2$) the reflection coefficient can be approximated as $r \simeq \Gamma_1^2/(2\Omega^2)$

at $\delta\omega = 0$. The absolute power then becomes

$$\begin{aligned} W_0 &= \frac{\Gamma_1}{4r}\hbar\omega \\ &= \frac{\Omega}{2\sqrt{2r}}\hbar\omega, \end{aligned} \tag{6.5}$$

where the relaxation rate Γ_1, the reflection coefficient r are measurable quantities. By definition the reflection coefficient is linked to the transmission coefficient via $r = 1 - t$. We measure transmission around 7.48 GHz for a range of input powers W_{in} for all qubits. This requires tuning the magnetic field when switching between qubits. The experimental set-up is shown in Fig. 3.10 but with a 50dB attenuator in the input line at room temperature.

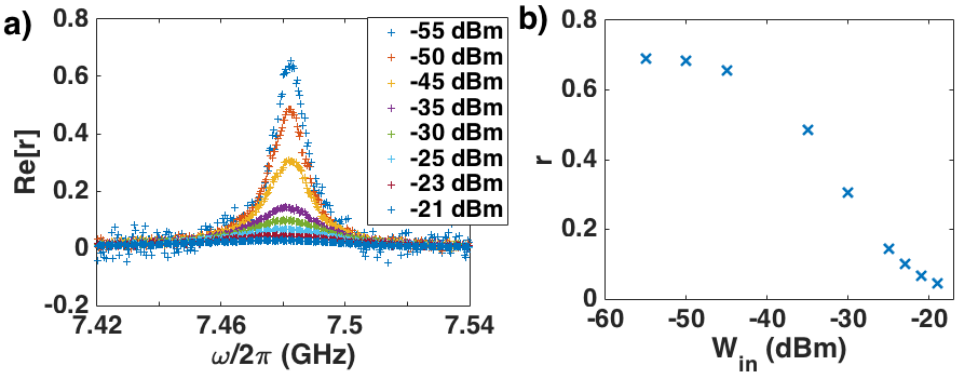

Figure 6.4: Qubit B. a) Reflection as function of frequency for a set of input powers W_{in}. b) Reflection at $f = 7.468$ GHz versus input powers W_{in}.

As seen in Fig. 6.4 the peak in reflection saturates at low powers. We fit Eq. 6.4 in this limit of saturation to obtain relaxation rate Γ_1 (Table 6.1). We calculate the absolute power according to $\Gamma_1\hbar\omega/4r$ (Eq. 6.5) and plot it against W_{in} (W_{out}) with the slope representing the attenuation (gain) in our system (Fig 6.5). We find that we had (-107.0 ± 0.4) dBm attenuation and (54.7 ± 0.4) dBm gain in our measurement circuit where the uncertainties are deduced from the 95% confidence bound from the least square linear fit.

Recall that in the derivation of Eq. 6.5 we approximated r in the limit of strong drive ($\Omega >> \Gamma_1\Gamma_2$). However, at high powers the reflection curve may exhibit distortions due to interference with power leaked.

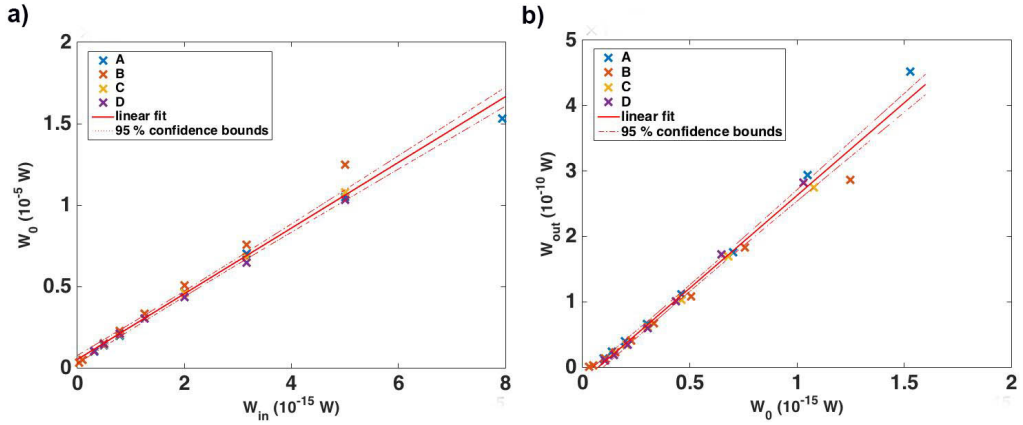

Figure 6.5: The absolute power W_0 sensed by qubits A, B, C, and D (Table 6.1) at 7.48 GHz as a function of (a) input power W_{in} and as a function of (b) output power W_{out}. The slope of the linear fit (solid red line) represents (a) attenuation and (b) gain in our measurement circuit.

6.4 Quantum oscillations

An alternative method comprises of measuring Ω and deducing the absolute power via $W_0 = \Omega^2/(2\Gamma_1)\hbar\omega$. We have already characterised Γ_1 and obtain the Rabi frequency, Ω, for a set of driving powers W_{in} by performing quantum oscillation measurements (Fig.6.6(a)). A schematic of the experimental set-up is shown in Fig. 3.15. At the input, a continuous microwave is chopped by a rectangular pulse of varying pulse length from 1.5 ns to 15.5 ns forming an excitation pulse that is delivered through coaxial cables to the sample (at 12 mK) exciting the atom. The output signal is amplified by a cryogenic and a room temperature amplifier and then chopped by a readout pulse of length 40ns. The emission of the atom is detected using a Vector Network Analyser (VNA). We perform Rabi oscillation measurements for all qubits tuned to 7.48 GHz at values of the microwave power, W_{in}, applied at room temperature ranging from -9 dBm to 8 dBm. Fig. 6.6(b) shows the absolute power W_0 sensed by qubits A, B, C, and D (Table 6.1) at 7.48 GHz as a function of input power W_{in}. The slope of the linear fit (red solid line) gives an attenuation of (-103.9 ± 0.4) dB in our measurement circuit.

A clear disadvantage of this method is that the measurement of Rabi oscillations is limited by dephasing. At high input powers it may not be

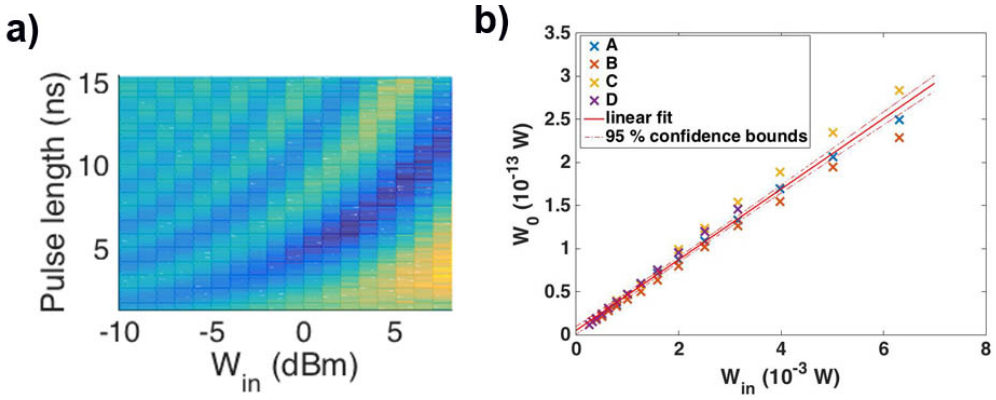

Figure 6.6: (a) Rabi oscillations (of qubit B) for input powers W_{in} ranging from -10 to 8 dBm. (b) The absolute power W_0 sensed by qubits A, B, C, and D (Table 6.1) at 7.48 GHz as a function of input power W_{in}. The slope of the linear fit (solid red line) represents attenuation in our measurement circuit.

possible to measure many periods, and the Rabi frequency has to be deduced through linear interpolation.

6.5 Mollow triplet

A more robust way to deduce the Rabi frequency Ω is to measure the atom's incoherent spectrum under strong drive. The atom coupled to a strong driving field ($\Omega^2 >> \Gamma_1^2$) can be described by the dressed-state picture in which the atomic levels are split by Ω and four transitions between the dressed states are allowed giving rise to the Mollow or resonance fluorescence triplet [51, 53, 32]. To observe the Mollow triplet we measure the power spectrum around 7.48 GHz using a spectrum analyser under a strong resonant drive (Fig.6.7). The expected spectral density is calculated solving Eq. 2.68 giving [32]

$$S(\omega) \approx \frac{1}{2\pi}\frac{\hbar\omega\Gamma_1}{8}\left(\frac{\gamma_s}{(\delta\omega+\Omega)^2+\gamma_s} + \frac{2\gamma_c}{\delta\omega^2+\gamma_c^2} + \frac{\gamma_s}{(\delta\omega-\Omega)^2+\gamma_s^2}\right) \tag{6.6}$$

where half-width of the central and side peaks are $\gamma_c = \Gamma_2$ and $\gamma_s = (\Gamma_1+\Gamma_2)/2$, respectively. We deduce the Rabi frequency from the separation of the Mollow triplet side peaks, find the linear relationship between the Rabi frequency and the input microwave amplitude and calculate the absolute power according to $W_0 = \Omega^2/(2\Gamma_1)\hbar\omega$. The result is shown in Fig. 6.8 yielding an attenuation of

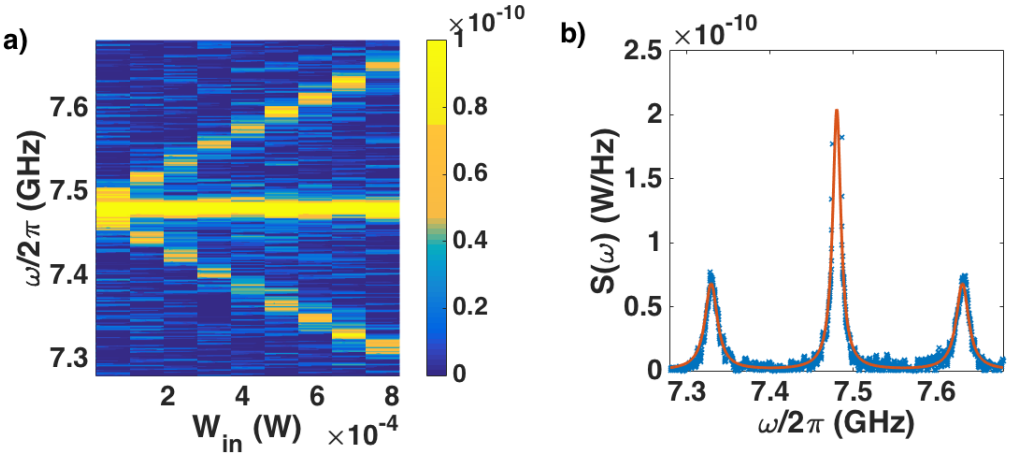

Figure 6.7: Qubit B. a) Mollow triplet as a function of W_{in} and frequency. b) Linear frequency spectral density of emission power under a resonant drive with fixed driving power $W_{in} = 0.73$mW forming the Mollow Triplet. Experimental data is presented by blue markers. The red solid curve presents the fit of the emission spectrum according to Eq.6.6with $\Gamma_1 = 12.36$ MHz and $\Gamma_2 = \Gamma_1/2$. From the fitting parameters we obtain the Rabi frequency as a function of the input driving power.

(-102.6 ± 0.3) dB in our measurement circuit. The gain in our measurement circuit can be deduced from the amplitude of the fit of the Mollow triplet. We obtain a gain of 52.37 dBm.

6.6 Wave mixing in combination with the Mollow triplet

In sec. 4.7.1 we have derived an analytical formula for the amplitude of wave mixing peaks (Eq. 4.24). We drive the artificial atom by two continuous drives with frequencies $\omega_- = \omega_0 - \delta\omega$ and $\omega_+ = \omega_0 + \delta\omega$ where $\omega_0 = 7.48$ GHz and negligible detuning $\delta\omega = 0.5$ kHz $<< \Gamma_1$. For driving amplitudes $\Omega_- >> \Omega_+$ we may approximate the ratio of the first (p=1) and the zeroth (p=0) order peak in the limit of $\Gamma_1\Gamma_2 << \Omega_-^2$ as $V_{-3}/V_{-1} \approx \Gamma_1^2/2\Omega_-^2$.

Then,

$$\frac{W_0}{\Omega_-}\sqrt{\frac{V_3}{V_1}} = \frac{V_0^2}{2Z\Omega_-}\frac{\Gamma_1}{\sqrt{2}\Omega_-} \tag{6.7}$$

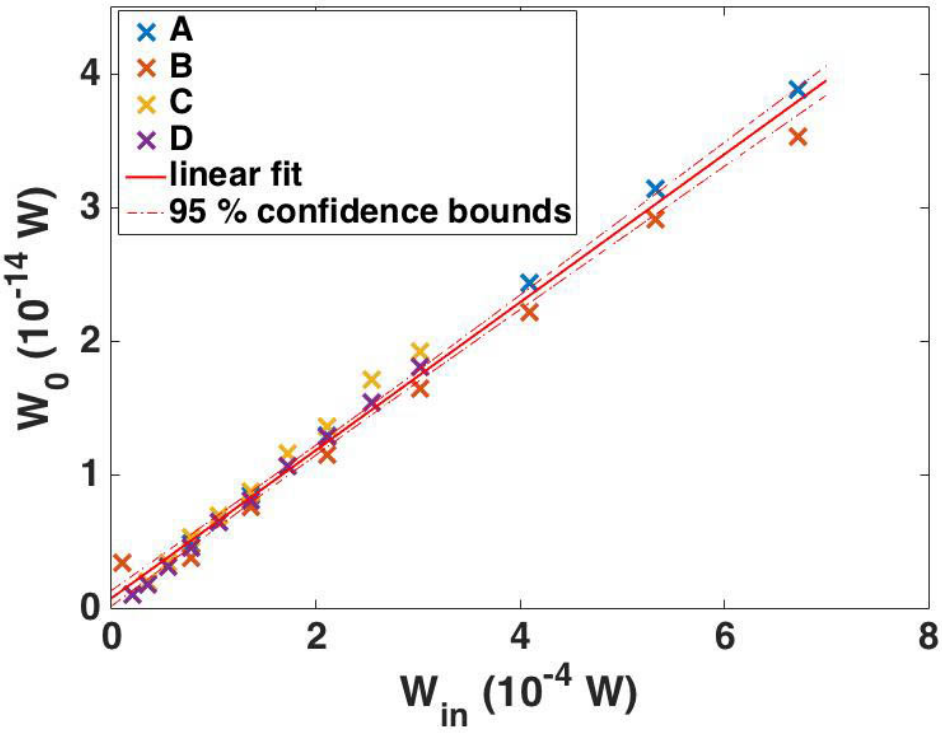

Figure 6.8: The absolute power W_0 sensed by qubits A, B, C, and D (Table 6.1) at 7.48 GHz as a function of input power W_{in}. The slope of the linear fit (solid red line) represents attenuation in our measurement circuit.

and substituting $\Gamma_1 = \omega Z q_p^2/\hbar$ and $q_p V_0 = \hbar\Omega_-$ gives

$$\begin{aligned} \frac{W_0}{\Omega_-}\sqrt{\frac{V_3}{V_1}} &= \frac{V_0^2\omega_- q_p^2}{2\sqrt{2}\Omega_-\hbar} \\ &= \frac{\hbar\omega}{2\sqrt{2}}. \end{aligned} \tag{6.8}$$

Rearranging Eq. 6.8 yields

$$W_0 = \frac{\Omega_-}{2\sqrt{2}}\sqrt{\frac{V_1}{V_3}}\hbar\omega. \tag{6.9}$$

Comparing Eq. 6.9 to Eq. 6.5, we find $r \approx \sqrt{V_3/V_1}$. Already knowing Ω from the previous Mollow triplet measurement, using a spectrum analyser we only need to record amplitudes of the wave mixing peaks V_1, and V_3 (Fig. 6.9(a)) for a set of powers W_{in}. We plot $\sqrt{V_3/V_1}$ as a function of frequency (Fig. 6.9(b)) and find the minimum in the vicinity of 7.486 GHz. The absolute power can

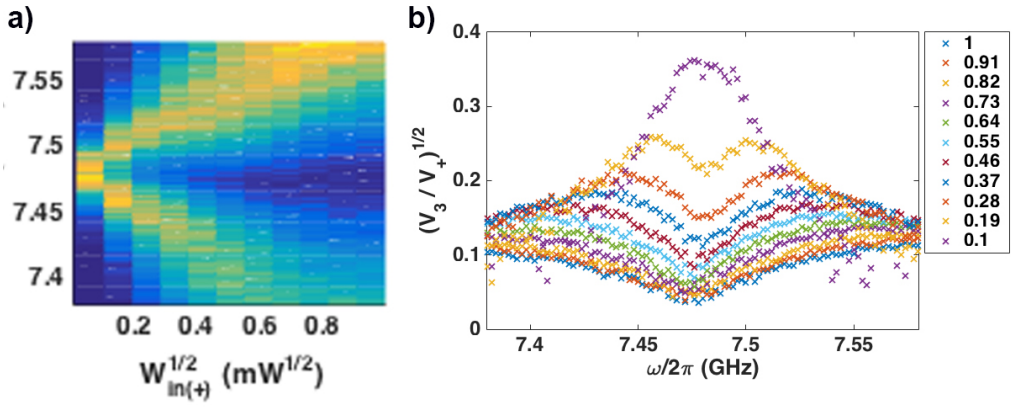

Figure 6.9: Qubit B. a) Spectral component of first side peak (p=1), that appears due to continuous wave mixing with two drives of unequal amplitudes, as a function of frequency for driving amplitudes V_+ ranging from 1 to 0.1 $(mW)^{1/2}$. b) $\sqrt{V_3/V_1}$ as a function of frequency.

now be deduced according to Eq. 6.9. Fig. 6.10 show results for the case of equal driving amplitudes in which we obtain an attenuation of (-109.4 ± 0.9) dB and a gain of (52.0 ± 0.9) dB in our measurement circuit. For unequal

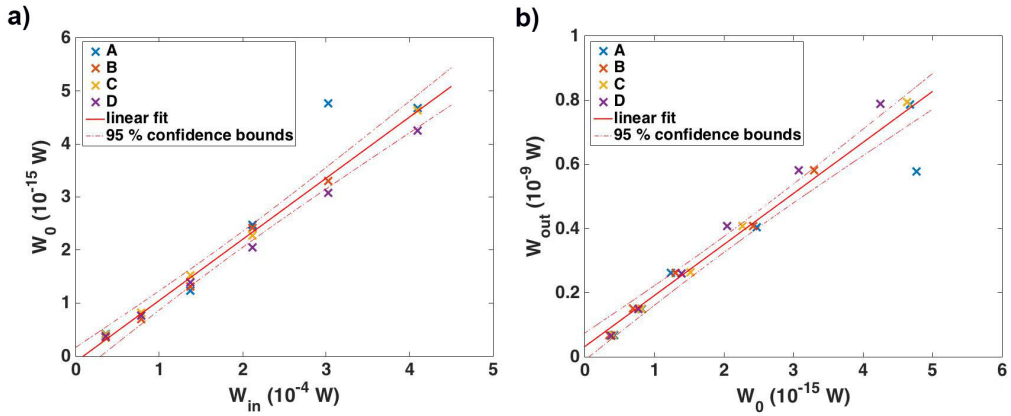

Figure 6.10: Third peak method with equal driving powers: The absolute power W_0 sensed by qubits A, B, C, and D (Table 6.1) at 7.48 GHz as a function of (a) input power W_{in} and as a function of (b) output power W_{out}. The slope of the linear fit (solid red line) represents (a) attenuation and (b) gain in our measurement circuit.

driving amplitudes we find an attenuation of (-111.7 ± 0.6) dBm and a gain of (55.0 ± 0.6) dB in our measurement circuit (Fig. 6.11). The discrepancy in our results may arise from the high sensitivity of the amplitude of the split side peaks (Fig 6.9(a)) to the driving amplitudes. Although we set the two

drives as equal, they may in reality be slightly different.

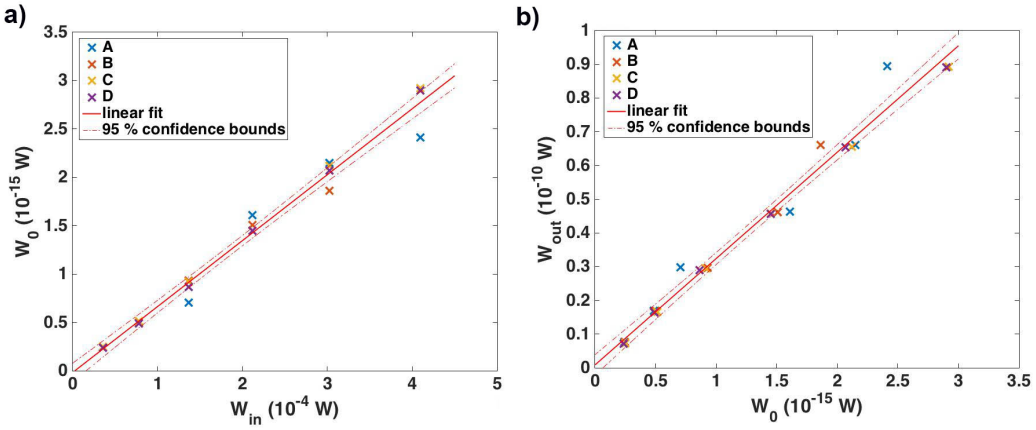

Figure 6.11: Third peak method with unequal driving powers: The absolute power W_0 sensed by qubits A, B, C, and D (Table 6.1) at 7.48 GHz as a function of (a) input power W_{in} and as a function of (b) output power W_{out}. The slope of the linear fit (solid red line) represents (a) attenuation and (b) gain in our measurement circuit.

6.7 Conclusion

To conclude, a two-level system strongly coupled to the environment can act as a sensor of absolute power. Only two quantities, the Rabi frequency Ω and the relaxation rate Γ_1, need to be measured to deduce the absolute power.

We have presented several methods to obtain the two required quantities, which ideally should be measured using the same experimental set-up. If this is not possible, microwave elements outside the cryostat such as wires, choppers and attenuators for example, have to be calibrated using a VNA at room temperature. A summary of the obtained attenuation and gain coefficients is presented in Table 6.2 with the errors coming from the least-square fits. Note that, the different methods required different experimental set-ups. Even though we aimed to keep the attenuation in our system similar, we could not keep it exactly equal across all methods.

Method	Attenuation	Gain
Reflection (sec. 6.3)	(-107.0 ± 0.4) dB	(54.5 ± 0.4) dB
Rabi osc. (sec. 6.4)	(-103.9 ± 0.4) dB	-
Mollow triplet (sec. 6.5)	(-102.6 ± 0.3) dB	52.37 dB
Mixing equal case (sec. 6.6)	(-109.4 ± 0.9) dB	(52.0 ± 0.9) dB
Mixing unequal case (sec. 6.6)	(-111.66 ± 0.6) dB	(55.0 ± 0.6) dB

Table 6.2: Summary of attenuation and gain coefficients obtained by different methods.

We recommend methods 6.5 (Mollow triplet), or 6.6 (Wave mixing) since these are independent of dephasing. So far we have proved the operation principle of the absolute power sensor, however, to quantify systematic errors and the accuracy of our absolute power sensor further work is still due.

Chapter 7

Conclusion and outlook

Quantum optics is the study of light interacting with matter at a fundamental level, where the physical description needs to include quantum mechanics to account for the dynamic of single photons and atoms.

Superconducting qubits or artificial atoms are ideal systems to investigate quantum optical effects. They are nano-scale electrical circuits that are fabricated using techniques that have been well-established in the semi-conductor industry. In contrast to natural atoms, their energy levels can be engineered as desired. Although the first superconducting qubits was demonstrated in 1999 [31], they have not been demonstrated in the UK until we successfully set-up and established the fabrication and measurement of superconducting qubits - artificial atoms - in the Nanotechnology Group at Royal Holloway, University of London in 2015.

This thesis focused on quantum optics experiments with artificial atoms. Strong coupling of artificial atoms has been demonstrated in transmission lines [32], resonators [42], and 3D-cavities [137] allowing to observe scattering on a single atom. Scattering with a single frequency on a single artificial atom has been studied before [32], we have now extended this to two frequencies unveiling, for the first time, different regimes of wave mixing on a single quantum scatterer. We have shown that in quantum wave mixing the superposed and coherent states of light are mapped into a quantised spectrum of narrow peaks with the number of peaks determining the number of interacting

photons. We have partly published our findings in [1], and another article is in preparation (see publication list at the beginning of the thesis).

Furthermore, we demonstrated that we can reach regimes that are unattainable using natural atoms. In particular, cyclic atoms are lacking in nature but can be engineered with superconducting circuits. We have explored three-wave mixing within a single three-level artificial atom allowing coherent frequency conversion to occur. To the best of our knowledge this is the first experiment showing measurements of this effect. This work has been submitted for publication (see publication list).

We also proposed to use a superconducting qubit as a quantum sensor of absolute power at cryogenic temperatures and have performed a proof of principle experiment. We have filed a patent and the article is in preparation (see publication list).

A natural continuation to this thesis would be to develop the absolute power sensor further. Another interesting direction to pursue are quantum simulations of spin dynamics using an array of superconducting qubits. In addition, it was shown theoretically that a quantum state can be perfectly transferred through a one-dimensional chain of spins [138, 139]. Realising this theoretical proposal using a chain of superconducting qubits would make an important contribution towards the development of quantum computers.

Bibliography

[1] A Yu Dmitriev, R Shaikhaidarov, V N Antonov, T Hönigl-Decrinis, and O V Astafiev. Quantum wave mixing and visualisation of coherent and superposed photonic states in a waveguide. *Nature Communications*, 8(1):1352, 2017.

[2] L J Zeng, S Nik, T Greibe, P Krantz, C M Wilson, P Delsing, and E Olsson. Direct observation of the thickness distribution of ultra thin AlO x barriers in Al/AlO x /Al Josephson junctions. *Journal of Physics D: Applied Physics*, 48(39):395308, October 2015.

[3] W Yu-Lin, D Hui, Y Hai-Feng, X Guang-Ming, T Ye, L Jie, C Ying-Fei, Z Shi-Ping, and Z Dong-Ning. Fabrication of Al/AlOx/Al Josephson junctions and superconducting quantum circuits by shadow evaporation and a dynamic oxidation process. *Chinese Physics B*, 22(6):060309, June 2013.

[4] G Dolan and J Dunsmuir. Very small (20 nm) lithographic wires, dots, rings, and tunnel junctions. *Physica B*, (152):7, 1988.

[5] J M Fink. *Quantum Nonlinearities in Strong Coupling Circuit QED: On-Chip Quantum Optics with Microwave Photons and Superconducting Electronic Circuits*. LAP LAMBERT Academic Publishing, August 2001.

[6] Y R Shen. *The principles of nonlinear optics*. New York, Wiley-Interscience, 1984, 575 p., 1984.

[7] R W Boyd. *Nonlinear optics*. Elsevier, 2003.

[8] H Kamerlingh Onnes. The resistance of pure mercury at helium temperatures. *Commun. Phys. Lab. Univ. Leiden, b*, 120, 1911.

[9] M Tinkham. *Introduction to superconductivity*. 2nd ed. Dover Books, 2004.

[10] W Meissner and D Ochsenfeld. Ein neuer Effekt bei Eintritt der Supraleitfaehigkeit. *Naturwiss*, 21(44):787, 1933.

[11] F London Proceedings A149 and 1935. Royal Society of London. *zmhweb.nerc-murchison.ac.uk*.

[12] W S Corak, B B Goodman, C B Satterthwaite, and A Wexler. Atomic heats of normal and superconducting vanadium. *Physical Review*, 102(3):656–661, December 1956.

[13] M A Biondi, M P Garfunkel, and A O McCoubrey. Millimeter wave absorption in superconducting aluminum. *Physical Review*, 101(4):1427–1429, December 1956.

[14] III R E Glover and M Tinkham. Conductivity of Superconducting Films for Photon Energies between 0.3 and 40kT_c. *Physical Review*, 108(2):243–256, October 1957.

[15] J Bardeen, L N Cooper, and J R Schrieffer. Theory of Superconductivity. *Physical Review*, 108(5):1175–1204, December 1957.

[16] L P Gork'ov. *Zh. Eksperim. i Teor. Fiz*, 36:1918, 1959.

[17] V L Ginzburg and L D Landau. *Zh. Eksperim. i Teor. Fiz*, 20:1064, 1950.

[18] B D Josephson. Possible new effects in superconductive tunnelling. *Physics Letters*, 1(7):251–253, July 1962.

[19] B S Deaver and W M Fairbank. Experimental evidence for quantized flux in superconducting cyclinders. *Physical Review Letters*, 7(2):43–46, December 1961.

[20] R P Feynman. Simulating physics with computers. *International Journal of Theoretical Physics*, 21(6-7):467–488, June 1982.

[21] M A Nielsen and I L Chuang. *Quantum computation and quantum information*. University of Queensland, Brisbane, Australia, December 2000.

[22] P W Shor. Introduction to Quantum Algorithms. *eprint arXiv:quant-ph/0005003*, April 2000.

[23] L K Grover. Quantum Mechanics Helps in Searching for a Needle in a Haystack. *Physical Review Letters*, 79(2):325–328, July 1997.

[24] D P DiVincenzo. The physical implementation of quantum computation. *Fortschritte der Physik*, 48(9-11):771–783, December 2000.

[25] J A Jones, M Mosca, and R H Hansen. Implementation of a quantum search algorithm on a quantum computer. *Nature*, 393(6683):344–346, May 1998.

[26] I L Chuang, Lieven M K Vandersypen, X Zhou, Debbie W Leung, and Seth Lloyd. Experimental realization of a quantum algorithm. *Nature*, 393(6681):143–146, May 1998.

[27] J I Cirac and P Zoller. Quantum Computations with Cold Trapped Ions. *Physical Review Letters*, 74(20):4091–4094, May 1995.

[28] C Monroe, D M Meekhof, B E King, W M Itano, and D J Wineland. Demonstration of a Fundamental Quantum Logic Gate. *Physical Review Letters*, 75(25):4714–4717, December 1995.

[29] J M Raimond, M Brune, and S Haroche. Manipulating quantum entanglement with atoms and photons in a cavity. *Reviews of Modern Physics*, 73(3):565–582, August 2001.

[30] H Walther, B T H Varcoe, B-G Englert, and Becker. Cavity quantum electrodynamics. *Rep. Prog. Phys.*, 69(5):1325–1382, May 2006.

[31] Y Nakamura, Yu A Pashkin, and J S Tsai. Coherent control of macroscopic quantum states in a single-Cooper-pair box. *Nature*, 398(6730):786–788, April 1999.

[32] O Astafiev, A M Zagoskin, A A Abdumalikov, Yu A Pashkin, T Yamamoto, K Inomata, Y Nakamura, and J S Tsai. Resonance fluorescence of a single artificial atom. *Science*, 327(5967):840–843, 2010.

[33] J Clarke and F K Wilhelm. Superconducting quantum bits. *Nature*, 453(1031), 2008.

[34] J M Martinis, M H Devoret, and J Clarke. Energy-Level Quantization in the Zero-Voltage State of a Current-Biased Josephson Junction. *Physical Review Letters*, 55(15):1543–1546, October 1985.

[35] Y Makhlin, G Schön, and A Shnirman. Josephson-junction qubits with controlled couplings. *Nature*, 398(6725):305–307, March 1999.

[36] D Vion, A Aassime, A Cottet, P Joyez, H Pothier, C Urbina, D Esteve, and M H Devoret. Manipulating the Quantum State of an Electrical Circuit. *Science*, 296(5569):886–889, May 2002.

[37] V E Manucharyan, J Koch, L I Glazman, and M H Devoret. Fluxonium: Single Cooper-Pair Circuit Free of Charge Offsets. *Science*, 326(5949):113–116, October 2009.

[38] M Büttiker. Zero-current persistent potential drop across small-capacitance josephson junctions. *Phys. Rev. B*, 36:3548–3555, Sep 1987.

[39] Y Nakamura, C D Chen, and J S Tsai. Spectroscopy of Energy-Level Splitting between Two Macroscopic Quantum States of Charge Coherently Superposed by Josephson Coupling. *Physical Review Letters*, 79(12):2328–2331, September 1997.

[40] V Bouchiat, D Vion, P Joyez, D Esteve, and M H Devoret. Quantum coherence with a single cooper pair. In *Physica Scripta T*, pages 165–170. Service de Physique de l'Etat Condense, Gif-sur-Yvette, France, December 1998.

[41] J Koch, T M Yu, J Gambetta, A A Houck, D I Schuster, J Majer, A Blais, M H Devoret, S M Girvin, and R J Schoelkopf. Charge-insensitive qubit design derived from the Cooper pair box. *Physical Review A*, 76(4):042319, October 2007.

[42] A Wallraff, D I Schuster, A Blais, L Frunzio, R S Huang, J Majer, S Kumar, S M Girvin, and R J Schoelkopf. Strong coupling of a single photon to a superconducting qubit using circuit quantum electrodynamics. *Nature*, 431(7005):162–167, September 2004.

[43] S Han, R Rouse, and J E Lukens. Observation of Cascaded Two-Photon-Induced Transitions between Fluxoid States of a SQUID. *Physical Review Letters*, 84(6):1300–1303, February 2000.

[44] J R Friedman, V Patel, W Chen, S K Tolpygo, and J E Lukens. Quantum superposition of distinct macroscopic states. *Nature*, 406(6791):43–46, July 2000.

[45] C H van der Wal, A C J ter Haar, F K Wilhelm, R N Schouten, C J P M Harmans, T P Orlando, S Lloyd, and J E Mooij. Quantum Superposition of Macroscopic Persistent-Current States. *Science*, 290(5492):773–777, October 2000.

[46] C P Slichter. *Principles of Magnetic Resonance*. Springer, Berlin, 1996.

[47] M Lax. Formal Theory of Quantum Fluctuations from a Driven State. *Physical Review*, 129(5):2342–2348, March 1963.

[48] M Lax. Quantum Noise. X. Density-Matrix Treatment of Field and Population-Difference Fluctuations. *Physical Review*, 157(2):213–231, May 1967.

[49] H J Carmichael. *An Open Systems Approach to Quantum Optics*. Springer, 1991.

[50] M O Scully and M S Zubairy. *Quantum optics*. Cambridge University Press, 1999.

[51] B R Mollow. Power Spectrum of Light Scattered by Two-Level Systems. *Physical Review*, 188(5):1969–1975, December 1969.

[52] F Y Wu, R E Grove, and S Ezekiel. Investigation of the spectrum of resonance fluorescence induced by a monochromatic field. *Phys. Rev. Lett.*, 35:1426–1429, Nov 1975.

[53] M Baur, S Filipp, R Bianchetti, J M Fink, M Göppl, L Steffen, P J Leek, A Blais, and A Wallraff. Measurement of autler-townes and mollow transitions in a strongly driven superconducting qubit. *Phys. Rev. Lett.*, 102:243602, Jun 2009.

[54] R J Schoelkopf, A A Clerk, S M Girvin, K W Lehnert, and M H Devoret. Qubits as Spectrometers of Quantum Noise. In *Quantum Noise in Mesoscopic Physics*, pages 175–203. Springer, Dordrecht, 2003.

[55] G Ithier, E Collin, P Joyez, P J Meeson, D Vion, D Esteve, F Chiarello, A Shnirman, Y Makhlin, J. J Schriefl, and G Schön. Decoherence in a superconducting quantum bit circuit. *Phys. Rev. B*, 72:134519, Oct 2005.

[56] Y Makhlin, G Schön, and A Shnirman. *Quantum computing and quantum measurement with mesoscopic Josephson junctions. In: Kulik I.O., Ellialtiolu R. (eds) Quantum Mesoscopic Phenomena and Mesoscopic*

Devices in Microelectronics. NATO Science Series (Series C: Mathematical and Physical Sciences), volume 559.

[57] G Schön Y Makhlin and A Shnirman. Quantum-state engineering with josephson-junction devices. *Rev. Mod. Phys.*, 73:357–400, May 2001.

[58] A A Clerk, M H Devoret, S M Girvin, F Marquardt, and R J Schoelkopf. Introduction to quantum noise, measurement, and amplification. *Rev. Mod. Phys.*, 82:1155–1208, Apr 2010.

[59] O Astafiev, Yu A Pashkin, Y Nakamura, T Yamamoto, and J S Tsai. Quantum noise in the josephson charge qubit. *Phys. Rev. Lett.*, 93:267007, Dec 2004.

[60] F Yoshihara, K Harrabi, A O Niskanen, Y Nakamura, and J S Tsai. Decoherence of flux qubits due to $1/f$ flux noise. *Phys. Rev. Lett.*, 97:167001, Oct 2006.

[61] E L Hahn. Spin echoes. *Phys. Rev.*, 80:580–594, Nov 1950.

[62] H Y Carr and E M Purcell. Effects of diffusion on free precession in nuclear magnetic resonance experiments. *Phys. Rev.*, 94:630–638, May 1954.

[63] C P Slichter. *Principles of Nuclear Magnetic Resonance 3rd edn.* Springer, 1990.

[64] A A Abdumalikov, O V Astafiev, Yu A Pashkin, Y Nakamura, and J S Tsai. Dynamics of coherent and incoherent emission from an artificial atom in a 1d space. *Phys. Rev. Lett.*, 107:043604, Jul 2011.

[65] V Ambegaokar and A Baratoff. Tunneling Between Superconductors. *Physical Review Letters*, 10(11):486–489, June 1963.

[66] R Igreja and C J Dias. Analytical evaluation of the interdigital electrodes capacitance for a multi-layered structure. *Sensors and Actuators A: Physical*, 112(2-3):291–301, May 2004.

[67] M A Mohammad, M Muhammad, S K Dew, and M Stepanova. Fundamentals of electron beam exposure and development. In *Nanofabrication*. Springer, Wien, 2012.

[68] L I Aparshina, S V Dubonos, S V Maksimov, A A Svintsov, and S I Zaitsev. Energy dependence of proximity parameters investigated by fitting before measurement tests. *Journal of Vacuum Science and Technology B: Microelectronics and Nanometer Structures*, 15(6):2298–2302, November 1997.

[69] S V Dubonos, B N Gaifullin, H F Raith, A A Svintsov, and S I Zaitsev. Evaluation, verification and error determination of proximity parameters α, β and ν in electron beam lithography. *Microelectronic Engineering*, 21(1-4):293–296, January 1993.

[70] R Dylewicz, N Klauke, J Cooper, and F R M Matt. Conductive polymers for advanced micro-and nanofabrication processes. *sigmaaldrich.com*, 2011.

[71] M Nahum and J M Martinis. Ultrasensitive-hot-electron microbolometer. *Applied Physics Letters*, 63(22):3075–3077, December 1993.

[72] L P H Jeurgens, W G Sloof, F D Tichelaar, and E J Mittemeijer. Growth kinetics and mechanisms of aluminum-oxide films formed by thermal oxidation of aluminum. *Journal of Applied Physics*, 92(3):1649–1656, July 2002.

[73] P H Smith. Transmission line calculator. *Electronics*, 1939.

[74] J Q You and F Nori. Atomic physics and quantum optics using superconducting circuits. *Nature*, 474(7353):589–597, June 2011.

[75] D I Schuster, A A Houck, J A Schreier, A Wallraff, J M Gambetta, A Blais, L Frunzio, J Majer, B Johnson, M H Devoret, S M Girvin, and

R J Schoelkopf. Resolving photon number states in a superconducting circuit. *Nature*, 445(7127):515–518, February 2007.

[76] Z H Peng, S E De Graaf, J S Tsai, and O V Astafiev. Tuneable on-demand single-photon source in the microwave range. *Nature Communications*, 7:12588, August 2016.

[77] A A Houck, D I Schuster, J M Gambetta, J A Schreier, B R Johnson, J M Chow, L Frunzio, J Majer, M H Devoret, S M Girvin, and R J Schoelkopf. Generating single microwave photons in a circuit. *Nature*, 449(7160):328–331, September 2007.

[78] C Lang, C Eichler, L Steffen, J M Fink, M J Woolley, A Blais, and A Wallraff. Correlations, indistinguishability and entanglement in Hong-Ou-Mandel experiments at microwave frequencies. *Nature Physics*, 9(6):345–348, June 2013.

[79] M Hofheinz, E M Weig, M Ansmann, R C Bialczak, E Lucero, M Neeley, A D O'Connell, H Wang, John M Martinis, and A N Cleland. Generation of Fock states in a superconducting quantum circuit. *Nature*, 454(7202):310–314, July 2008.

[80] M Hofheinz, H Wang, M Ansmann, and R C Bialczak. Synthesizing arbitrary quantum states in a superconducting resonator. *Nature*, 459(546):546–549, May 2009.

[81] O Astafiev, K Inomata, A O Niskanen, T Yamamoto, Yu A Pashkin, Y Nakamura, and J S Tsai. Single artificial-atom lasing. *Nature*, 449(7162):588–590, October 2007.

[82] I-C Hoi, A F Kockum, T Palomaki, T M Stace, B Fan, L Tornberg, S R Sathyamoorthy, G Johansson, P Delsing, and C M Wilson. Giant Cross–Kerr Effect for Propagating Microwaves Induced by an Artificial Atom. *Physical Review Letters*, 111(5):053601, August 2013.

[83] G Kirchmair, B Vlastakis, Z Leghtas, S E Nigg, H Paik, E Ginossar, M Mirrahimi, L Frunzio, S M Girvin, and R J Schoelkopf. Observation of quantum state collapse and revival due to the single-photon Kerr effect. *Nature*, 495(7440):205–209, March 2013.

[84] D Roy, C M Wilson, and O Firstenberg. Strongly interacting photons in one-dimensional continuum. *Reviews of Modern Physics*, 89(2):021001, May 2017.

[85] I-C Hoi, C M Wilson, G Johansson, J Lindkvist, B Peropadre, T Palomaki, and P Delsing. Microwave quantum optics with an artificial atom in one-dimensional open space. *New J. Phys.*, 15(2):025011, 2013.

[86] D M Toyli, A W Eddins, S Boutin, S Puri, D Hover, V Bolkhovsky, W D Oliver, A Blais, and I Siddiqi. Resonance Fluorescence from an Artificial Atom in Squeezed Vacuum. *Physical Review X*, 6(3):031004, July 2016.

[87] O V Astafiev, Jr A A Abdumalikov, A M Zagoskin, Yu A Pashkin, Y Nakamura, and J S Tsai. Ultimate On-Chip Quantum Amplifier. *Physical Review Letters*, 104(18):183603, May 2010.

[88] I-C Hoi, C M Wilson, G Johansson, T Palomaki, B Peropadre, and P Delsing. Demonstration of a Single-Photon Router in the Microwave Regime. *Physical Review Letters*, 107(7):073601, August 2011.

[89] Y-L L Fang and H U Baranger. Multiple emitters in a waveguide: Nonreciprocity and correlated photons at perfect elastic transmission. *Physical Review A*, 96(1):013842, July 2017.

[90] A F van Loo, A Fedorov, K Lalumière, B C Sanders, A Blais, and A Wallraff. Photon-mediated interactions between distant artificial atoms. *Science*, 342(6165):1494–1496, 2013.

[91] J A Mlynek, A A Abdumalikov, C Eichler, and A Wallraff. Observation of Dicke superradiance for two artificial atoms in a cavity with high decay rate. *Nature Communications*, 5:5186, November 2014.

[92] W D Oliver, Y Yu, J C Lee, K K Berggren, L S Levitov, and T P Orlando. Mach-Zehnder Interferometry in a Strongly Driven Superconducting Qubit. *Science*, 310(5754):1653–1657, December 2005.

[93] M Sillanpää, T Lehtinen, A Paila, Y Makhlin, and P Hakonen. Continuous-time monitoring of Landau-Zener interference in a cooper-pair box. *Physical Review Letters*, 96(18):467, May 2006.

[94] P Neilinger, S N Shevchenko, J Bogár, M Rehák, G Oelsner, D S Karpov, U Hübner, O Astafiev, M Grajcar, and E Il'ichev. Landau-Zener-Stückelberg-Majorana lasing in circuit quantum electrodynamics. *Physical Review B*, 94(9):88, September 2016.

[95] F Schackert, A Roy, M Hatridge, M H Devoret, and A D Stone. Three-Wave Mixing with Three Incoming Waves: Signal-Idler Coherent Attenuation and Gain Enhancement in a Parametric Amplifier. *Physical Review Letters*, 111(7):073903, August 2013.

[96] M Orszag. *Quantum optics: Including noise reduction, trapped ions, quantum trajectories, and decoherence, third edition.* Springer International Publishing, Cham, January 2016.

[97] A Maser, B Gmeiner, T Utikal, S Götzinger, and V Sandoghdar. Few-photon coherent nonlinear optics with a single molecule. *Nature Photonics*, 10(7):450–453, July 2016.

[98] A I Lvovsky and M G Raymer. Continuous-variable optical quantum-state tomography. *Reviews of Modern Physics*, 81(1):299–332, March 2009.

[99] A P T Lau, D J F Barros, E Ip, and J M Kahn. Coherent detection in optical fiber systems. *Optics Express*, 16(2):753–791, January 2008.

[100] J-T Shen and S Fan. Coherent Single Photon Transport in a One-Dimensional Waveguide Coupled with Superconducting Quantum Bits. *Physical Review Letters*, 95(21):213001, November 2005.

[101] R Miller, T E Northup, K M Birnbaum, A Boca, A D Boozer, and H J Kimble. Trapped atoms in cavity qed: coupling quantized light and matter. *J. Phys. B*, 38(9):S551, 2005.

[102] R Hanson, L P Kouwenhoven, J R Petta, S Tarucha, and L M K Vandersypen. Spins in few-electron quantum dots. *Rev. Mod. Phys.*, 79:1217–1265, Oct 2007.

[103] M V G Dutt, L Childress, L Jiang, E Togan, J Maze, F Jelezko, A S Zibrov, P R Hemmer, and M D Lukin. Quantum register based on individual electronic and nuclear spin qubits in diamond. *Science*, 316(5829):1312–1316, 2007.

[104] H De Riedmatten, M Afzelius, M U Staudt, C Simon, and N Gisin. A solid-state light—[ndash]—matter interface at the single-photon level. *Nature*, 456(7223):773–777, December 2008.

[105] I-C Hoi, C M Wilson, G Johansson, T Palomaki, B Peropadre, and P Delsing. Demonstration of a single-photon router in the microwave regime. *Phys. Rev. Lett.*, 107:073601, Aug 2011.

[106] W R Kelly, Z Dutton, J Schlafer, B Mookerji, T A Ohki, J S Kline, and D P Pappas. Direct observation of coherent population trapping in a superconducting artificial atom. *Phys. Rev. Lett.*, 104:163601, Apr 2010.

[107] K V R M Murali, Z Dutton, W D Oliver, D S Crankshaw, and T P Orlando. Probing decoherence with electromagnetically induced

transparency in superconductive quantum circuits. *Phys. Rev. Lett.*, 93:087003, Aug 2004.

[108] A A Abdumalikov, O Astafiev, A M Zagoskin, Yu A Pashkin, Y Nakamura, and J S Tsai. Electromagnetically induced transparency on a single artificial atom. *Phys. Rev. Lett.*, 104:193601, May 2010.

[109] S H Autler and C H Townes. Stark effect in rapidly varying fields. *Phys. Rev.*, 100:703–722, Oct 1955.

[110] M A Sillanpää, J Li, K Cicak, F Altomare, J I Park, R W Simmonds, G S Paraoanu, and P J Hakonen. Autler-townes effect in a superconducting three-level system. *Phys. Rev. Lett.*, 103:193601, Nov 2009.

[111] S Novikov, J E Robinson, Z K Keane, B Suri, F C Wellstood, and B S Palmer. Autler-townes splitting in a three-dimensional transmon superconducting qubit. *Phys. Rev. B*, 88:060503, Aug 2013.

[112] S U Cho, H S Moon, Y-T Chough, M-H Bae, and N Kim. Quantum coherence and population transfer in a driven cascade three-level artificial atom. *Phys. Rev. A*, 89:053814, May 2014.

[113] K Inomata, K Koshino, Z R Lin, W D Oliver, J S Tsai, Y Nakamura, and T Yamamoto. Microwave down-conversion with an impedance-matched Λ system in driven circuit qed. *Phys. Rev. Lett.*, 113:063604, Aug 2014.

[114] É Dumur, B Küng, A K Feofanov, T Weissl, N Roch, C Naud, W Guichard, and O Buisson. V-shaped superconducting artificial atom based on two inductively coupled transmons. *Phys. Rev. B*, 92:020515, Jul 2015.

[115] T Y Li, J F Huang, and C K Law. Scattering of two distinguishable photons by a Ξ-type three-level atom in a one-dimensional waveguide. *Phys. Rev. A*, 91:043834, Apr 2015.

[116] R Bianchetti, S Filipp, M Baur, J M Fink, C Lang, L Steffen, M Boissonneault, A Blais, and A Wallraff. Control and tomography of a three level superconducting artificial atom. *Phys. Rev. Lett.*, 105:223601, Nov 2010.

[117] S R Sathyamoorthy, L Tornberg, A F Kockum, B Q Baragiola, J Combes, C M Wilson, T M Stace, and G Johansson. Quantum nondemolition detection of a propagating microwave photon. *Phys. Rev. Lett.*, 112:093601, Mar 2014.

[118] J Q You, Y-x Liu, and F Nori. Simultaneous cooling of an artificial atom and its neighboring quantum system. *Phys. Rev. Lett.*, 100:047001, Jan 2008.

[119] S O Valenzuela, W D Oliver, D M Berns, K K Berggren, L S Levitov, and T P Orlando. Microwave-induced cooling of a superconducting qubit. *Science*, 314(5805):1589–1592, 2006.

[120] S Gasparinetti, M Pechal, J-C Besse, M Mondal, C Eichler, and A Wallraff. Correlations and entanglement of microwave photons emitted in a cascade decay. *Phys. Rev. Lett.*, 119:140504, Oct 2017.

[121] Y-x Liu, H-C Sun, Z H Peng, A Miranowicz, J S Tsai, and F Nori. Controllable microwave three-wave mixing via a single three-level superconducting quantum circuit. *Sci. Rep.*, 4(1), December 2014.

[122] D Patterson and J M Doyle. Sensitive chiral analysis via microwave three-wave mixing. *Phys. Rev. Lett.*, 111:023008, Jul 2013.

[123] N Roch, E Flurin, F Nguyen, P Morfin, P Campagne-Ibarcq, M H Devoret, and B Huard. Widely tunable, nondegenerate three-wave mixing microwave device operating near the quantum limit. *Phys. Rev. Lett.*, 108:147701, Apr 2012.

[124] Y-J Zhao, J-H Ding, Z H Peng, and Y-x Liu. Realization of microwave amplification, attenuation, and frequency conversion using a single three-level superconducting quantum circuit. *Phys. Rev. A*, 95:043806, Apr 2017.

[125] F Lecocq, I M Pop, I Matei, E Dumur, A K Feofanov, C Naud, W Guichard, and O Buisson. Coherent frequency conversion in a superconducting artificial atom with two internal degrees of freedom. *Phys. Rev. Lett.*, 108:107001, Mar 2012.

[126] J E Mooij, T P Orlando, L Levitov, L Tian, C H van der Wal, and S Lloyd. Josephson persistent-current qubit. *Science*, 285(5430):1036–1039, 1999.

[127] S Gustavsson, O Zwier, J Bylander, F Yan, F Yoshihara, Y Nakamura, T P Orlando, and W D Oliver. Improving quantum gate fidelities by using a qubit to measure microwave pulse distortions. *Phys. Rev. Lett.*, 110:040502, Jan 2013.

[128] J Bylander, M S Rudner, A V Shytov, S O Valenzuela, D M Berns, K K Berggren, L S Levitov, and W D Oliver. Pulse imaging and nonadiabatic control of solid-state artificial atoms. *Phys. Rev. B*, 80:220506, Dec 2009.

[129] D I Schuster, A Wallraff, A Blais, L Frunzio, R-S Huang, J Majer, S M Girvin, and R J Schoelkopf. ac stark shift and dephasing of a superconducting qubit strongly coupled to a cavity field. *Phys. Rev. Lett.*, 94:123602, Mar 2005.

[130] A Schneider, J Braumüller, L Guo, P Stehle, H Rotzinger, M Marthaler, A V Ustinov, and M Weides. Local Sensing with the Multi-Level AC Stark Effect. *aeprint arXiv:quant-ph/1801.05144v2*, January 2018.

[131] N Bergeal, F Schackert, L Frunzio, D E Prober, and M H Devoret. Mesoscopic resistor as a self-calibrating quantum noise source. *App. Phys. Lett.*, 100(20):203507, May 2012.

[132] J-H Yeh and S M Anlage. In situ broadband cryogenic calibration for two-port superconducting microwave resonators. *Rev. Sci. Instrum.*, 84(3):034706, March 2013.

[133] L Ranzani, L Spietz, and J Aumentado. Broadband calibrated scattering parameters characterization of a superconducting quantum interference device amplifier. *App. Phys. Lett.*, 103(2):022601, July 2013.

[134] L Ranzani, L Spietz, Z Popovic, and J Aumentado. Two-port microwave calibration at millikelvin temperatures. *Rev. of Sci. Instrum.*, 84(3):034704, March 2013.

[135] M Jerger, Z Vasseli, and A Fedorov. In situ characterization of qubit control lines: a qubit as a vector network analyzer. *ArXiv e-prints:quant-ph/1706.05829*, June 2017.

[136] J E Mooij, T P Orlando, L Levitov, L Tian, C H van der Wal, and S Lloyd. Josephson persistent-current qubit. *Science*, 285(5430):1036–1039, 1999.

[137] M Reagor, W Pfaff, C Axline, R W Heeres, N Ofek, K Sliwa, E Holland, C Wang, J Blumoff, K Chou, M J Hatridge, L Frunzio, M H Devoret, L Jiang, and R J Schoelkopf. Quantum memory with millisecond coherence in circuit qed. *Phys. Rev. B*, 94:014506, Jul 2016.

[138] Bose, S. Quantum communication through an unmodulated spin chain. *Physical Review Letters*, 91(20), November 2003.

[139] M Christandl, N Datta, A Ekert, and A J Landahl. Perfect State Transfer in Quantum Spin Networks. *Physical Review Letters*, 92(18):187902, May 2004.